Development and investigation of devices for ultrahigh speed gastrointestinal Optical Coherence Tomography imaging

by

Kaicheng Liang

S.M. Electrical Engineering and Computer Science
Massachusetts Institute of Technology, 2014

B.S. Biomedical Engineering
Duke University, 2010

Submitted to the Department of Electrical Engineering and Computer Science
in Partial Fulfillment of the Requirements for the Degree of

Doctor of Philosophy

at the

MASSACHUSETTS INSTITUTE OF TECHNOLOGY

June 2018

Signature of Author Signature redacted
Department of Electrical Engineering and Computer Science
May 23, 2018

Certified by Signature redacted
Professor James G. Fujimoto
Elihu Thomson Professor of Electrical Engineering and Computer Science
Thesis Supervisor

Accepted by Signature redacted
Professor Leslie A. Kolodziejski
Professor of Electrical Engineering and Computer Science
Chair, Department Committee on Graduate Students

Development and investigation of devices for ultrahigh speed gastrointestinal Optical Coherence Tomography imaging

by

Kaicheng Liang

Submitted to the Department of Electrical Engineering and Computer Science in Partial
Fulfillment of the Requirements for the Degree of Doctor of Philosophy

ABSTRACT

Diseases of the gastrointestinal (GI) tract are typically diagnosed by random biopsy of tissue, which samples only a small area and often misses focal neoplasias. Existing endoscopic visualization tools including white light endoscopy, narrowband imaging and confocal laser endomicroscopy have enabled *in vivo* assessment to guide biopsies, but suffer from technical limitations and have demonstrated suboptimal sensitivity and specificity to neoplasia. Optical Coherence Tomography (OCT) can generate *in vivo*, 3-dimensional microscopic imaging. Recent efforts in ultrahigh-speed OCT systems for endoscopic applications have shown promise, but devices had limited fields of view and imprecise beam scanning mechanisms, limiting image quality and coverage.

This thesis develops a wide range of new fiber optic devices that substantially extend OCT capabilities in the GI tract, either by greatly increasing field of view for wide field mapping of entire luminal organs, or achieving high precision 2-D beam scanning with compact actuators for *in vivo* microscopy. Piezoelectrically actuated fiber scanning devices enable forward viewing for focal inspection, while micromotor actuators combined with pneumatic or piezoelectric mechanisms enclosed in tethered capsules generate side viewing over large areas. The work also advances the emerging paradigm of gastrointestinal screening without use of sedation, which promises to lower costs of screening and improve access for a broader population. Design, fabrication and benchtop evaluation of devices, as well as pre-clinical and clinical imaging protocols are reported. Results from validation studies in living swine, and human patients in collaboration with the Veterans Affairs Boston Healthcare System are discussed. The thesis work demonstrates new imaging modalities for *in vivo* detection and diagnosis of GI pathology that could have important applications in disease screening, surveillance, and therapeutic procedures.

Thesis Supervisor: Professor James G. Fujimoto

Title: Elihu Thomson Professor of Electrical Engineering and Computer Science

Acknowledgments

I am forever grateful to my advisor Jim Fujimoto for his mentorship. First, he gave me the gift of being an MIT student, which I will treasure, and will always make me look smarter than I actually am. Second, he taught me how to be a rigorous and meticulous scientist, although I will still forget my scalebars from time to time. Third, he showed me how to lead, by example, without compromise, and in service to community and society. I will strive for the same (but maybe do a few things differently). And finally, he proved that scientists through their work can improve the lives of millions, and so we should dedicate our lives to trying. As I enter the next phase of my career and pursue scientific leadership, these lessons will always be on my mind. If I can be a little nicer than Jim Fujimoto while achieving a little less success than he has, then I will be content. However it is much more likely that I will end up a lot less nice and still a lot less successful.

My sincere thanks to the VA Boston Healthcare System for hosting my research. I dream to find a hospital back home with medical professionals and patients who will support cutting edge research with the same commitment, energy, and enthusiasm. Dr. Hiroshi Mashimo, fearless endoscopist, will always be my role model in his mastery of his chosen art, passion for education and mentorship, and commitment to interdisciplinary collaboration (read: saint-like toleration of bungling engineers in his clinic). The professionals of the Endoscopy unit have been gracious, patient, and incredibly supportive of our work. Having worked with veterans will always be one of the greatest privileges of my life. For each and every one of you who gulped down a tethered capsule without batting an eyelid, thank you.

Special thanks to our collaborator Vijay Jayaraman, founder of Praevium Research. Your brilliant, one-of-a-kind VCSEL has enabled my entire PhD.

How do I express my gratitude to my colleagues at MIT, who have taught me everything I know, endured my painfully ignorant questions, and inspired me to strive for excellence in all things? Hsiang-Chieh Lee PhD and Tsung-Han Tsai PhD were my first mentors, teaching me to assemble probes, polish GRIN lenses, build FC/APC connectors and countless other tasks, and continuing to dazzle me in their new careers as budding thought leaders. Chao Zhou PhD was a kind supervisor, and his suggestion of "why don't you learn how to build a probe?" set me on a path that defined my PhD. Zhao Wang PhD was an incredible collaborator – the year over which we unraveled the mysteries of the cycloid scanner was the purest agony and joy that I will probably ever experience (perhaps until I have a child). Osman Ahsen PhD worked with me longer than anybody else, and even though we often disagreed about almost everything, I was always in awe of his intelligence and commitment to his beliefs. Benjamin Potsaid PhD was the ultimate resource in OCT engineering, but more inspirational was his supreme composure in the face of adversity, whether it was seeing that I had snapped down a VCSEL yet again, or when he methodically helped me debug a system issue the night before a critical swine experiment, or when we prepared a complex grant proposal submission. Lucas Cahill and Jason Zhang were wonderful office mates. The ophthalmology team has been the perfect foil to endoscopy, and I have enjoyed our vigorous discussions while admiring your long list of publications. Special thanks to Dr. Giovanni Traverso, who helped us bring the swine model back to our lab for the first time in a very long time.

I'm grateful to A*STAR for their generous funding, which was a helpful incentive for my lab to hire me. I'm even more grateful to my parents, who have had to live half the world away from their only child for nearly a third of my life, while supporting me unconditionally from afar. My partner Michelle has stuck with me for exactly all of that time, inspired me with her own academic adventure, and continues to be a pillar of encouragement and comfort. Thank you.

Contents

Chapter 1

Introduction: Clinical motivation and state of the art

Imaging of luminal organs *in vivo* can have enormous impact on clinical decision making, including diagnosis, treatment planning, and real-time therapeutic guidance. In gastroenterology and the gastrointestinal (GI) tract, where advanced endoscopes have been used for decades, clinicians are no strangers to cutting edge technology for imaging and therapy. This chapter will briefly review some important clinical needs for real-time *in vivo* imaging, as well as a number of existing commercially available technologies that have attempted to meet these needs, with a focus on applications in the upper GI tract including the esophagus and proximal gastric cardia.

Barrett's Esophagus (BE) and dysplasia

Barrett's Esophagus (BE) is a premalignant condition that is associated with, and believed to be a consequence of, chronic (>5 years) gastroesophageal reflux disease (GERD). Acid exposure in the distal esophagus over a prolonged period can lead to metaplastic changes in the squamous epithelium, producing a columnar phenotype. BE can be observed during standard esophagogastroduodenoscopy (EGD) as having a salmon pink appearance of the mucosa, and is confirmed histologically by specialized intestinal metaplasia (IM) with presence of goblet cells, although presence of goblet cells is not required by Britain and Japan for BE diagnosis and is being debated[1]. The standard definition of BE progression is from non-dysplastic BE to low-grade/high-grade dysplasia (LGD/HGD) to esophageal adenocarcinoma (EAC), however the pathogenesis of BE and dysplasia still lacks consensus [2]. BE is thus an important precursor to

EAC, which in recent decades has become the cancer with the fastest growing incidence in the Western world, although the actual incidence in the United States is still relatively low at less than 5 cases per 100,000 people[3]. Specific demographics including male gender, Caucasian race, and obesity are important risk factors for BE and EAC. Although chronic GERD is one of the most important risk factors to indicate endoscopic screening for BE, it has been noted that over 40% of EAC patients never report GERD symptoms[4]. After BE is diagnosed, patients are enrolled in regular endoscopic surveillance, during which biopsies are obtained every 2 cm of BE length in 4 quadrants, known as random biopsy or the "Seattle protocol". After a surveillance endoscopy is negative for dysplasia, risk of neoplastic progression is deemed reduced, and patients are recalled after a year and then every 3-5 years for follow up endoscopies and biopsies.

Pathogenesis and natural history of BE

The pathogenesis of BE remains unclear, and there are multiple controversies regarding the onset and progression of the disease. BE is observed manifesting as different lengths in different patients, therefore it was previously believed that BE may be occurring at the GEJ and then progressing longer over time due to increased acid exposure from a weakened lower esophageal sphincter[5]. However, multiple recent studies found that BE lengths remained relatively stable over a follow up of several years[6], suggesting that a short/long BE phenotype may be occurring relatively rapidly, and then subsequently changing little.

In general, BE develops from 'multi-potential' stem cells, which can develop into a mixture of gastric and intestinal cells. As a result, a BE segment can contain a range of mucosal phenotypes, where gastric and intestinal epithelium coexist as a mosaic, although the former decreases in prevalence when moving from distal to proximal esophagus. As the BE evolves proximally, glands multiply by gland fission, resulting in 'patches' or clusters.

There are disagreements[7] on whether BE originates from squamous epithelium of the normal esophagus, or from the proximal gastric cardia. In the first and more traditional theory, esophageal glands and ducts of the squamous epithelium contain stem cells that are stimulated by acid reflux and encouraged to differentiate abnormally into intestinal metaplasia. Esophageal glands have been observed to contain dysplasia, adenoma, or even carcinoma *in situ*, further boosting this theory. In the competing theory, the columnar cells of the proximal cardia migrate up into the acid-damaged distal esophagus. This was initially dismissed because gastric-type mucosa does not contain goblet cells, unlike intestinal mucosa including intestinal metaplasia. However, it has been consistently found that regions of BE can contain a range of tissue types including gastric-type epithelium, suggesting that intestinal metaplasia is a two-step process – migration of gastric epithelium into the distal esophagus, which then undergoes intestinalization. This further implies that columnar-lined mucosa without goblet cells may simply be a precursor lesion to BE, and is thus of no less malignant potential.

Supporting this theory is the histological observation that there exists a region of 'junctional' tissue between the stomach and the esophagus that has been termed 'cardiac mucosa'[8], which appears to exist in all adult individuals but becomes longer in patients with BE. The cardiac mucosa consists of both cardiac glands and oxyntocardiac glands, the former with metaplastic potential. In patients with prior esophagectomy[9], cardiac mucosa (columnar metaplasia) is said to develop at the neo-GEJ within the first 1-2 years, with BE only manifesting years after. These observations appear to support the theory that BE arises from the stomach.

Ablative therapy and challenges

Fortunately, there are now a multitude of endoscopic techniques for the treatment of dysplasia and early carcinoma in the esophagus that do not require surgery. Radiofrequency ablation (RFA) is now largely the standard of care, due to notable success in a large clinical trial that showed complete eradication of dysplasia in 91% of LGD patients and 81% of HGD patients[10]. Other modalities including endoscopic mucosal resection[11] and cryogenic ablation[12] are also available, which are often combined with RFA to further improve outcomes. In these treatment protocols, ablation is used to completely eradicate an entire segment of BE, which at completion is termed complete eradication/remission of intestinal metaplasia (CEIM/CRIM). However, in esophagectomy studies where large segments of esophagus were histologically analyzed[13], dysplasia was found to be highly focal, such that random biopsy would likely miss these regions. Without a confirmatory biopsy to diagnose dysplasia, therapies however effective would not be administered in a timely fashion. Therefore, there is great interest in imaging modalities that can be used during endoscopy to evaluate the esophageal mucosa for abnormalities, possibly detecting dysplasia in real time without excisional biopsy and the consequent delay for histopathology. Such a rapid protocol for dysplasia detection might motivate immediate treatment for dysplasia during the same endoscopy procedure, reducing delays to treatment and risk of loss to follow up.

While RFA has found widespread success in the eradication of dysplasia, recent large scale studies of durability at academic centers have raised serious concerns of recurrent IM and dysplasia after completion of a treatment course. In one large study of a single center where the RFA technique was first developed[14], 24% of patients developed recurrence of BE or dysplasia, at an incidence rate of 9.6% per year. The mean time to recurrence was 1.88 years after CEIM. In a larger multi-center study[15], the incidence rate of recurrence was 33% at 2 years after CEIM, and 22% of all recurrences contained dysplasia. It was observed that up to half of recurrences were found at the gastroesophageal junction (GEJ) and ~1 cm distal to the top of the gastric folds, however standard endoscopic visualization has been poor at identifying accurately the GEJ especially after ablation[16]. Therefore, there is an unmet need to rigorously evaluate the GEJ after RFA treatment for recurrent disease and dysplasia. The high rate of recurrence also suggests that patients will need continued endoscopic surveillance for an indefinite period, further motivating the enhancement of diagnostic yield/efficacy of endoscopic visualization.

Narrow band imaging (NBI) for enhanced wide field assessment

Since over a decade ago, there has been substantial effort by multiple research and clinical groups to improve the superficial visibility of mucosal structure and vasculature in the GI tract. A technique known as chromoendoscopy, in which the superficial mucosa is stained with a dye and then assessed with an endoscope, was found to be highly diagnostic in multiple studies[17-19], but has fallen out of favor due to perceived procedural complications and time expense. A Japanese group proposed a type of 'electronic chromoendoscopy', whereby the use of blue (415 nm) illumination and a combination of detection filters (415 nm, 445 nm, 500 nm) could enhance the visualization of the mucosal surface[20]. This became known as 'narrow band imaging' (NBI). After initial pilot studies by clinicians in Japan, the technique began to catch on internationally after a number of high profile studies by leading groups in the US[21] and Europe[22]. NBI was found to enhance the visibility and contrast of the superficial mucosa, which contained both a mucosal and vascular pattern. NBI was marketed by Olympus as an enhanced imaging technology that was integrated into conventional endoscope systems and could be switched on/off whenever needed. Early seminal papers by Japanese groups using magnification and chromoendoscopy obtained and categorized a range of mucosal/vascular patterns observed in both upper[23] and lower[24] GI pathology, part of which became known as the Kudo pit pattern system. It became clear that NBI could visualize similar mucosal structure without the procedural difficulty of chromoendoscopy. A multitude of pattern classification systems were later developed using NBI over time[25, 26], however it became well established that NBI was extremely high performing. Early studies demonstrated up to 100% sensitivity and 99% specificity in detecting HGD in BE[21], and while later multi-center studies reported more conservative results, sensitivity/specificity performance for dysplasia detection hovered in the range of 80-90% when assessed by experts[26].

While NBI in the upper GI tract continues to be a leading diagnostic technique, it has notably failed to perform adequately when assessing the GEJ after RFA treatment for recurrence of BE, despite high quality visualization of the mucosal patterns. In a study of 21 patients by a leading European group, the sensitivity/specificity for identifying recurrent intestinal metaplasia were 65% and 46% respectively[27]. Another study of 198 patients found that any endoscopic finding using white light endoscopy (WLE) or NBI had only 59% sensitivity and 81% specificity to recurrence[16]. It has been suggested that high resolution imaging for the detection of goblet cells would confirm the presence of specialized intestinal metaplasia, however ongoing controversies over histological criteria for BE also apply. Therefore, mucosal patterns and any modalities that enhance exclusively *en face* microstructure may not be sufficiently diagnostic for this specific yet extremely important application.

Confocal laser endomicroscopy (CLE) for high resolution inspection

WLE or enhanced endoscopy with NBI has yet to achieve optimal sensitivity/specificity to dysplasia, even in expert hands. Upon locating a region of interest using a wide field modality such as WLE/NBI, it may be desirable to examine the region with high resolution. There have been successful efforts in miniaturizing confocal microscopy into compact endoscopic devices, which is known as confocal endomicroscopy[28]. Using intravenous or topical fluorescent agents, and a blue laser for excitation, cellular imaging could be achieved. For example, when using intravenous fluorescein or topical acriflavine, an excitation wavelength of 488 nm may be used. About a decade ago, Pentax commercialized an endoscope system with an integrated confocal microscope at the distal end, in collaboration with Optiscan. Tissue could be imaged in contact with a viewing window adjacent to the endoscope optics. The distal microscope contained an electromagnetic mechanism for actuating an optical fiber in 2 axes, and a third mechanism for depth (axial) focus scanning, which led to substantial bulk but generated high quality images. This became known as endoscopic confocal laser endomicroscopy (eCLE), and quickly led to a number of compelling studies[29] such as the detection of BE-associated neoplasia with sensitivity/specificity of 93%/98% in 63 patients[30]. A competing technology also became commercially available, developed by Mauna Kea Technologies (in reference to the telescope observatories on the Hawaiian summit) and branded as Cellvizio. The device was a small diameter catheter probe that could be passed through the 2.8 mm diameter accessory channel of a standard endoscope. Images were acquired via a 2-dimensional fiber bundle, thus no bulky scanning mechanisms were necessary. This device became known as probe-based confocal laser endomicroscope (pCLE).

	Pentax/Optiscan (eCLE)	Mauna Kea Cellvizio (pCLE)
Field of view	475 μm	240-600 μm
Transverse resolution	0.7 μm	1-5 μm
Axial (depth) resolution	7 μm	20-30 μm
Imaging depth	250 μm	60-130 μm
Frame rate	0.8-1.6 frames/sec	12 frames/sec
Device diameter	13 mm	2.5-2.7 mm

Table 1. Summary of specifications for commercial endomicroscopy. Adapted from [28, 29].

pCLE images were objectively lower quality than eCLE (poorer resolution and depth penetration, see Table 1) however a number of ergonomic advantages proved to be the winning recipe, including the small diameter catheter size (allowing use in any existing endoscope systems) and the rapid frame rate (minimizing motion artifacts) of pCLE. Eventually Pentax discontinued their confocal endomicroscopy product, while the Mauna Kea Cellvizio continued to be used in a number of clinical studies, although reports have complained of difficulty in obtaining stable motion-free images with adequate cellular visibility, suggesting need for substantial operator skill/experience[31]. The approximately half millimeter, highly limited field of view exacerbates problems with stabilizing images, particularly at the GEJ where there is substantial patient motion, and also precludes the ability to efficiently inspect a large BE segment, such that a widefield modality is typically required in combination. In a large multicenter trial of 101 patients[32], the sensitivity/specificity of pCLE in combination with WLE/NBI for detection of BE neoplasia was 76%/84%. Notably, use of pCLE alone had poor performance (63% sensitivity, 93% specificity). A group at Rice University has worked on developing a low cost but functionally equivalent analog to the Mauna Kea system, using proflavine as a topical stain and 450 nm for the excitation laser. A number of clinical studies have been performed with this technology[33], some notably in low resource communities[34], to great success and highly promising diagnostic performance.

Volumetric laser endomicroscopy (VLE)

Optical coherence tomography (OCT) in the GI tract has been studied extensively for nearly two decades; in the year 2000 some of the first GI OCT images were reported from virtually the entire GI tract, including the esophagus, stomach, colon, duodenum and terminal ileum[35]. Early imaging speeds were infeasible for *in vivo* imaging, but the swept source speed revolution promised a wide range of realistic applications for OCT in gastroenterology[36, 37]. A group at Massachusetts General Hospital (MGH) developed an OCT balloon for a much larger field of view coverage than previous small-diameter catheter probes[38, 39]. This device was later commercialized by NinePoint Medical with their OCT product Volumetric Laser Endomicroscopy (VLE)[40]. VLE generates a volumetric scan over 6 cm length of the esophagus and the entire circumference, with balloon diameters 14/17/20 cm. Over a 90 second pullback scan, 1200 cross-sectional frames are acquired. The system imaging speed is 50 kHz axial scan rate, and the rotational frame rate is 12.2 Hz[41]. The transverse and axial resolution is 40 um (FWHM) and 7 um (tissue).

Early studies with VLE focused on understanding tissue features using precise *ex vivo* histological correlation[42, 43], namely visibility of layered structure, signal intensity of surface layer versus subsurface, and the presence of atypical glands/ducts. These studies were largely inspired by OCT studies nearly a decade ago that first proposed these features[44, 45]. Leggett et al.[42] showed 86% sensitivity and 88% specificity for BE dysplasia in 50 EMR specimens (34 HGD, 16 LGD + NDBE) from 27 patients, although important limitations of the study include images acquired *ex vivo* and one of the image readers was also responsible for developing the diagnostic criteria. Swager et al.[43] found worse performance of 83% sensitivity and 71% specificity, and used only selected cross-sectional images as well as a variable scoring system for each VLE feature arbitrarily adjusted to optimize diagnostic performance. Clinical studies by a number of leading groups investigating interobserver agreement[46] and learning curve have also been recently published.

In vivo studies of diagnostic performance will require precise histological correlation to imaging features in order to validate diagnosis. The MGH group had previously pioneered the use of a laser to produce marks on tissue guided by imaging[47, 48]. While the concept laser marking generates an impression of precision, the production of a visible mark with continuous-wave lasers can take from one to several seconds, which is likely to be compromised by physiological motion. The latest VLE systems carry this marking capability, and clinical trials of feasibility and accuracy of laser marking to guide biopsies indicated by VLE features are ongoing.

Scope of the thesis

The primary aims of this thesis are the development of innovative, minimally invasive imaging devices with applications in studying diseases of the gastrointestinal tract, pre-clinical and clinical validation of these new technologies, and comprehensive analysis of novel imaging data to assess potential clinical utility in future diagnostic and pathogenesis studies. While these studies focus on the use of OCT to deliver ultrahigh speed 3-dimensional (3-D) optical imaging, these devices are optical scanners that can be generalized for any flying spot optical imaging or microscopy modality.

Chapter 2 is a continuation of the author's Master thesis work in developing ultrahigh speed forward imaging probes based on piezoelectric actuation of a resonant scanning fiber, and describes clinical translation and validation in patients. The technology was further miniaturized and packaged for *in vivo* endoscopic OCT imaging, where the probe was introduced in the accessory channel of a colonoscope. OCT angiography could be obtained by reducing the scan field to achieve oversampling. Imaging was performed in patients undergoing colonoscopy. Imaging of a range of GI mucosa was performed, including a hyperplastic polyp, for which an altered crypt pattern was observed in *en face* views.

Chapter 3 describes a tethered capsule device for imaging at speeds of 10-20x faster than previously reported OCT capsules. Capsules can cover large areas of luminal organs but require high imaging speeds and precision optical scanning for high quality 3-D and *en face* imaging. In this work, a tethered capsule with two independent scan mechanisms – a micromotor and a pneumatic scanner was developed, imaging at 1 MHz axial scan rate for rapidly acquired *en face* views. Validation results in living swine esophagus and rectum are presented.

Chapter 4 describes the successful clinical translation of high speed, *en face* imaging capsule technology to patients with BE. Wide field luminal imaging has the potential to detect focal areas of dysplasia. A simplified scanning capsule containing only a micromotor for precise circumferential scanning was used to image up to 24 cm length of the esophagus, in sedated patients during endoscopy. 18 patients were imaged to investigate optimal design and imaging parameters. Novel *en face* OCT features of dysplasia including dilated glands and irregular mucosal patterns were reported, in combination with traditional cross-sectional OCT features.

Chapter 5 describes a substantial improvement in tethered capsule precision scanning by the introduction of resonant fiber scanning. The combination of resonant scanning and micromotor scanning dramatically improved scan precision and speed from the earlier pneumatic design (Chapter 3). The device generated a novel scan trajectory known as a cycloid. Using the micromotor as the slow axis scanner, the cycloid scan could rapidly acquire 2-D *en face* images (or 3-D volumes) with no flyback or reset downtime. The micromotor could be slowed down to achieve oversampling for OCT angiography. This rapid 2-D scan mechanism has applications not only in OCT but any benchtop flying spot microscopy modality. Imaging was performed in the living human rectum at 3 volumes/sec over a 1 mm x 38 mm strip field of view.

Chapter 6 reports a clinical case series of 16 patients imaged with a micromotor tethered capsule without use of sedation. Volumetric and *en face* imaging of the esophagus and BE segment was performed over large fields of view of 4 x ~10 cm in 10 seconds. Image quality metrics including tissue contact and longitudinal uniformity were assessed in relation to BE segment length and presence of sliding hiatal hernia. Image features including atypical gland clusters and irregular mucosal patterns were investigated to discover associations with patient history (pathology and treatment history).

Chapter 7 concludes the thesis.

Chapter 2

Forward viewing endomicroscopy with piezoelectrically actuated fiber scanning

Introduction

Endoscopic optical coherence tomography (OCT) using minimally invasive catheters is an emerging imaging modality in gastroenterology[42, 49]. Early studies demonstrated side viewing catheters that scanned the OCT beam by proximal rotary and pullback actuation of a torque cable[50]. This design enabled imaging of luminal organs and continues to be the workhorse of commercially available catheter OCT systems[42]. Proximal actuation via a long catheter with multiple bends produces non-uniform rotational and/or longitudinal distortion[41, 51]. Recent catheters have used distal rotary scanning micromotors, reducing rotational distortion[52-54]. Our group developed new methods for side viewing OCT that use distal actuation for 2-dimensional scanning[55]. Distal scanning enables OCT angiography (OCTA), which uses repeated scans to detect motion contrast from blood flow to visualize microvasculature and has been used extensively in ophthalmology[56]. Our group recently demonstrated endoscopic OCTA using distal micromotor scanning[52, 57].

Forward viewing OCT catheters are of clinical interest because they generate images analogous to endoscopic views[24], and can examine small regions of interest (ROIs) at high resolution. Forward viewing devices using microelectromechanical system (MEMS) [58] or piezoelectric actuators[59, 60] enable distal 2-D scanning, and are thus immune to catheter bending. These devices exploit mechanical resonances for scanning and are uniquely suited for high speed OCT due to their high scan speed[61, 62].

This chapter reports a forward viewing OCT piezoelectric probe and endoscopic imaging in the human gastrointestinal (GI) tract *in vivo*. The probe has a 3.3 mm diameter and 20 mm rigid length, and can be used into the endoscopic accessory channel, enabling use in existing endoscopic workflows. Volumetric OCT and OCTA was performed at 1 MHz axial scan (A-scan) rate to image colonic mucosa and a hyperplastic polyp in human patients. The high speed laser was a critically enabling factor in clinical translation of OCT/OCTA, particularly in endoscopy where patient motion is significant and rapid volumetric display with adequate image sampling is essential. The ability to perform high A-scan speed endoscopic forward viewing OCT has clinical potential for providing volumetric and *en face* microscopic tissue assessment.

Materials and Methods

This work was performed in collaboration with the VA Boston Healthcare System (Dr. Hiroshi Mashimo MD PhD and staff at the Endoscopy Unit), Thorlabs (Dr. Benjamin Potsaid) and Praevium Research (Dr. Vijaysekhar Jayaraman) for use of prototype swept source technology. Our early investigations into piezoelectric scanning were supported by Prof. Xingde Li's group at Johns Hopkins University who provided us with designs for high voltage amplification circuits and imaging probes for testing purposes.

The OCT system[52] (Fig. 1A) used a dual circulator interferometer with a MEMS vertical cavity surface emitting laser (VCSEL) swept source at 1310 nm (Thorlabs/Praevium)[63] running at ~500 kHz sweep rate, producing a ~1 MHz bidirectional A-scan rate. The exact VCSEL repetition rate was set to a high integer multiple of the probe resonant frequency, and the waveform generator used to drive the VCSEL was also used to clock the D/A board (National Instruments), simplifying electronic synchronization. The OCT interferometer and detector sensitivity was 103 dB at an incident power of 35 mW on the sample. The probe one-way transmission was 80%; therefore, the effective system sensitivity was ~100 dB. Losses were due to imperfect circulators/couplers (AC Photonics), use of fiber mating sleeves instead of splices, and imperfect optical surfaces of the probe lens and fiber cleave (Oxford angle cleaver). The imaging range was 2.1 mm in air and the axial resolution was 9 μm in tissue. The A/D board (AlazarTech 9370) was optically clocked up to 1.1 GHz by a Mach-Zehnder interferometer. Optical clocking with linear in k sampling enabled direct Fourier transformation, simplifying post-processing. A D/A board (National Instruments PCIe-6323) generated amplitude-modulated sinusoidal waveforms to drive a piezoelectric actuator, which were synchronized to the start of each volumetric acquisition. The phase shifted sinusoidal waveforms produced a spiral (Fig. 3B) fiber scanning trajectory.

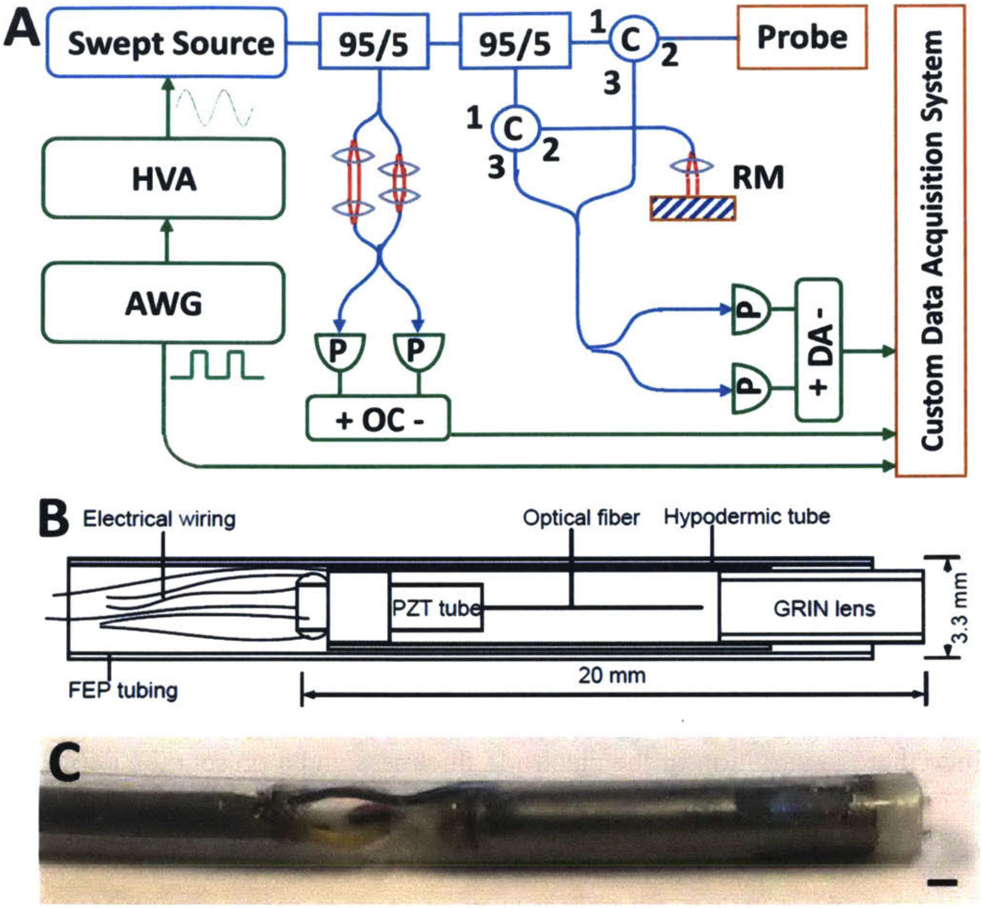

Fig. 1. (A) Ultrahigh speed OCT system. HVA: high voltage amplifier, AWG: arbitrary waveform generator, P: photodetector, C: circulator, RM: reference mirror, OC: optical clock, DA: differential amplifier. (B) Schematic and (C) photo of forward viewing probe (scale bar 1 mm).

The resonant fiber scanning probe (Fig. 1B-C) was similar to previous devices[59, 60, 64]. An optical fiber was mounted to the tip of a piezoelectric (lead zirconate titanate) tube (Boston Piezo-Optics, Bellingham MA) of 6 mm length, 1.5 mm outer diameter, 0.3 mm wall, and quartered electrodes for 2-axis actuation. <20 mm rigid length of the probe was necessary for passage through the 3.7 mm endoscopic accessory channel; therefore, piezoelectric actuator length was minimized, costing a reduction in actuating range. The fiber was aligned to a 1.8 mm diameter gradient index lens (Go!Foton, Somerset NJ) for 1:1 magnification to the focal plane (~200 μm deep in tissue contacting with lens). The piezoelectric actuator, optical fiber, and lens were housed in a 12G hypotube. The entire device was encapsulated in American Wire Gauge 9 fluorinated ethylene propylene tubing (Zeus) with no exposed conductive surfaces, and sealed watertight using medical epoxy.

The piezoelectric tubular actuator was commercially available (e.g. Boston Piezo-Optics). At this dimension (1.5 mm OD and smaller), electrically separate electrodes on the outer surface are typically unavailable; the tubes are shipped with the outer surface uniformly metallized. The tubes were sent out to a separate vendor for laser etching of the electrodes. The depth of etch was selected based on the piezoelectric actuator vendor's specification of the electrode thickness (Fig. 2). The laser etching vendor was asked to verify electrical isolation of the electrode sectors after each etch, since there is variation in the electrode thickness and a preset etch depth may not fully separate the sectors.

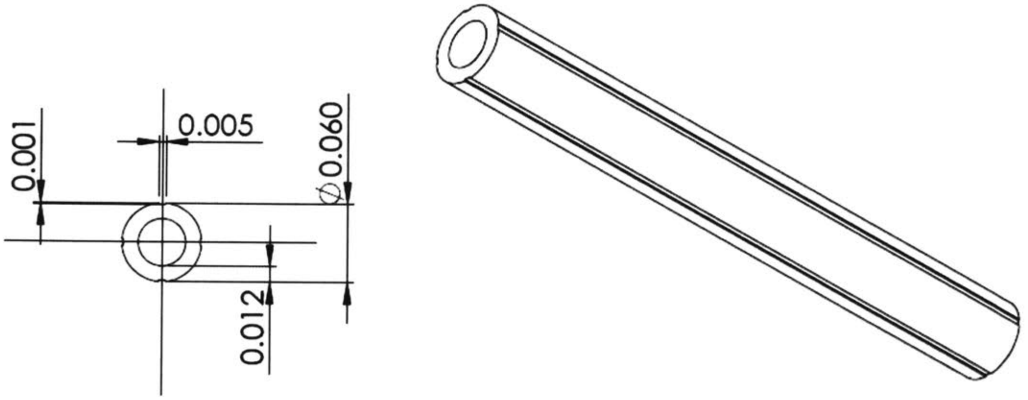

Fig. 2. Dimensions (inches) of piezoelectric tube cross section and etch specifications.

The piezoelectric tube was hand-soldered under a magnifier to a multi-conductor cable (Cooner Wire) with 4 connections to each electrode and one earth connection to the metallic hypotube housing. Soldering to the piezoelectric tube's nickel electrode required a specialized flux

(Superior Flux) and so did soldering to the stainless steel housing (LA-CO flux). Care was taken to solder to the nickel at around 500°F (under 600°F) to prevent oxidation. The piezoelectric actuator was driven by waveforms from a 4-channel current limited 50x amplifier. This amplifier circuit was previously constructed by Tsung-Han Tsai PhD based on designs from Prof. Xingde Li's group. The output voltage after amplification was 40 V peak amplitude A.C., within the recommended limit (42 V_p) from the International Electrotechnical Commission 60601-1 medical electrical apparatus standards[65]. Electrodes on the actuator were precision laser etched (Laser Impressions, Sunnyvale CA) for symmetric actuation. It was also important for the fiber mount to be centered and symmetric in the tube, so that resonance frequency and amplitude would be similar in both axes. The fiber was centered in the tube with a ring jewel bearing (Swiss Jewel, Philadelphia PA) and fixed with heat-cured epoxy for optimal rigidity, ensuring a high (>100) resonant quality (Q) factor. The ring jewel was custom fabricated with a center hole very closely fitting the diameter of 125 μm stripped bare fiber, and outer diameter very closely matching the inner diameter of the piezoelectric tube. The resonating fiber deflection was measured using a consumer webcam CCD sensor fitted with a microscope objective.

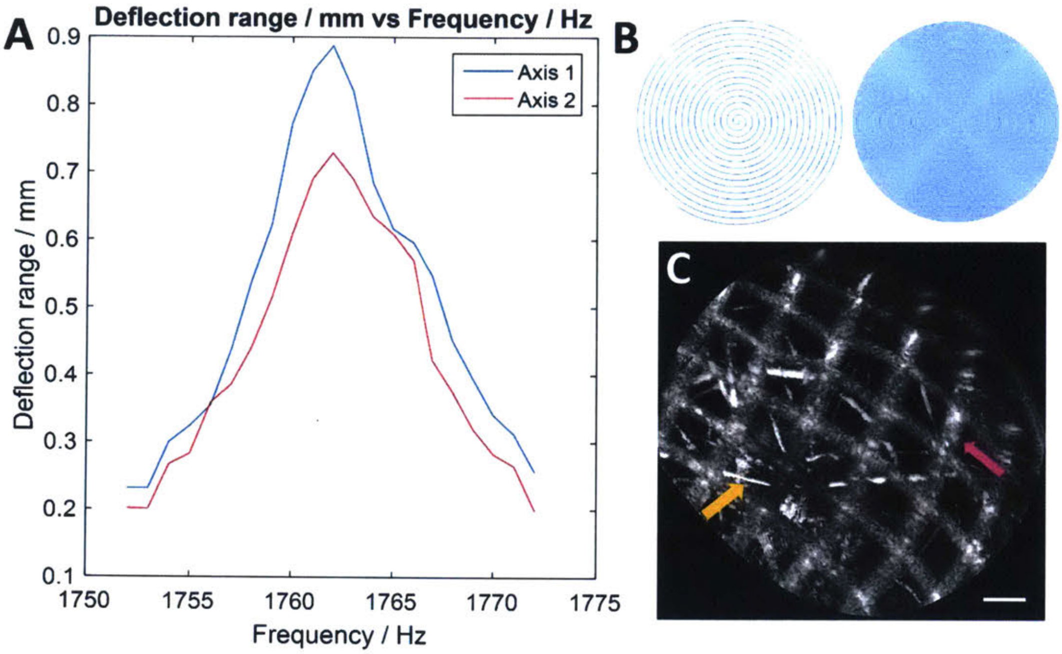

Fig. 3. (A) Frequency response of the fiber scanner. Range refers to the scan diameter (peak to peak deflection). (B) Illustration of spiral scan showing sparse/dense sampling. (C) *En face* OCT image of a nylon grid (pink arrow) of pitch 140 μm placed over an absorbent fiber pad (orange), acquired with the probe (scale bar 100 μm).

The scanner resonance frequency was determined by fiber length, estimated using the fixed-free cantilever formula[64]:

$$f = \frac{\pi}{16}\sqrt{\frac{E}{\rho}}\frac{R}{L^2}(1.194^2)$$

$E = 72GPa$ and $\rho = 2200kg/m^3$ are the Young's modulus and mass density of fused silica, $R = 63\times10^{-6}m$ is the radius (for standard SMF-28 fiber) and L is the length of the fiber cantilever, and 1.194^2 is a numerically obtained constant representing the fundamental vibration mode. The fiber length was 7.5 mm, producing a theoretical resonant frequency of ~1800 Hz on the fast circular scan. A useful rule of thumb for the resonant frequency is $f = \frac{0.1}{L^2}$ which can be obtained simply by plugging in the values of the constants.

The piezoelectric tube has a deflection width governed by the following:

$$\Delta y = \frac{2\sqrt{2} d_{31} V L^2}{\pi D h}$$

V is the voltage, L is the length of the tube, D is the outer diameter, h is the wall thickness, and d_{31} is a piezoelectric constant relevant to the material, which is about 300 x 10^{-12} m/V for the tube used (PZT-5H material). The fiber deflection depends in part on the fiber material, length and resonance response and is thus not exactly proportional to the tube deflection, however there is similar linear dependence with voltage. The fiber scanned a ~900 μm diameter, which was equal to the field of view (FOV) at 1:1 magnification. The 9 μm mode field diameter ($1/e^2$) of SMF-28 gave 5 μm full-width at half maximum (FWHM) transverse resolution and ~600 resolvable spots on the outermost circle. At 1 MHz A-scan rate, each resonant period had ~600 A-scans, such that the outermost circle was sampled at half-Nyquist (5 μm pitch). Each volume had 300 circular scans; the FOV radius was ~450 μm (~90 resolvable spots), therefore the slow radial axis was sampled at 3x Nyquist. For OCTA, volumes were acquired at half the scan field (~450 μm diameter), such that the outermost circle was Nyquist sampled, and the slow axis sampled at 6x Nyquist.

After probe assembly was completed, the fiber was scanned in a spiral and the trajectory assessed using a position-sensitive detector (PSD, On-Trak, Irvine CA). The phase difference and amplitudes of the two axes driving the fiber were tuned for optimal circularity[60]. The trajectory measured by the PSD was recorded and used to generate a nearest neighbor look-up table (LUT) for converting the spiral to a 512x512 Cartesian grid. The nearest neighbor interpolation did not account for oversampling, thus multiple ‘nearest’ samples were not averaged. The trajectory was stable regardless of probe orientation, and re-calibration was required after 1-2 weeks. Each volume was acquired in 0.17 sec, and processed by the acquisition software (C++) for *en face* display before the next acquisition. The volume was acquired with the fiber actuated with increasing amplitude (outward spiral) because an inward spiral did not follow the drive waveform phase accurately. The spiral had 300 circular scans, which at ~1800 Hz frequency amounted to a volumetric acquisition time of 0.17 sec and acquisition rate of ~6 volumes/sec. However, the repeat volume rate was limited by time required for the fiber to damp naturally, an additional ~0.2 sec. Processing introduced a further delay resulting in ~2 volumes/sec rate. Improving processing and damping times would allow the true volumetric display rates to approach acquisition rates. Processing of spectral data was performed in MATLAB. Each OCT volume was remapped to the spiral using the LUT. Cross-sectional images analogous to traditional B-scans were extracted from the remapped volumes. OCT angiograms were post-processed and calculated by intensity decorrelation[52, 66] of the raw circular scans, which did not require registration. Remapping was performed after decorrelation. OCT volumes were used to generate OCTA, therefore the OCT and OCTA images were intrinsically co-registered at all depths.

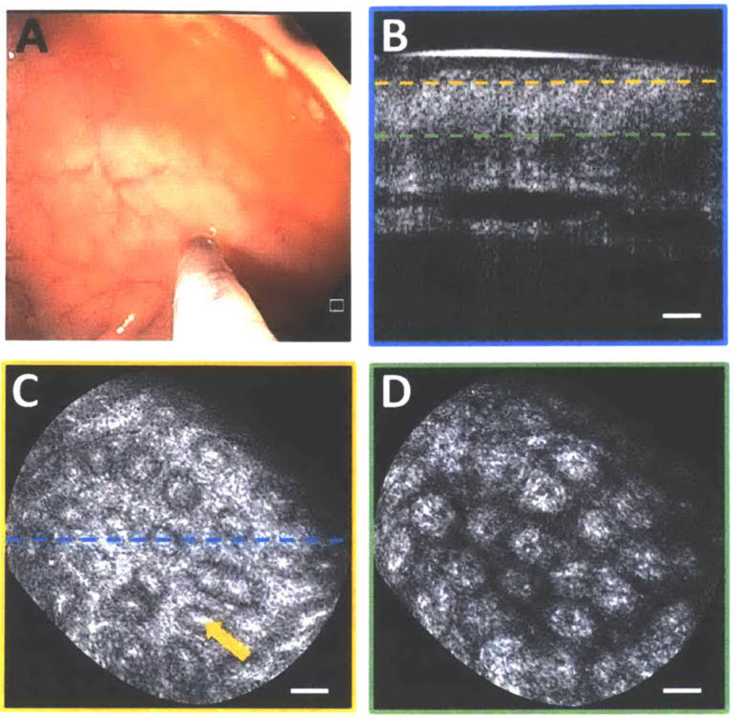

Fig. 4. (A) Endoscopic image showing probe in contact with normal colonic mucosa. (B) Cross section of OCT volume acquired. *En face* OCT slices of 40 μm depth mean intensity projection at (C) 40 μm depth and (D) 200 μm depth in tissue (dashed lines indicate depth) showing crypt lumens (orange arrow). Scale bars 100 μm.

Imaging was performed at the Veterans Affairs Boston Healthcare System (VABHS) with IRB approvals at the Massachusetts Institute of Technology, VABHS, and Harvard Medical School, and written informed consent obtained. Inclusion criteria was colonoscopy. The probe was introduced into the accessory channel and placed in gentle contact with ROIs in the endoscopic view to minimize compression. Multiple volumes were acquired at each location to overcome potential imaging artifacts from bulk motion.

Results and Discussion

The fiber scanner had a measured resonance of 1762 Hz (Fig. 3A). The resonance peak frequency for either axis was the same; however, the amplitude for one axis was lower at the same driving voltage. This might be related to asymmetry in fiber mounting or etching of actuator electrodes. It was possible to reduce amplitude on one axis to improve circularity; however, it was preferable to optimize FOV. Fig. 3C shows a test image of a nylon grid placed on top of an absorbent fiber pad, just before the endoscopy. The probe was held by hand and placed in contact with the grid. The image had stable reconstruction of the grid, with minor distortions due to the non-telecentricity of the field. The resolution was sufficient to visualize the absorbent fibers that were tens of microns thick.

Imaging was performed on normal colonic mucosa (Fig. 4). Cross-sectional OCT images showed vertically projecting features associated with colonic crypts. The *en face* plane at shallower depth showed circular/elliptical crypts, and structural features reminiscent of crypt lumens. At deeper depths, OCT shows integrated effects of light propagation/backscattering; crypt walls produced high OCT signal, while lumens and stroma produced dark vertical features, resulting in contrast inversion[54]. Imaging of a benign hyperplastic polyp (Fig. 5) showed regular crypts but slightly enlarged and more sparsely distributed, in this single illustrative example. OCTA of the polyp (Fig. 6) showed vascular patterns varying with depth and encircling the crypts.

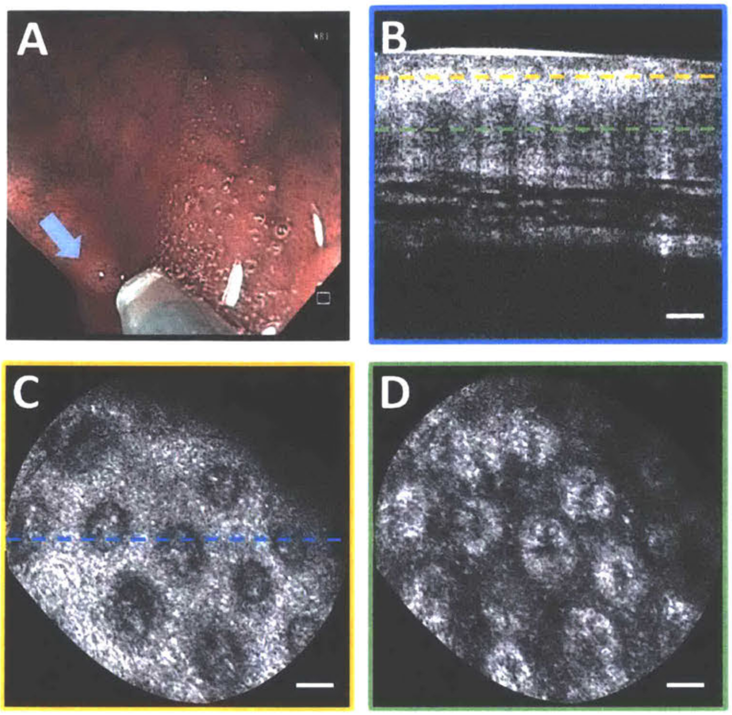

Fig. 5. (A) Endoscopic image showing probe coming into contact with hyperplastic polyp (arrow). (B) Cross section of OCT volume from polyp. *En face* OCT slices of 40 μm depth projection at (C) 40 μm depth and (D) 200 μm depth showing enlarged crypts. Scale bars 100 μm.

In endoscopic and minimally invasive scenarios using catheters, 2-D distal actuation for scanning is attractive. The repeat volume rate in this study was limited because of the time for the fiber to damp before rescanning (Fig. 7). A large resonant deflection was required to maximize FOV, but the high Q resonance produced a ~0.2 sec damping time, limiting the volume rate. The fiber resonant motion may be actively damped by driving with a waveform of the opposite quadrature, but accurate phasing is required[60]. Graphics processing units could reduce the processing delay.

Forward viewing devices are an important complement to side viewing. While side viewing probes have large FOV, they are inefficient for targeting small regions flagged on the endoscopic view and requiring a closer look. Proximal scan errors exacerbate the difficulty of visualizing small regions. Forward viewing has small FOV but is suited for close-up inspection.

The resolution of scanning fiber devices depends on the number of resolvable spots, which is calculated from the fiber mode field diameter and the scan range. Constraints of the probe rigid length and driving voltages impose a limit on resolvable spots. Smaller actuators (~400 μm diameter) have been reported[60] but are not yet commercially available. Deflection is inversely proportional to tube diameter and wall thickness[67]; smaller actuators scan larger fields for a given voltage, which will increase resolvable spot numbers and relax requirements for high Q factors. With improvements made to the assembly process and more experimentation with various epoxy options, it should be possible to achieve more precise control of the fiber mount rigidity and resultant Q factor. More conservative Q factors will reduce ring-down time of the fiber resonator and potentially improve scan reset rates.

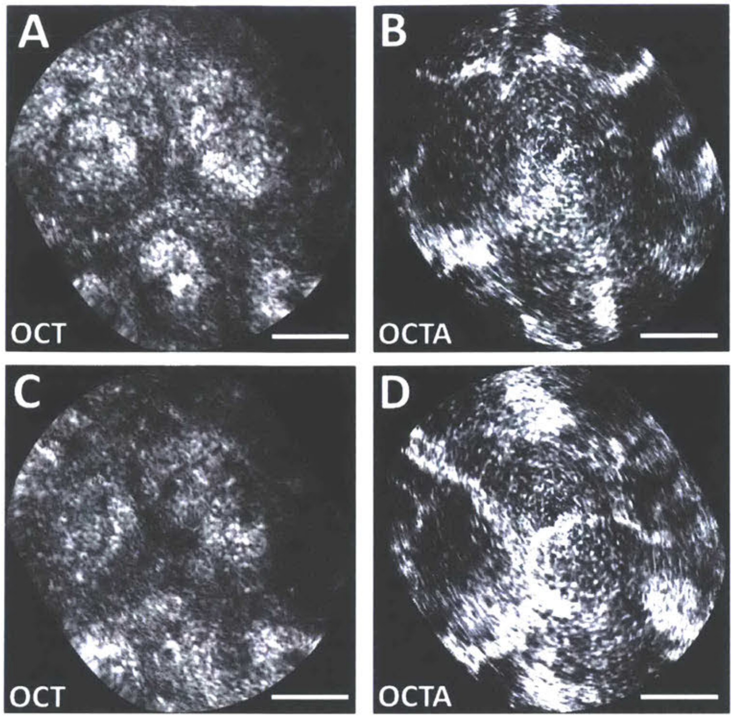

Fig. 6. Zoomed *en face* OCT images at (A) 150 μm and (C) 200 μm depth (40 μm depth projection) of polyp. Intrinsically co-registered, depth-resolved OCT angiography from (B) 150 μm and (D) 200 μm depth showing vascular morphology. Scale bars 100 μm.

The resonant scan sampled at constant angular velocity, such that sampling decreased with increasing radial distance. While this resulted in non-uniform sampling, it enabled sequential circular scans to be decorrelated to generate OCTA because the spots were radially aligned. The fast resonance produced scan overlap, but the short (0.57 ms) interscan time reduced sensitivity to slow flows in small vessels. Constant linear velocity would produce uniform sampling but cannot easily generate OCTA. Although there was oversampling in the fast axis towards the center due to decreasing length of the circular scans, the latter increased uncertainty in scan-to-scan alignment; therefore, decorrelation noise did not necessarily decrease towards the center. Noise artifacts mimicking the spiral were likely due to small synchronization errors between the laser and scanner, and small parasitic motion.

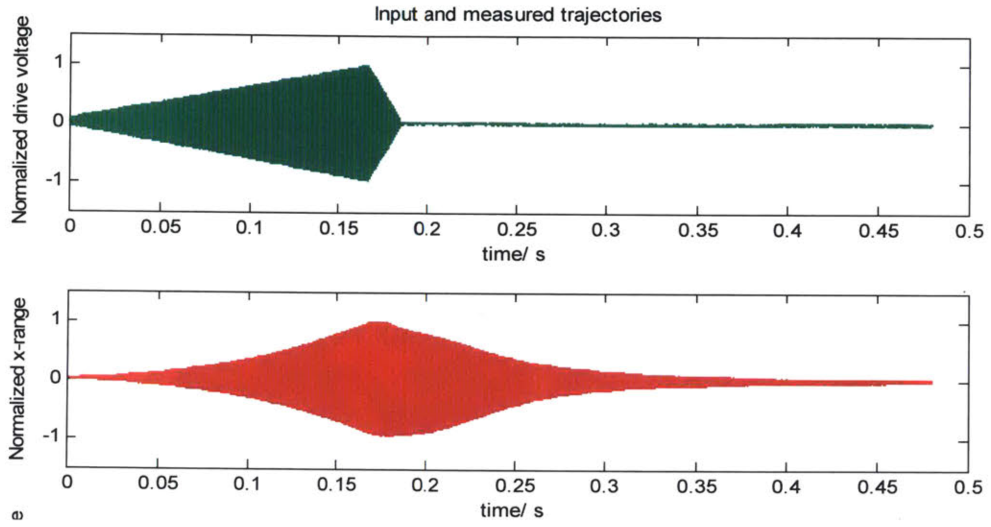

Fig. 7. Illustrative figure from the author's Master's thesis [68] showing the input ramp drive to a piezoelectric actuator and the resultant resonant response from a deflecting fiber. There is a long decay time related to the fiber damping.

In GI endoscopy, the concept of 'resect and discard' i.e. assessing polyps to be benign *in situ* and discarding them without histopathological analysis is gaining traction as a potentially more cost-effective surveillance protocol, given the significant cost of histology processing[69]. The polyp in this study did not exhibit marked structural anomalies on imaging, and later showed benign histology. In this context, forward viewing OCT has promise in providing real-time tissue assessment during endoscopy.

Ultrahigh speed OCT at 1 MHz A-scan rate with a forward viewing probe generated high quality volumetric and *en face* images of colonic microstructure and vascularity. Future work will assess adenomas and other colonic pathology to assess the diagnostic potential of forward viewing OCT in GI surveillance.

Chapter 3

Ultrahigh speed OCT capsule for *en face* imaging: studies in swine

Introduction

Catheter based optical coherence tomography (OCT) enables high resolution, volumetric imaging of organ surfaces and luminal walls [50]. The rapid advancement and speed improvements of wavelength swept laser sources [70] enable *in vivo* three-dimensional (3D) OCT imaging at high frame rates. Increases in laser sweep rate have been accompanied by advances in optical scanning probe technologies. Early work with swept source OCT (SS-OCT) and a rotary scanning fiber optic probe with pullback demonstrated the feasibility of generating 3D gigavoxel image volumes [36, 37]. Later SS-OCT studies used novel probe designs such as a balloon catheter [38, 39, 71], MEMS scanner [72], and resonant fiber scanning [59, 61, 73]. The distally scanning micromotor OCT probe was first demonstrated a decade ago [74, 75] and more recently, multiple groups have achieved high frame rate 3D-OCT imaging over large fields using micromotor scanners [76-78]. Using ultrahigh speed MEMS tunable VCSEL laser technology and micromotor scanners, our group recently demonstrated endoscopic OCT angiography (OCTA) and *en face* OCT in the upper and lower gastrointestinal (GI) tract in human subjects [52, 79].

However, rotary scanning to acquire volumetric data in a luminal organ has traditionally been performed using a proximal motorized pullback for the longitudinal, slow scan direction. Proximal actuation transmits force via a long tether, such as a torque cable, which is subject to mechanical deformation such as stretching and twisting. This limits the actuation stability at the distal end of the probe and degrades scan accuracy along the longitudinal axis. Probes with distal resonant fiber scanning have been widely investigated [59-61, 80], but the scan speed is not adjustable, image sampling is non-uniform because of the need for resonant scan patterns such as the spiral or Lissajous, and imaging is primarily in the forward direction. Two-dimensional (2D) non-resonant fiber scanners have been developed [81-84], but typically require high voltage actuation for the non-resonant axis/axes, which could limit clinical utility. A novel side-viewing probe based on the piezoelectric 'squiggle' motor achieved 2D distal side scanning using a rotating leadscrew [85], but the scan axes could not be controlled independently.

Wireless capsule endoscopy is a well-known and clinically accepted modality for comprehensive imaging of the entire gastrointestinal tract [86]. However, the wireless capsule travels rapidly down and away from the esophagus, and it is not possible to slow down or steer the device for high resolution, closer inspection of the esophageal wall. It was found that simply tying a string to a capsule endoscope was a useful and well tolerated method for diagnosing Barrett's Esophagus (BE) with good diagnostic sensitivity [87-89]. Seibel et al. developed a tethered capsule endoscope with forward viewing capability based on resonant fiber scanning which could perform white light imaging of the esophageal wall at video rates [90, 91]. The tethered capsule had the advantage that it could be swallowed by unsedated patients for screening applications, without the need for conventional endoscopy which requires sedation. More recently, the tethered capsule concept was demonstrated using SS-OCT for circumferential 3D OCT imaging [92], as well as spectrally encoded confocal microscopy [93]. These devices had a highly flexible and soft tether that was shown to be easily swallowed and well tolerated by patients [94]. In this design, the distal optics were scanned in the rotary direction via a proximally actuated torque cable and the capsule was allowed to passively traverse the esophagus by peristalsis, then manually retracted (pullback) by the soft tether in order to scan the longitudinal extent of the esophagus. Manual pullback in order to perform the longitudinal scan is rapid and convenient in a screening context, but may not be stable or precise enough to achieve high resolution volumetric OCT for *en face* OCT, especially at limited frame rates supported by proximal torque cable actuation. In addition, precision longitudinal beam scanning is required for scanning microscopies such as confocal, fluorescence or multiphoton microscopy imaging. Therefore, there is a need for device technologies which can perform high speed rotary beam scanning combined with precision longitudinal scanning, maximizing image quality and reducing intraluminal device time.

En face features in the GI tract, such as mucosal surface patterns or 'pit patterns', are known markers for disease [24, 95]. The ability to resolve these patterns with *en face* OCT could improve diagnostic sensitivity. However, image quality depends on optical resolution and scan pattern repeatability. Accurate and stable beam scanning enables imaging of structural features in the *en face* plane, as well as more advanced functional methods such as OCTA [51]. Previous probe designs for circumferential luminal scanning such as balloon and capsule catheters were limited by scan instability due to proximal rotary and longitudinal actuation, and relatively poor transverse resolution because the optics have to be centered in the large diameter probe. Small diameter probes can have better transverse resolution, but cover only a limited portion of the luminal circumference, such that multiple pullbacks over different sectors of the esophagus are required to survey the entire circumference.

This chapter describes a capsule probe that incorporates 2D circumferential and longitudinal beam scanning in the distal end, thus eliminating mechanical instability from proximal torque cable actuation. The device has a 3.8 mm diameter tether that is semi-rigid to allow manual positioning, pulling back or advancing the device, depending on the mode of operation, such that peristaltic propulsion is not necessarily required. The rotary scanner is a micromotor, and the longitudinal scanner is a novel pneumatic actuator. The optical design enables focusing elements to be positioned close to the tissue surface, to improve transverse resolution. Additionally, the path length of the OCT sample arm is designed to vary with the longitudinal pneumatic scan, enabling non-uniformities in the longitudinal scan trajectory to be tracked and corrected in post-processing. The longitudinal scan can also be performed by proximal manual actuation of the entire capsule (large field coverage) via the tether, versus by distal pneumatic actuation of an internal carriage with the capsule kept stationary (small field, high stability inspection). Compared to our previously reported micromotor probe [77], the capsule probe has significantly improved field of view and 2D distal scanning capabilities. Images were acquired in the living swine esophagus, rectum, and anal canal. This study serves as an important translational step in validating the ultrahigh speed capsule OCT technology for potential clinical applications in screening and surveillance. In particular, the ability to image a wide range of field sizes, in both the upper and lower GI tract, and in sedated subjects promises to enable new applications of OCT as a next-generation GI imaging modality.

Materials and Methods

This work was performed in collaboration with Dr. Giovanni Traverso and veterinary staff at the MIT Division for Comparative Medicine, Thorlabs (Dr. Benjamin Potsaid) and Praevium Research (Dr. Vijaysekhar Jayaraman) for use of prototype swept source technology.

Imaging system

The OCT system used a dual circulator Michelson interferometer as shown in Fig. 1. The data acquisition card (AlazarTech, Quebec, Canada) had 12 bit resolution and was rated at up to 1.8 GS/s with internal clocking, but was limited to lower sampling rates when externally clocked. The acquisition card was optically clocked by a Mach-Zehnder interferometer with a variable fringe frequency of up to 1.1 GHz, which was the maximum frequency that the A/D card could perform variable clocking. The laser source was a 1300 nm MEMS-based vertical-cavity surface-emitting laser (VCSEL) [63], and was driven sinusoidally at 500 kHz by an arbitrary waveform generator and high voltage amplifier. Both forward and backward wavelength sweeps of the laser were used to achieve an effective axial scan rate of 1 MHz. The VCSEL sweep bandwidth was 115 nm, the measured axial resolution was 12 μm in air (8.5 μm in tissue), and the Nyquist imaging range was 2.3 mm in air (1.6 mm in tissue). Sensitivity roll off was negligible across the imaging range because of the long coherence length of the VCSEL and high bandwidth of the detectors. The coherence length of the VCSEL has been previously reported to be more than 100 mm in air [96]. The power emitted from the imaging capsule was 35 mW. System sensitivity was measured using an isolated reflection from a flat-cleaved fiber patch cord with 0.6% reflectivity, with additional attenuation from a 17 dB single pass attenuator in the sample arm. The sensitivity was measured to be 105 dB, defined by the ratio of the OCT signal to the standard deviation of the magnitude of the OCT signal with the reflection blocked. The transmission through the capsule probe was 70 percent. The backcoupling efficiency of a mirror reflection into the probe was estimated to be 50 percent. The effective sensitivity of the OCT imaging engine with the capsule was ~102 dB.

A custom C++ software was used to control the beam scanning and data acquisition. The OCT interferometer reference mirror was on a motorized translation stage that was triggered by the acquisition software at a preset timing delay. The translation range of the pneumatic actuator in the capsule is about 3.5 mm, which is larger than the system imaging range. Thus, the reference mirror position was scanned at a speed matched to the maximum speed of the pneumatic actuator, in order to enable imaging over the full longitudinal translation range. The system was installed on a portable cart for convenient transport to the animal housing facility for imaging experiments.

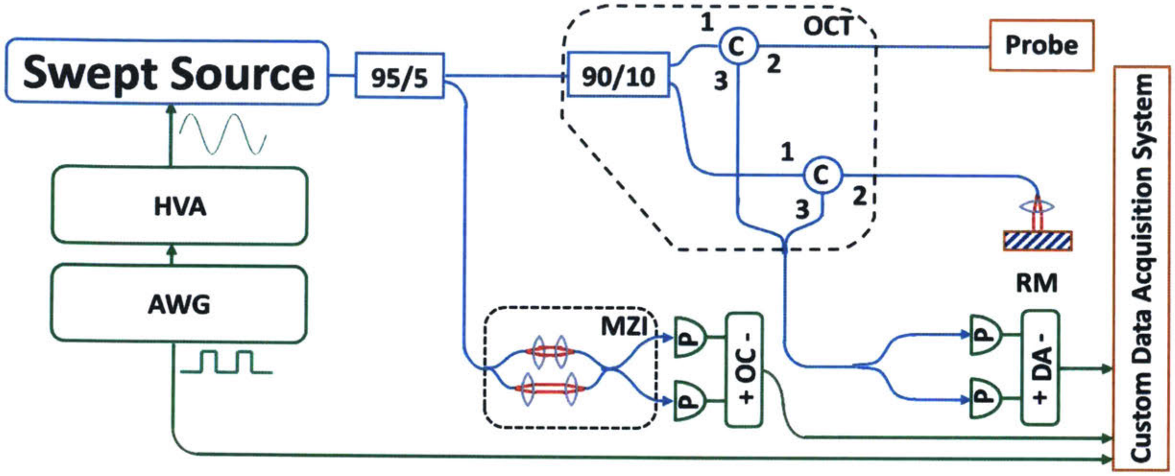

Fig. 1. Schematic of OCT system. HVA: high voltage amplifier; AWG: arbitrary waveform generator; MZI: Mach-Zehnder interferometer; OC: optical clock; RM: reference mirror; DA: differential amplifier.

Catheter design and assembly

A schematic of the capsule device is shown in Fig. 2(a), and photographs in Figs. 2(b) and 2(c). A collimated beam was reflected at a right angle by a prism and focused by a microlens to a focal plane outside of the glass tube enclosure. The microlens was mounted on a counterweighted lens holder on the shaft of a micromotor. The micromotor rotated the lens holder to circumferentially scan the focused beam. The micromotor was mounted on a carriage, which was centered in a glass tube by multiple contact points with non-marring set screws. The carriage was attached to a bellows that was expanded and contracted by pneumatic inflation and deflation via an inflation tube. When the bellows was actuated, the carriage slid smoothly along the glass tube, generating a precision longitudinal scan.

A commercially available, low cost miniature fiber coupled collimator (AC Photonics, CA) with 1.4 mm diameter and 6 mm rigid length was used to generate the input beam. The objective was a stock telecom-coated planoconvex lens (Edmund Optics) with 2.0 mm diameter and 4.0 mm focal length. The objective was mounted in a lens holder that was rapid-prototyped by high resolution stereolithography (SLA) (In'Tech Industries, MN). The material used was Accura 25, a proprietary SLA-specific material that has ABS-like properties. A stock 2.0 mm prism was mounted in a square hole in the center of the lens holder. The prism was angled at 6 degrees to minimize backreflections from the glass tube surface into the collimator. The lens was counterweighted by an identical lens to minimize vibration during rotation. The focal plane was located 1 mm from the glass surface assuming tissue contact, with a 26 μm full width at half maximum focused spot diameter.

The lens holder was designed and rapid-prototyped such that the prism and lens were aligned. The collimator (centered in the torque cable and mounted in the center of proximal end cap) and lens holder (mounted on the micromotor shaft and centered in glass tube) were also aligned coaxially. High precision, rapid-prototyped parts enabled the optical components to be self-aligning when assembled. In this design, longitudinal translation of the optical assembly varied the optical path length in the OCT interferometer sample arm, but did not change the focal plane of the optical system. This path length variation enabled the OCT instrument to precisely measure the longitudinal position of the carriage assembly.

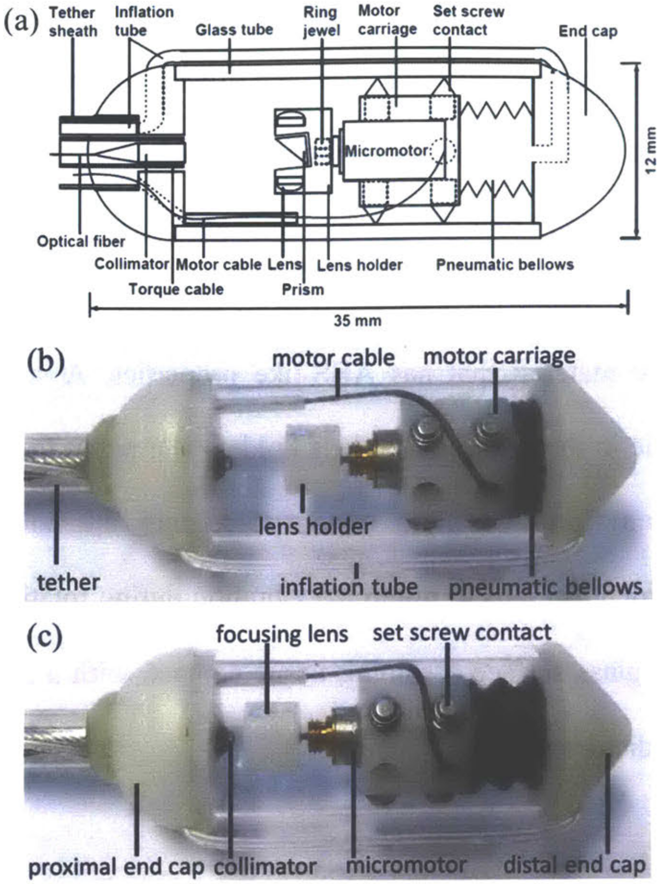

Fig. 2. (a) Schematic of capsule. Photographs of capsule with motor carriage at (b) beginning position and (c) ending position of the longitudinal pneumatic scan.

The end caps of the capsule were also rapid-prototyped. The proximal end cap had internal channels for the micromotor electrical cable and pneumatic inflation tube, and an extruded slot for management of the electrical cable over the imaging region. The distal end cap had an L-channel for passage of air or other fluid. A glass tube with outer diameter 12.0 mm and inner diameter 10.0 mm was cut to length with a diamond saw from stock fused quartz tubing (Technical Glass Products, OH). Glass was chosen for high optical clarity and close dimensional tolerances of commercial manufacturing. Future iterations designed for human use would use medical grade plastics. An elastic nitrile bellows was cut to length and attached on one end to the distal end cap such that the bellows could be pneumatically inflated via the L-channel. Kink-resistant Tygon tubing with outer diameter 0.8 mm (US Plastic Corp, OH) was attached to the opening of the L-channel, folded back outside the glass tube and inserted into a channel on the proximal end cap.

A brushless DC micromotor with 4 mm diameter (Namiki Precision, CA) was mounted in the center of a rapid-prototyped carriage. The carriage was designed with 2 sets of 3 through holes spaced radially apart. The holes were tapped through for 2-56 thread non-marring set screws. The set screws were screwed into the through holes such that the tips emerged from the opposing side, producing 2 parallel sets of 3 radially distributed contact points. In order for the diameter of the carriage with set screw contacts to match the inner diameter of the tube, a simple alignment tool was constructed. A short segment of glass tube was fitted on one end with a closely toleranced Teflon insert. The insert was drilled with a 4 mm through hole. To align the set screws on the carriage to the inner diameter of the glass tube, the carriage was temporarily mounted on a 4 mm rod, which was slid smoothly through the Teflon insert such that the carriage could be slid into the alignment tube while centrally aligned. The radial protrusion of each set screw could then be systematically tuned with a wrench until the carriage was found to slide smoothly yet snugly through the alignment tube. The protrusions of each set screw were carefully optimized such that the carriage was well centered in the glass tube and were then fixed in position with adhesive. The carriage was then affixed to the open end of the bellows. To check for leaks, the carriage-bellows assembly was fully immersed in water and the bellows inflated. Leaks were sealed with adhesive.

After the bellows and carriage were assembled, the motor was mounted in the carriage, and the motor cable passed through one of the unused threaded holes on the carriage. The motor shaft was fitted with a precision jewel bearing (Swiss Jewel, PA), which allowed accurate mounting of the lens holder on the central axis of the motor. The collimator was centered in a torque cable of outer diameter 1.9 mm (ACTONE, Asahi-Intecc, Japan) that was then centered in the proximal end cap. The torque cable was used to increase the tether rigidity and was not used for any internal actuation. The carriage was qualitatively evaluated for low friction actuation, radial or angular fit, and alignment with the collimated beam. The laser spot was verified to be circular by a beam profiler (DataRay Inc., CA). Both end caps were snap fitted with adhesive on each end of the glass tube. Proximal to the capsule, the optical fiber, motor cable and inflation tubing were organized into a bundle that was passed through an FEP AWG8 tubing (Zeus Industrial Products, SC), which was then affixed to the proximal end cap of the capsule. At the proximal end of the entire tether, the optical fiber and motor cable were connectorized. The inflation tube was connected to a female Luer lock fitting and 20 mL syringe containing air, which was actuated by a motorized linear translation stage modified to work as a syringe pump.

Scan actuation and characterization

The rotary speed of the motor was set according to the spot size, capsule circumference and axial scan rate. For a 26 μm (FWHM) focused spot and $\pi \times 12$ mm ≈ 38 mm circumference, ~3000 axial scans per revolution were required for Nyquist sampling. At 1 MHz A-scan rate, this corresponded to a maximum rotary speed of 330 Hz. The motor was driven at 250 Hz, sampling at 1.3 times Nyquist, with a three-phase D/A output (National Instruments) to an audio amplifier. In the longitudinal scan direction, the Nyquist translation speed was $\frac{1}{2} \times 26$ μm $\times$ 250 Hz = 3.3 mm/s. The syringe pump for the pneumatic actuation generated a maximum longitudinal carriage translation speed of ~1 mm/s, sampling at 3 times Nyquist. The longitudinal speed could be increased with a larger syringe or a faster translation stage. The capsule was hermetically sealed, therefore there was a pressure build up and significant infusion pressure was required to expand the bellows within the capsule. This limitation can be addressed by future redesigns. Figs. 2(b) and 2(c) show the pneumatic actuator in the start and end positions. The varying path length during longitudinal scanning of the carriage could be used to track the precise position of the carriage. The actuator had an acceleration phase, a near constant-speed phase, and a deceleration phase. The longitudinal actuator could be improved in the future by using hydraulic actuation to reduce the non-uniform speed artifacts.

The longitudinal scan position and trajectory (Fig. 3(a)) were obtained by automatically detecting a reflection from the glass tube (Fig. 5) that was present in all frames, and measuring the frame to frame longitudinal translation. A ramp offset was then added to account for the constant speed translation of the reference mirror, to obtain the actual carriage displacement. The noise in the trajectory plot was generated by micromotor vibration that produced small displacements in the longitudinal direction as well as segmentation errors. The compressibility of the air in the bellows resulted in the vibrations being undamped. A linearized trajectory was obtained by smoothing the measured trajectory with a moving average filter and fitting a line to the central, nearly linear portion. Before longitudinal distortion correction, the frames were circular-shifted to the same interferometric delay by using the reflection from the glass tube. Frames were then interpolated by cubic spline to the linearized trajectory to correct for longitudinal distortion from the nonlinear longitudinal actuation. For each pneumatically scanned dataset, the longitudinal trajectory from that dataset was obtained and used to correct distortions. All data post-processing was performed in MATLAB (MathWorks, MA). Fig. 3(b) shows the filtered and linearized trajectory used for the spline resampling. Figs. 3(c) and (d) show an image of rectal crypts, before and after longitudinal position correction, respectively. Both images appear similar in the central region corresponding to the pneumatic near-constant speed phase, but the regions corresponding to the acceleration and deceleration phases are distortion-corrected.

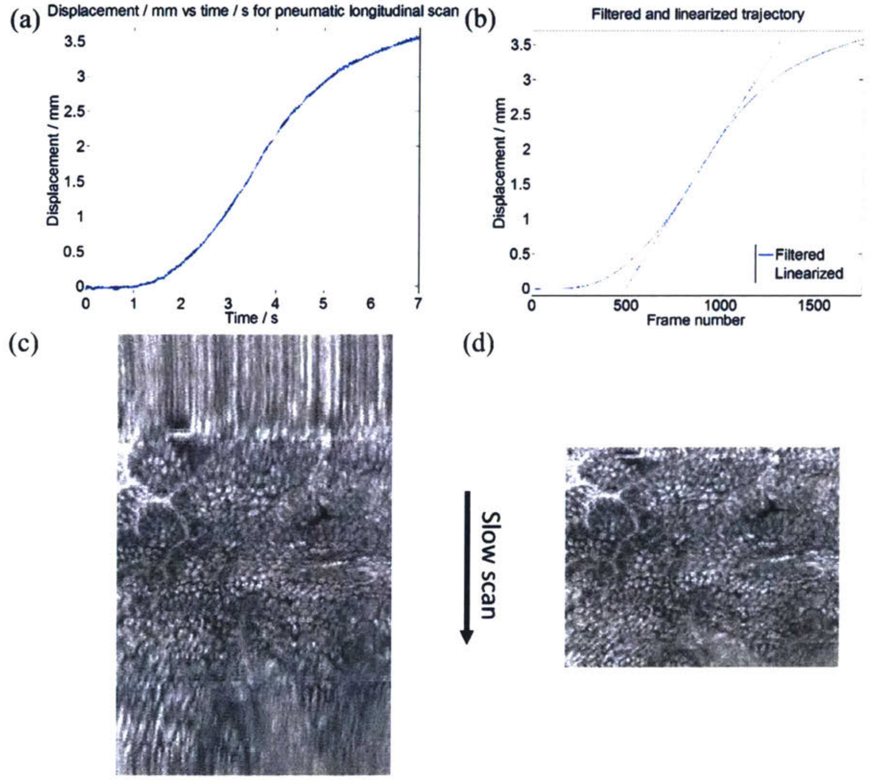

Fig. 3. (a) Measured trajectory of longitudinal pneumatic actuator. Maximum translation speed was ~1 mm/s. (b) Filtered and linearized longitudinal trajectory for spline resampling. Zoomed portion of an endoscopic *en face* OCT image of the rectum (c) before and (d) after correction.

Animal imaging procedure and scan protocols

Imaging was performed under protocols approved by the Committee on Animal Care (CAC) at the Massachusetts Institute of Technology. Three Yorkshire swine of approximately 50 kg were imaged in two sessions with the same capsule device. Sedation in the swine was induced with intramuscular injection of 5 mg/kg telazol and 2 mg/kg xylazine, and atropine at 0.04 mg/kg was given to maintain heart rate after sedation and to control mucus secretions. For upper GI imaging, a 16.7 mm inner diameter overtube (US Endoscopy, OH) was slid over and up to the proximal end of an endoscope (Pentax Medical) before introduction into the animal. The endoscope was then introduced into the esophagus, the overtube slid over and into the esophagus from the distal end of the endoscope, and the endoscope withdrawn from the esophagus, leaving the overtube in place. The capsule was introduced directly into the overtube by advancing the semi-rigid tether. The overtube was then withdrawn from the esophagus and mouth, and slid up to the proximal end of the tether. Thereafter, the distal end of the probe could be longitudinally positioned by advancing or retracting the semi-rigid tether. For lower GI imaging, a tap water enema was administered to clear the rectum of stool. The capsule was then inserted via the anal canal and then advanced forward using the tether into the rectum. X-ray images (Hudson Digital Systems, NJ) were acquired to confirm positioning of the capsule in the upper and lower GI tract (Fig. 4).

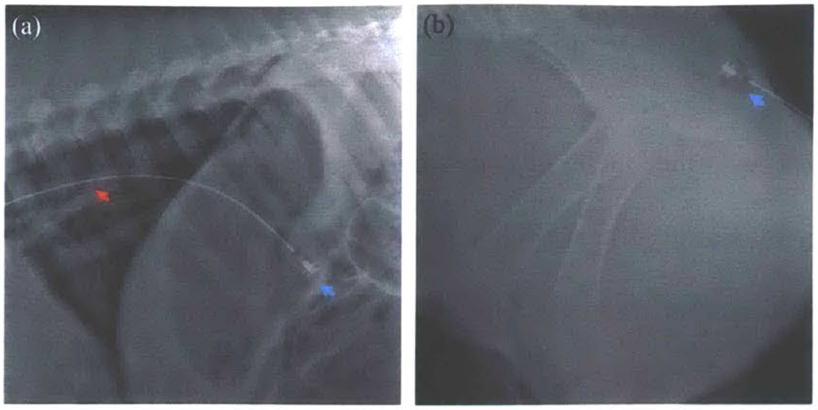

Fig. 4. Representative X-rays showing the position of the capsule in the (a) stomach and (b) anal canal. The tether (red arrow) and capsule (blue) are indicated.

For 2D distal scanning, the capsule was positioned at an area of interest based on real-time cross-sectional OCT display, and left stationary while the pneumatic actuator performed the longitudinal scan. The data size of each pneumatically scanned acquisition was 960 samples × 4000 A-scans × 1750 frames for a 7 second acquisition over a longitudinal range of ~3.5 mm, corresponding to a total OCT scanned area of ~1.3 cm^2. For manual actuation to obtain a large field of view, the pneumatic actuator was disabled while continuing distal rotary scanning. The entire capsule was pulled back or advanced manually at a speed of ~3 mm/s via the semi-rigid tether. The data size of each manually actuated acquisition was 960 samples × 4000 A-scans × 7000 frames for a 28 second acquisition over a longitudinal range of ~80 mm, corresponding to a total OCT scanned area of ~30 cm^2.

Results and Discussion

Cross-sectional OCT

Fig. 5 shows representative OCT cross-sections of the esophagus and rectum in polar and Cartesian coordinates. Cross-sectional OCT images (B-scans) were displayed in logarithmic grayscale. Each B-scan consisted of 4000 A-scans and was acquired at 250 frames per second. The squamous epithelium (e), lamina propria (lp), muscularis mucosa (mm), submucosa (s), and muscularis propria (mp) in the esophagus were visible, and OCT imaging depth was over 1 mm (Figs. 5a and 5c). In the rectum, the OCT cross-sectional images showed the characteristic columnar structure of crypts with vertical shadowing and increased OCT signal attenuation (Figs. 5b and 5d). The outer glass surface of the capsule was approximately index matched with the tissue and generated minimal reflections. The inner glass surface (white arrow) appeared as an aliased reflection, which was detected to obtain the longitudinal trajectory for pneumatic scans, as described in Section 2.3. The features which appear as discontinuities at the tissue surface were produced by the micromotor cable (aliased, blue arrow) and inflation tube (orange arrow).

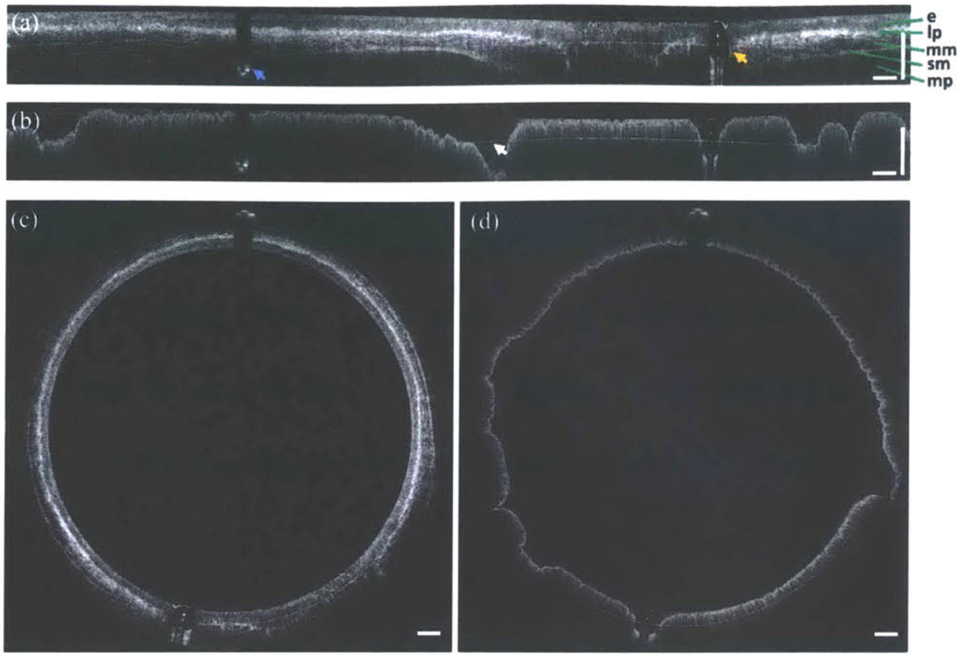

Fig. 5. Representative *in vivo* endoscopic OCT images of swine (a,c) esophagus and (b,d) rectum. Images are displayed in unwrapped (Cartesian) and circumferential (polar) views, respectively. The characteristic layered structure of the esophagus and the columnar structure of the rectum are visible. The blue and orange arrows in (a) indicate the motor cable and inflation tube, respectively. The arrow in (b) indicates the aliased inner surface of the glass tube. Scale bars are 1 mm in tissue.

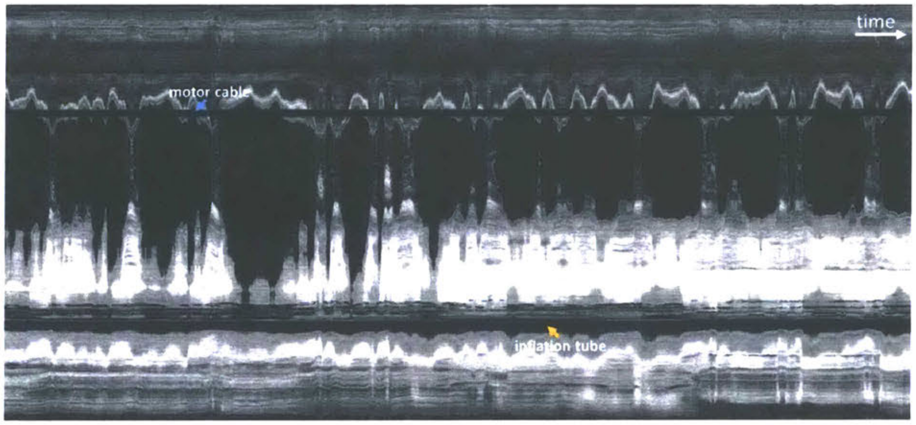

Fig. 6. *En face* OCT image from acquired volume with the fast distal rotary scan and no longitudinal actuation in order to assess motion artifacts. Large hyposcattering (dark) regions indicated areas where the esophageal wall is not in contact with the capsule. The horizontal axis

corresponds to time and spans 28 seconds. Periodic motion artifacts are consistent with cardiac and respiratory cycles.

Motion artifacts in the en face *plane*

In order to qualitatively assess the effects of cardiac motion and other possible motion artifacts, the capsule was positioned mid-esophagus and left stationary while images were acquired for 28 seconds with distal rotary scanning (no manual or pneumatic longitudinal actuation). Fig. 6 shows a representative *en face* OCT image (4000 × 7000 pixels) from about 600 μm below the esophageal surface, projected over a 100 μm depth range. The motor cable (blue arrow) and inflation tube (orange arrow) appear as horizontal shadow artifacts. Notably, the motor cable artifact appears as a straight line. The motor cable was located inside the capsule, therefore it was not subject to tissue motion or perturbations relative to the micromotor. Any instability in the distal rotary scan would manifest as oscillations in the shadow artifact, but these were not visible at this scale. Therefore, the image oscillations were not due to the distal rotary scan.

Along the time axis, there were about 40 oscillatory periods at higher frequency, and about 12 oscillations at lower frequency. The total acquisition time was 28 seconds. Therefore, the higher frequency was about 1.4 Hz, and the lower frequency was about 0.4 Hz. These frequencies correspond approximately to heart rate and respiratory rate respectively, as described in veterinary literature [97]. Both heartbeat and breathing produced significant motion in the esophagus due to its close proximity to the heart and lungs. The capsule appeared to be in continuous, periodic motion in the transverse plane. Motion in the longitudinal direction was harder to detect using the transverse scanning acquisition protocol.

En face *OCT by manual scanning*

En face images were displayed in square root of OCT signal in grayscale. Ultrahigh speed OCT enabled the visualization of *en face* structural features, even using a relatively rapid and uncontrolled manual longitudinal actuation via the tether, and with significant motion of the esophagus. Each volumetric acquisition took 28 seconds and consisted of 7,000 frames. About 5% of the start of each image was cropped due to a brief delay between the start of data acquisition and the start of manual longitudinal scanning. Assuming a longitudinal actuation speed of ~3 mm/s, the pullback length was ~8 cm and the OCT field size was ~30 cm^2.

Volumetric data was acquired by manually advancing the capsule from the proximal to distal esophagus. Fig. 7 shows *en face* OCT views of the esophageal wall at different depths and projections. The full projection (mean over 600 μm depth) image (Fig. 7(a)) produced a relatively low contrast image with some shadowing reminiscent of a vascular network (indicated by arrows), similar to an endoscopic image. Fig. 7(b) shows an *en face* OCT image at ~200 μm below the surface and projected over a 100 μm depth range, where the lower and higher hyperscattering areas correspond to the epithelium and lamina propria layers, respectively. The varying contact and resultant compression of the esophageal wall on the capsule led to tissue layers being tilted relative to the capsule surface and thus spanning a range of depths. Fig. 7(c) shows an *en face* OCT image at ~600 μm below the surface and projected over a 100 μm depth range, which shows high contrast features resembling a vascular network of large and small vessels. Dark hyposcattering areas represent regions not in contact with the esophageal wall, due to esophageal dilation or folding.

En face OCT images were also obtained from the squamo-columnar junction ('dentate line') by manually advancing the capsule from the anal verge to the rectum. Fig. 8 shows an *en face* OCT image at ~300 μm below the tissue surface and projected over a 50 μm depth range. The anal canal exhibited squamous epithelium and tissue folds, which transitioned to crypt structures in the rectum. Crypts were generally round and densely packed. Distortions from the regular crypt pattern in the longitudinal direction were due to varying speed of the manual insertion of the capsule.

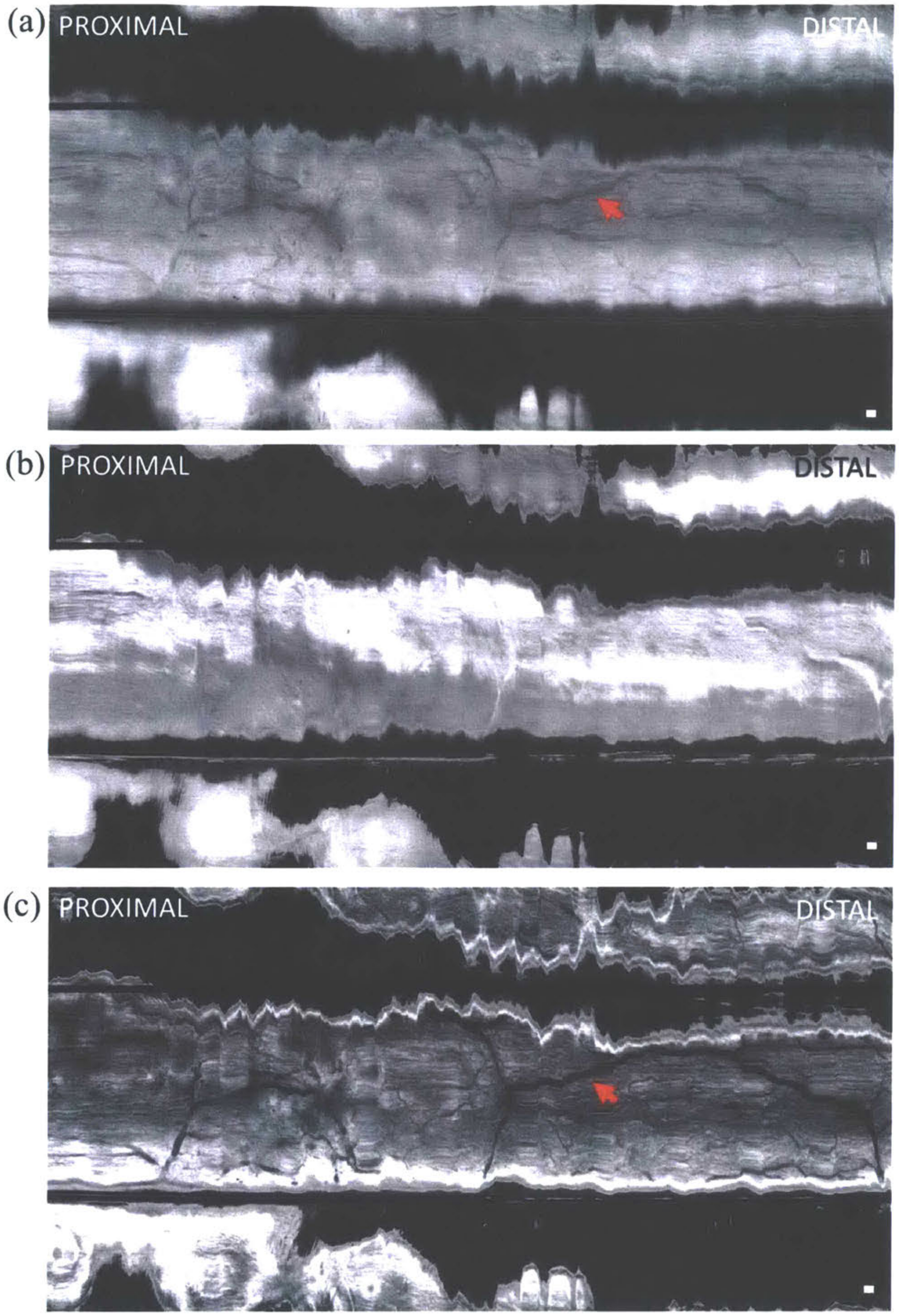

Fig. 7. *En face* OCT image of swine esophagus *in vivo* (a) projected over 600 μm depth range from the tissue surface, (b) at 200 μm below the surface and projected over 100 μm depth range, and (c) at 600 μm below the surface and projected over 100 μm depth range. The capsule was manually advanced for the longitudinal scan. Shadow patterns resembling a vascular network (red arrows)

were visible. The horizontal scale was based on an estimate of manual longitudinal pullback speed of ~3 mm/s. Scale bar is 1 mm.

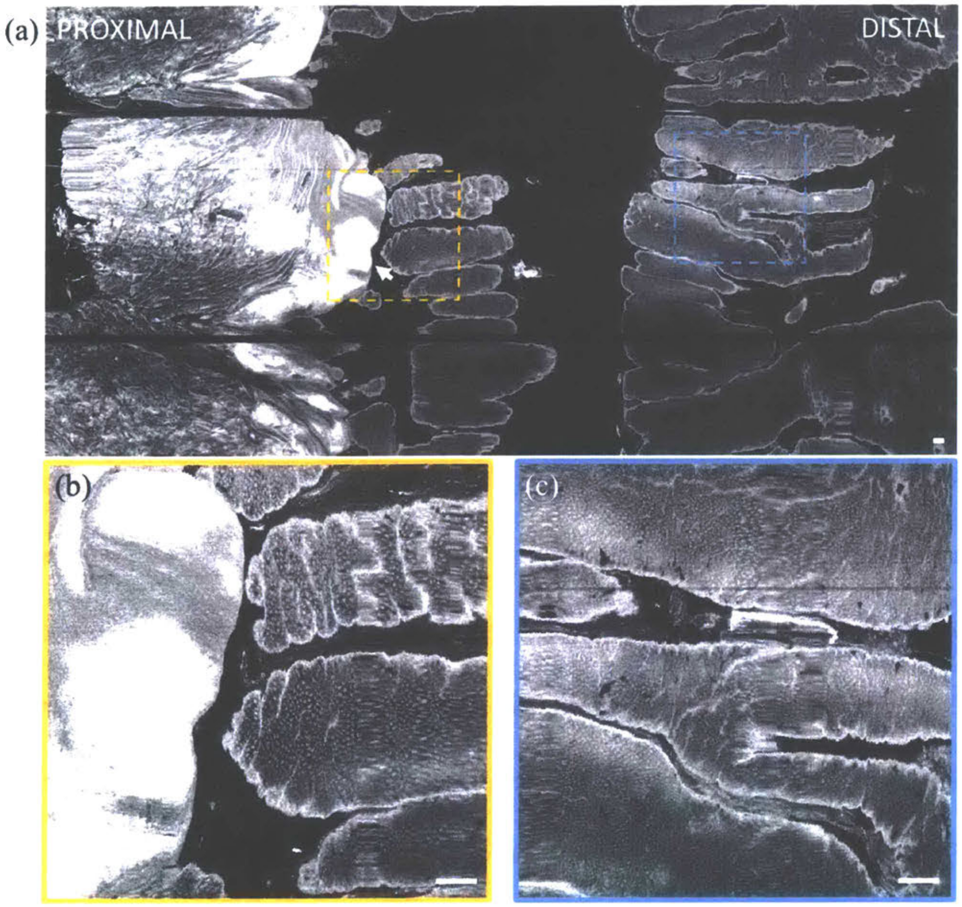

Fig. 8. (a) *En face* OCT image of swine dentate line *in vivo* at 300 μm below the tissue surface and projected over 50 μm depth range. The capsule was manually advanced for the longitudinal scan. Insets (b, c) show zoomed in regions. The transition from squamous epithelium to columnar crypts (arrow) is clearly visible. Scale bar is 1 mm.

En face *imaging by 2D distal scanning*

Volumetric OCT data was also acquired with the pneumatic actuator for longitudinal scanning in order to demonstrate precision 2D scanning over a smaller field of view. Each 3D OCT dataset consisted of 1,750 frames over a ~3.5 mm longitudinal distance, acquired in 7 seconds. The scanned area was ~1.3 cm^2. Since the squamous epithelium of the normal upper GI tract is relatively featureless in *en face* OCT, imaging was performed in the lower GI tract. Fig. 9 shows an *en face* OCT image at the dentate line in the rectum, at ~400 µm from the surface and projected over a ~50 µm depth range. The motor cable was visible as an aliased artifact. The inflation tube was in a region of tissue non-contact, such that it sagged away from the glass surface (Fig. 2) and was not visible at this particular *en face* depth. The longitudinal position of the carriage was measured using OCT, and non-uniform scanning in the longitudinal direction was corrected as described in section 2.3. Oscillation artifacts in the rotary direction are visible when the *en face* image is zoomed. These oscillations are highly regular, suggesting that they are due to non-uniform rotational distortion (NURD) of the micromotor. The deviation in rotary position was about 50 µm as measured from the image, which over a circumference of 38 mm corresponded to an angular deviation of about 8 mrad. The NURD can be corrected with methods such as a fiducial-based scan correction technique reported by our group, which can reduce NURD by over an order of magnitude [51]. This is necessary for accurate *en face* visualization, and is demonstrated in the capsule human studies reported in later chapters.

Discussion

The ability to accurately scan and image a larger circumferential region of luminal structures than previous small diameter probes is important for many endoscopic imaging applications. This study demonstrated a novel imaging capsule in living swine as a translational step towards human imaging and clinical studies. The capsule combines large field coverage (~30 cm^2) with proximal manual longitudinal actuation, and small field inspection (~1 cm^2) with precision distal pneumatic longitudinal actuation, for volumetric and *en face* imaging at microscopic resolution. These field sizes are orders of magnitude larger than existing endomicroscopy technologies such as magnification narrow band imaging with 1-2 mm^2 fields [98] and confocal laser endomicroscopy with <0.3 mm^2 fields [29]. In addition to large field of view imaging, the option to inspect a small field for fine structural anomalies could be important for real-time detection of dysplasias, which are known to be focal. The 2D distal scanning can generate undistorted *en face* features that, in future clinical studies, may resolve pit patterns which are markers of disease. The ultrahigh speed swept laser source was critical in order to image *en face* features over a large field.

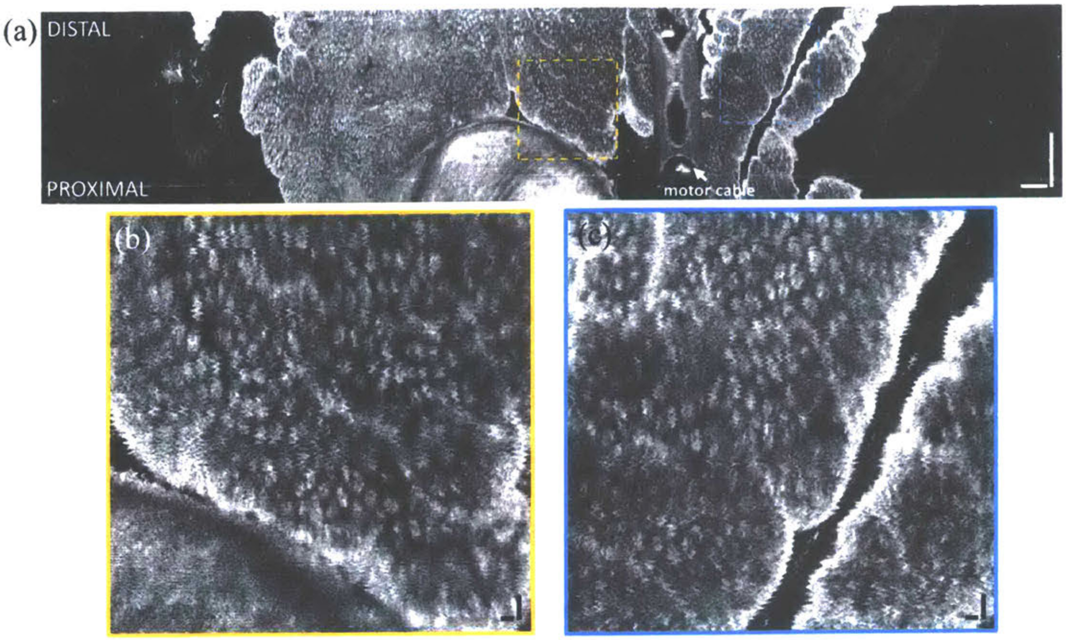

Fig. 9. (a) *En face* OCT image of swine rectum at ~400 μm depth from tissue surface and projected over ~50 μm depth range. Insets (b, c) show enlargements of regions demonstrating the high precision distal pneumatic scanning. Non-uniform rotational distortion (NURD) of the micromotor was visible. Scale bars of large image and insets are 1 mm and 100 μm, respectively. Scanned area was approximately 1.3 cm^2. The motor cable (covered by plastic extrusion on proximal end cap) appeared aliased at a different depth as indicated.

The device incorporates several technical innovations, many of which were made possible by the design flexibility of rapid prototyping. The availability and low cost of stereolithography suggests that even precision components with relatively small dimensions can be economically produced in prototype quantities or larger. Moreover, the resolution and dimensional accuracy was sufficient for parts to be used as optical mounts, making self-alignment of optical beams and bulk optics simple and accurate. The design can also be scaled to different focused spot sizes and transverse resolutions. Having the focusing optics perpendicular to the tissue surface, rather than reflecting 90 degrees as in previous generation proximally scanned catheters, allows higher numerical aperture focusing. The ability of the capsule to scale to high numerical aperture, combined with precision distal longitudinal scanning should enable these devices to be used for optical coherence microscopy (OCM) [99, 100] or other scanning microscopy techniques. The primary challenge in designing the precision distal longitudinal scanning optical system was the requirement that the translating carriage had to remain aligned to the collimated beam over the full longitudinal travel. Careful adjustment of the carriage contacts to ensure optimized centration and alignment in the glass tube was important. The uniformity and optical clarity of glass tubing was advantageous; however, future clinical devices would use medical grade plastics.

The requirement of precise but slow scanning in the longitudinal direction is extremely challenging, because it is difficult to achieve precision at slow speeds. The pneumatic longitudinal actuator is a novel method for performing precise distal longitudinal scanning. It is cylindrically symmetric, simple, extremely compact when deflated, and capable of actuating at different speeds dependent on the proximal inflation. Using a bellows with optimized material and structural design, together with a shorter motor would further improve the longitudinal scan length. Expanding the bellows within the sealed capsule required a relatively high pressure. Also, the compressibility of air resulted in inefficient and nonlinear actuation. Use of hydraulic actuation with an incompressible fluid would enable more accurate and rapid longitudinal translation, even with a hermetically sealed capsule. An incompressible fluid should also reduce parasitic oscillatory motion of the carriage due to motor vibrations. Finally, it should also be noted that the inflation tube was located outside the capsule due to space constraints, but a custom designed plastic enclosure could have the inflation tube fabricated inside the capsule or within the capsule wall.

While the speed may be marginally improved with better designs in the future, multi-volume/sec rates are likely too difficult to achieve, and the nonlinearity of the pneumatic trajectory may be a persistent limitation of this type of scan.

The ability to distally actuate longitudinally while simultaneously measuring the longitudinal position for post-acquisition volumetric data correction is important not only for applications such as *en face* OCT and OCTA, but also promises to enable high precision scanning microscopy modalities such as confocal fluorescence or multiphoton microscopy. Our group previously reported a fiducial based scan correction method for the fast rotary scan [51]. The present study demonstrated feasibility of correcting the slow longitudinal scan by measuring its trajectory using OCT. Translation of the mirror in the reference arm to vary the path length was required to maintain the OCT image within the limited imaging range. The long coherence length of the VCSEL light source supports long-range imaging with minimal sensitivity roll-off [101] and higher speed data acquisition cards of up to 4 GS/s are now commercially available, suggesting that imaging range could be increased in the future. Endoscopic OCTA using a small ~3 mm diameter micromotor probe compatible with the working channel of the endoscope [52] has been previously demonstrated, but the field of view is limited. Extending to wider fields of view provided by the capsule is challenging because OCTA requires precise and repeatable scanning in two dimensions in order to calculate scan-to-scan phase or intensity decorrelation. This is an important topic of continuing research and development.

The feasibility of the manual longitudinal actuation for generating *en face* images depends largely on the imaging speed of the OCT system. It is difficult to manually actuate a semi-rigid tether at a constant speed slower than a few millimeters per second, which would be required to achieve Nyquist sampling at limited axial scan rates. Anatomic variations and resultant tensional changes in the tether during the scan further exacerbate the difficulty in scanning smoothly. Length calibrated actuation using motorized translation stages, position sensors [102] or image-based tracking [103] would help to localize the capsule and/or control its speed. The availability of even higher speed swept source systems would relax the requirement for slow manual actuation, and even enable increased manual longitudinal scan speeds for more rapid volumetric data acquisition over large fields of view. Higher speeds are also important for functional OCTA imaging. Swept sources with multi-megahertz A-scan rates [70] would enable longitudinal actuation speeds of up to 1 cm/s, which is moderately fast and should be easier to perform than slower speeds.

In the upper GI tract, the capsule can cover virtually the entire length of the esophagus by proximal manual actuation. Dense optical sampling and *en face* imaging would enable mapping of the unwrapped esophageal surface to identify focal pathology. However, the generation of complete and unobscured *en face* views depends on contact of the full esophageal circumference with the capsule surface during the proximal actuation. Achieving uniform tissue contact was challenging in the sedated swine; in the esophagus, full circumferential contact occurred only occasionally, and *en face* OCT images often showed large areas of non-contact. Previous OCT capsule imaging studies in humans reported good contact, with 94% of acquired frames having more than 50% coverage when the capsule was swallowed by non-sedated, sitting patients [94]. This is likely due to the peristalsis produced when the patient swallows the capsule, causing the esophageal wall to contract around the capsule, while the peristaltic wave propels it downward. The muscular tone of the lower esophageal sphincter may also have a role in imaging of conscious patients. These issues are discussed further in later chapters. In a sedated animal model, peristalsis could not be induced, which may have resulted in highly variable tissue contact, exacerbated by the effects of cardiac motion. It is likely that swallow-induced peristalsis in either conscious or moderately sedated human patients will improve tissue-capsule contact.

The capsule could be clinically applicable to not only upper GI screening in unsedated patients, but also as an adjunct to the endoscope during standard upper GI endoscopy. Previous imaging studies in unsedated patients used a highly flexible tether to optimize patient comfort [92, 93]. For imaging during standard endoscopy, the tether should be semi-rigid, allowing arbitrary longitudinal positioning and actuation regardless of esophageal motility or gravitational force. In the swine study, the semi-rigid tether enabled large field of view imaging by pulling back or advancing the capsule, as well as small field of view imaging using precision distal pneumatic scanning while maintaining the capsule's orientation and longitudinal position. Although swallowing could not be induced in the swine and thus an overtube was required to introduce the capsule, a moderately sedated patient is able to swallow to open the upper esophageal sphincter for introduction of the capsule, as is done for an endoscope. After introduction of the capsule, the small-diameter tether remaining in the patient's mouth and throat should be well tolerated and more comfortable than a larger diameter endoscope. We have performed preliminary clinical studies in patients which suggest that the capsule can be introduced independently into the esophagus prior to introduction of the endoscope and obtain good tissue contact and *en face* imaging. It should be noted that the tether flexibility can be changed, independent of the distal device design, enabling variations of this device to be used for multiple endoscopic and possible intraoperative imaging applications such as surgical cavities. The semi-rigid tether might also be used in a non-sedation setting; there are ultrathin (<6 mm diameter) endoscopes and capsule catheters used transorally without sedation [104, 105] that have semi-rigid tethers. The ability to perform capsule OCT imaging as an adjunct to endoscopy suggests applications for surveillance as well as targeting of specific areas for ablative therapies based on real-time image guidance.

In the lower GI tract, the ability to position the imaging device is particularly critical since peristalsis cannot be used as in the upper GI tract. In the swine study, there was minimal motion in the lower GI tract, enabling high resolution *en face* visualization of surface pit patterns, although circumferential contact was variable and dependent on lumen size. Tissue contact was good in the anal canal and slightly worse in the rectum. Suboptimal tissue contact may be related to residual fluid from prior enema administration leading to lumen dilation; suction via a separate catheter may improve contact. The ease of introduction into the rectum suggests that the capsule could be used for non-endoscopic evaluation and other clinical studies of anal and rectal cancers, inflammation, and vascular pathologies [106]. For imaging further up in the transverse and ascending colon, the capsule could be carried on the distal end of the endoscope with a band or mount. The capsule would not be able to image the full luminal circumference of the colon, but when placed in contact with a region of interest would image a much larger angular field than a small diameter probe. Distal pneumatic longitudinal actuation is particularly well suited for this application; once the capsule is positioned in contact with a region of interest, the distal scan can cover a field of view that is larger than magnification endoscopy or confocal laser endomicroscopy.

Clinical *en face* OCT imaging can enable volumetric visualization of pit patterns that have been used as diagnostic markers with conventional endoscopic imaging in both the upper and lower GI tract. The swine study results suggest that depth resolved imaging could generate large field *en face* views of tissue morphology and vasculature with higher contrast than standard endoscopy. Recent studies with endoscopic narrow band imaging use image evaluation criteria based on surface and vascular pattern morphologies and have only moderate sensitivity and specificity [107]. OCT will enable high contrast subsurface *en face* visualization as well as cross-sectional imaging, providing more comprehensive structural information [44]. This could improve detection of not only BE in a screening setting, but also might enable detection of dysplasia in a surveillance setting without requiring conventional sedation endoscopy.

Future versions of the capsule could integrate endoscopic capabilities such as marking [47, 48], ablation, and biopsy that would be guided by real-time imaging. Circumferential ablation catheters [108] and biopsy capsules [109] are known in endoscopic practice, and could be significantly improved with real-time image guidance. Laser marking of sites for biopsy using an imaging capsule has also been demonstrated [72, 110]. However, the difficulty of delivering focal therapies using a capsule (unlike an inflated balloon, which is more stable but produces lower image quality) given motion between the capsule and the esophageal wall, is a challenging problem. Nevertheless, the modularity of the capsule design suggests that multiple medical technologies could be incorporated, such that a toolbox of multiple imaging / treatment capsules, each with different specialized capabilities could be a powerful addition to the endoscopy clinic.

4. Conclusion

In this study, capsule OCT was demonstrated at 1 MHz A-scan rate and 250 frames per second. The ultrahigh speed volumetric imaging was able to generate *en face* OCT over large fields. The capsule had two independent and orthogonal distal scanning mechanisms, a micromotor rotary scanner and a pneumatic longitudinal actuator, which produced accurate 2D beam scanning. The pneumatic actuator was shown to enable compact and robust optical scanning, and also longitudinal position measurement and correction. Images were acquired in the living swine esophagus and rectum, with proximal manual actuation and distal pneumatic actuation. *En face* and depth resolved visualization of surface features was demonstrated over large fields. This work was a translational study as a step toward performing clinical imaging studies in patients.

Capsule OCT with *en face* imaging may have significant clinical impact, particularly in the volumetric visualization of *en face* pit patterns in both the upper and lower GI tract. The device would be able to comprehensively image large fields of view for mapping of surface features by proximal manual actuation, and perform distal scanning for high resolution, small field of view, volumetric OCT imaging or scanning microscopy. Future work will investigate imaging in human patients with upper and lower GI pathologies.

Chapter 4

Tethered capsule *en face* OCT of Barrett's Esophagus and dysplasia: initial results in sedated patients

Introduction

Dysplasia in Barrett's Esophagus (BE) is patchy [13] and sometimes missed by random biopsies. Optical coherence tomography (OCT) can image large areas of the esophagus, however slow imaging speeds in earlier studies limited visualization to cross-sections. Cross-sectional OCT detected high-grade dysplasia with sensitivity/specificity ~80% [42, 111]. Tethered OCT capsules were demonstrated for cross-sectional imaging in unsedated screening to detect BE [92, 112]. Our group recently developed ultrahigh-speed OCT for *en face* and angiographic imaging using micromotor probes in patients [51, 52] and large field-of-view tethered capsule devices in swine [55]. Narrow-band imaging (NBI) visualizes surface mucosal patterns to detect dysplasia, but multi-center trials reported suboptimal dysplasia detection [113]. In this report, we demonstrate an ultrahigh-speed OCT tethered capsule enabling large field-of-view, subsurface *en face* and cross-sectional volumetric imaging of BE and dysplasia. Subsurface *en face* OCT provides complementary information to cross-sectional OCT and NBI.

Materials and Methods

This work was performed in collaboration with the VA Boston Healthcare System (Dr. Hiroshi Mashimo MD PhD and staff at the Endoscopy Unit), Thorlabs (Dr. Benjamin Potsaid) and Praevium Research (Dr. Vijaysekhar Jayaraman) for use of prototype swept source technology.

The OCT prototype instrument was 20x faster than commercial OCT instruments [42]. Imaging was performed using ~30mm long x 12mm diameter tethered capsules (Fig. 2C), with micromotor scanning at 300 frames/second. The semi-rigid tether enabled capsule introduction into the esophagus of sedated patients prior to introducing the endoscope for examination and biopsy/resection. The tether could be pulled/pushed to volumetrically map the esophagus. The capsule used a single micromotor scanner for rotary scanning, and did not use 2-D distal actuation as described in the previous chapter, for simplicity. An earlier capsule design investigated the use of proximal actuation for pullback of an internal optical carriage similar to the pneumatic design, but the range was too small and pullback was highly nonuniform due to friction.

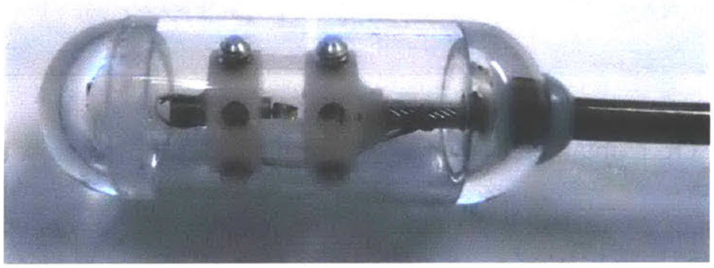

Fig. 1. An earlier design for clinical capsule imaging that used a proximal pullback for translation of an internal carriage for longitudinal scanning. This was found to be impractical and later discontinued in favor of manual pullback scanning.

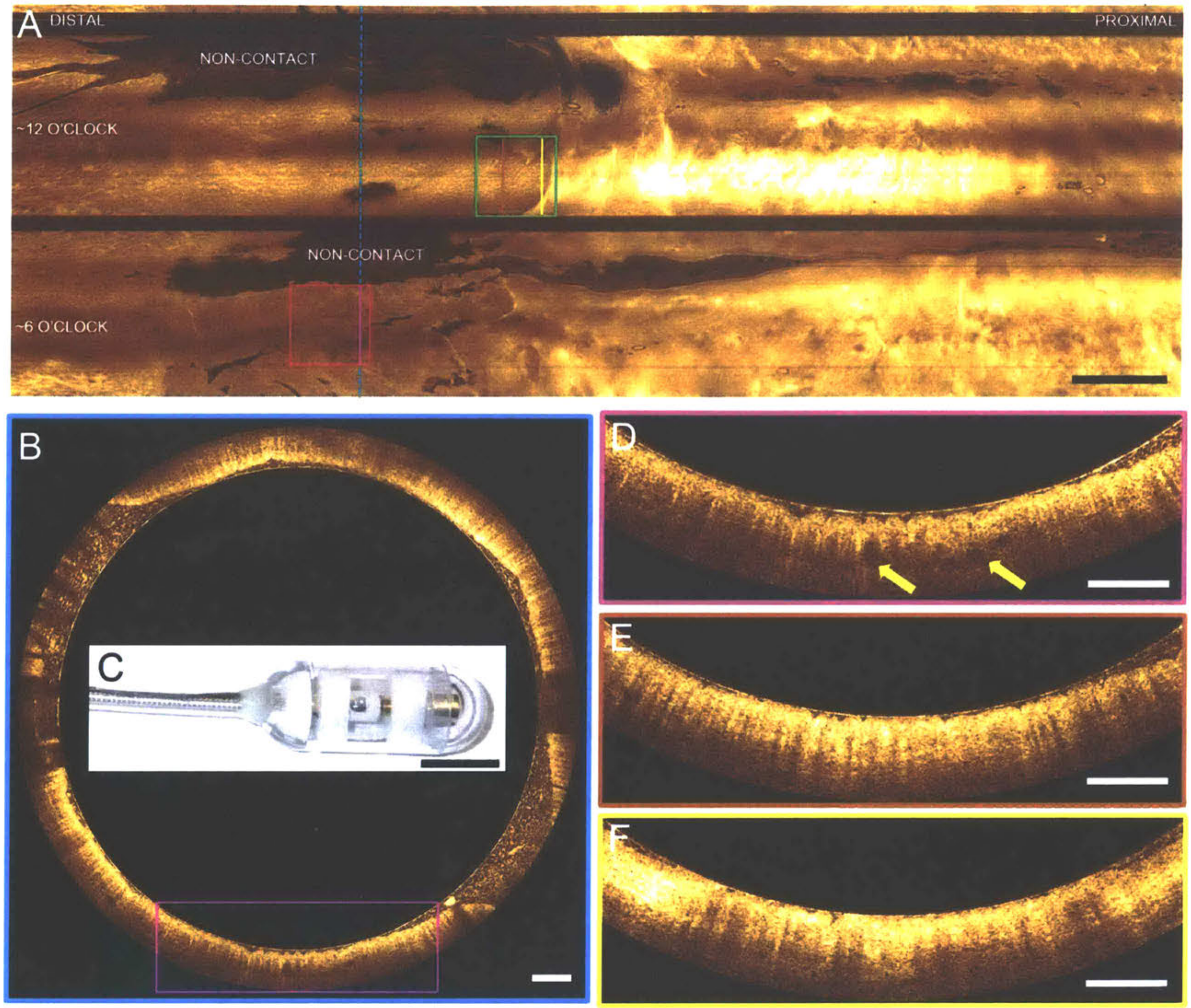

Fig. 2. (A) *En face* OCT obtained by averaging from ~200-280μm below esophageal surface. Only the distal 12cm out of 24cm data is shown. Dark regions are due to non-contact of the capsule with the esophagus. Scale bar 1cm. (B) Representative cross-section (blue) from EMR region (red). Scale bar 1mm. (C) Photograph of capsule used for imaging. Scale bar 1cm. (D) Enlargement (pink) from (B) showing layer effacement, surface signal greater than subsurface, and multiple dilated glands (arrows). (E) Cross-section (brown) showing layered BE which is likely non-

dysplastic. (F) Cross-section (yellow) showing the squamo-columnar junction at a tongue of BE. Inset scale bars 1mm.

Results and Discussion

Eighteen patients were imaged with different resolutions and pull/push speeds to optimize the imaging protocol; 3 were imaged with the optimum protocol presented here. The initial 7 patients were imaged at 600 kHz axial scan rate, and had the capsules introduced after endoscope introduction, which seemed to dilate the esophagus and produced little or no contact on the capsule, similar to the earlier swine studies. For the remaining patients, imaging was sped up to 1 MHz axial scan rate to try and improve image sampling and scan speeds. 4 patients were imaged at ~0.25 cm/sec pullback speeds (5 cm in 20 sec) to achieve oversampling for OCTA (see later bonus supplement), but longitudinal image artifacts were excessive. The next 4 patients were imaged at ~0.5 cm/sec, and thereafter 3 patients had imaging pullbacks at ~1cm/sec, which was below the Nyquist oversampling requirement but was attempted in order to overcome potential frictional effects and eventually yielded optimal data.

One patient, a 68 y.o. male with dysplasia history and treatment-naïve C4M5 segment is presented; the other two patients had non-dysplastic BE. After sedation, the capsule was advanced to the gastro-esophageal junction (GEJ) under OCT guidance. The capsule was pulled back ~24cm in ~20 seconds to acquire an OCT volume, advanced to acquire a second volume, then withdrawn. The endoscope was then introduced for standard examination.

A slightly raised lesion at 6 o'clock, ~1cm distal to the squamo-columnar junction (SCJ) appeared irregular on NBI and was removed with endoscopic mucosal resection (EMR). Histopathology showed extensive low-grade dysplasia. The EMR region was registered using OCT capsule fiducials and endoscopic landmarks such as the SCJ. In the EMR region, cross-sectional OCT showed atypical glandular architecture, dilated glands, layer effacement, and surface signal intensity higher than subsurface (Fig. 2D), OCT features associated with dysplasia [42]. Subsurface *en face* OCT at 200μm and 400μm depths exhibited irregular mucosal patterns and dilated glands respectively (Figs. 3A-B), features associated with dysplasia on NBI [113] and OCT. Near the SCJ, cross-sectional OCT showed layered BE (Figs. 2E-F), while *en face* OCT at 200μm depth (Fig. 3C) exhibited regular circular and ridged/villous mucosal patterns, features of non-dysplastic BE.

The registered cross-sectional and *en face* views facilitated interpretation of OCT data. The near-vertical columnar epithelium of crypts was associated with high optical scattering and transmission, producing bright vertical features in OCT cross-sections, which were projected to deeper depths in *en face* OCT. Conversely the crypt lumen and lamina propria between crypts were associated with low optical scattering, producing dark vertical features in cross-sections and *en face* OCT. These effects imply that *en face* OCT visualizes the integrated effect of light transmission and backscattering. Disruption of vertical crypt architecture by dysplasia increased OCT signal at shallow depths and attenuated signals at deeper depths in both cross-sectional and *en face* OCT.

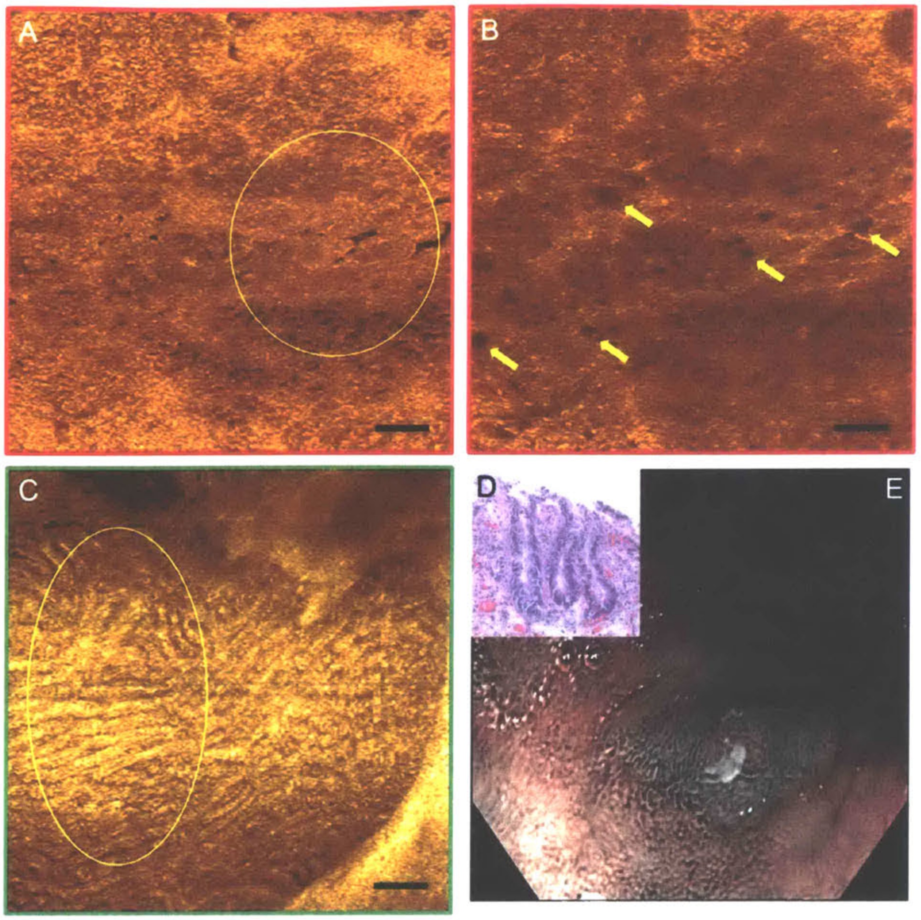

Fig. 3. (A) *En face* OCT (red) enlarged from Fig. 1(A) (averaged from ~200-280μm depth) showing the region from which EMR was taken, with irregular mucosal patterns (circled). (B) Deeper *en face* OCT from same region as (A) (averaged from ~400-480μm depth) showing dilated glands (arrows). (C) *En face* OCT (green) from Fig. 1(A) (~200-280μm depth) showing regular circular and ridged/villous mucosal patterns (circled), likely non-dysplastic BE. Inset scale bars 1 mm. (D) EMR histopathology showing LGD. (E) Endoscopic NBI image of EMR region.

The study was limited because the full esophageal circumference was not imaged; non-contact regions appeared dark in the *en face* images. Non-uniform longitudinal capsule actuation from manual pull/push, respiratory/cardiac motion, or peristalsis produced *en face* image distortion. Motion artifacts were ameliorated by the ultrafast imaging speed and ~1cm/s longitudinal pull/push (~300 frames/cm) which yielded smoother motion than slower pull/push speeds. OCT reading was not blinded to histopathology. The EMR was smaller than OCT field-of-view, therefore many OCT regions were histologically unverified.

Introducing the capsule with a semi-rigid tether prior to endoscopy was well tolerated with no adverse events and enabled endoscopic/histology correlation with OCT findings. The semi-rigid tether preserved capsule orientation enabling registration to endoscopic views. These capabilities will facilitate larger studies correlating OCT with histology. Imaging can also be performed with a soft tether in non-sedation screening/surveillance.

En face OCT capsule imaging enables rapid mapping of the esophagus. *En face* features at shallow depths corresponded with known NBI features, while subsurface *en face* views visualized gland morphology. Cross-sectional and *en face* views were intrinsically co-registered and showed features of BE and dysplasia. *En face* capsule OCT provides information which is complementary to cross-sectional OCT and NBI, and promises to improve sensitivity/specificity for detecting dysplasia.

Bonus supplement: OCT angiography

This section presents unpublished work that attempted to obtain OCT angiography (OCTA) using tethered capsules. By rescanning over vascular areas and comparing sequential OCT frames, motion contrast from moving blood can be obtained. Vascular changes and angiogenesis are associated with cancer progression and are a known marker of BE pathology. To date the only demonstrations of OCT angiography with endoscopic instruments has used high speed micromotor scanning in a small 3mm diameter probe and a proximal pullback. A slow pullback of 2 mm/sec enables the rapid micromotor frames to be sequentially compared. It was of interest to explore the possibility of dramatically increasing the field of view of endoscopic OCTA by using tethered capsules in a similar pullback scheme but with simple manual control.

Using the micromotor probe, the fast axis is 2x Nyquist (4x oversampled) and the slow axis is 3x oversampled. With typical capsule parameters (30 um FWHM transverse resolution, 300 Hz frame rate, 1 cm/sec pullback), the fast axis is 1x Nyquist and the pullback is 0.5x Nyquist. These parameters were adjusted for oversampling. The capsule resolution (Fig. 4) was adjusted to 40 um, similar to a VLE balloon. The worsened resolution will make oversampling easier, but does reduce OCT signal and sensitivity due to the lower numerical aperture.

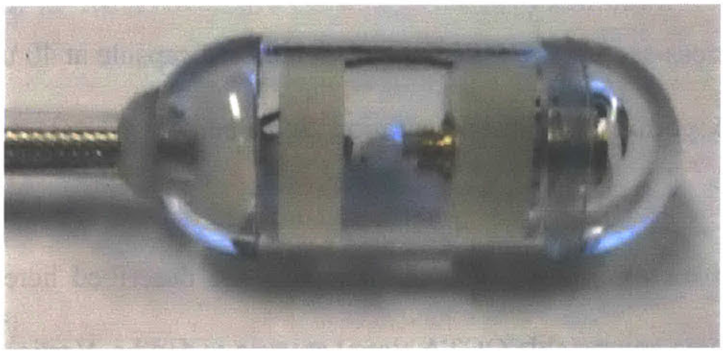

Fig. 4. Capsule design for low numerical aperture imaging. Motor rotates a prism only (no lens carriage) and the working distance of the focusing optics is long.

The imaging speed was 1 MHz A-scan rate, and the motor was scanned at 250 Hz frame rate, giving ~2x Nyquist sampling in the rotary direction. The manual scan speed was determined to be ~0.25 cm/sec (5 cm in 20 seconds), which was ~2x Nyquist in the pullback direction. Imaging was performed during sedation endoscopy, by the endoscopist performing pullback and push-forward scans via the tether. In post-processing, fiducial based non-rigid registration of OCT frames was performed to reduce nonuniform rotational artifacts and improve spot overlap. OCTA contrast was obtained by standard OCT amplitude decorrelation computations of adjacent OCT frames.

Fig. 5 shows an example cross-sectional image over squamous mucosa. Despite good tissue contact, the OCT signal was relatively low, and likely attributable to the large spot size (low numerical aperture signal collection).

Fig. 5. Example cross-sectional OCT image from tethered capsule at 40 um transverse resolution. OCT signal is suboptimal with poor penetration. Scale bar 1 mm.

Two BE patients imaged with this protocol are described here. Imaging in squamous mucosa yielded some appreciable OCTA signal at various depths. Vertical bands of noise artifacts likely corresponded to respiratory motion artifacts (about 6 periods in 20 sec = 0.3 Hz). Fig. 6-7 show OCTA from 200 um and 400 um depth respectively. The superficial layer shows pillar-like structures extending down into deeper depths, likely drainage vessels originating from intrapapillary capillary loops in the epithelium[114] that are likely too small or have too slow flows to be resolved with endoscopic OCTA.

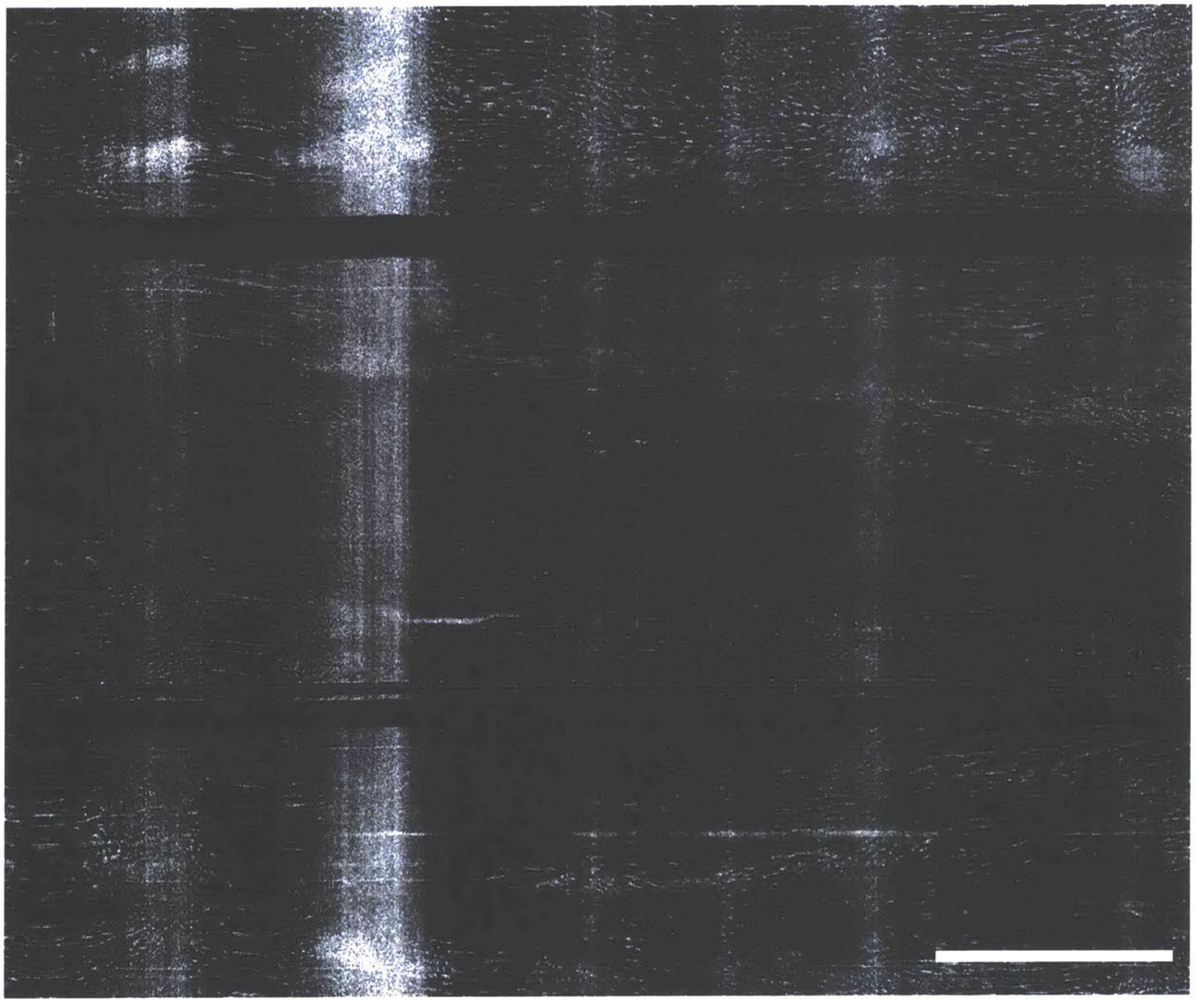

Fig. 6. OCTA of normal squamous mucosa at 200 um below surface. Image is 4 cm x 5 cm. Dots/streaks likely transverse sections of pillar-like vertical drainage vessels. Scale bar 1 cm.

The deeper layer closer to the lamina propria at 400 um depth (Fig. 7) shows a high density of complex vasculature, some of which with larger calibers. The features appear much smaller than typical vessel shadowing from OCT signal, which mainly picks up only the largest vessels.

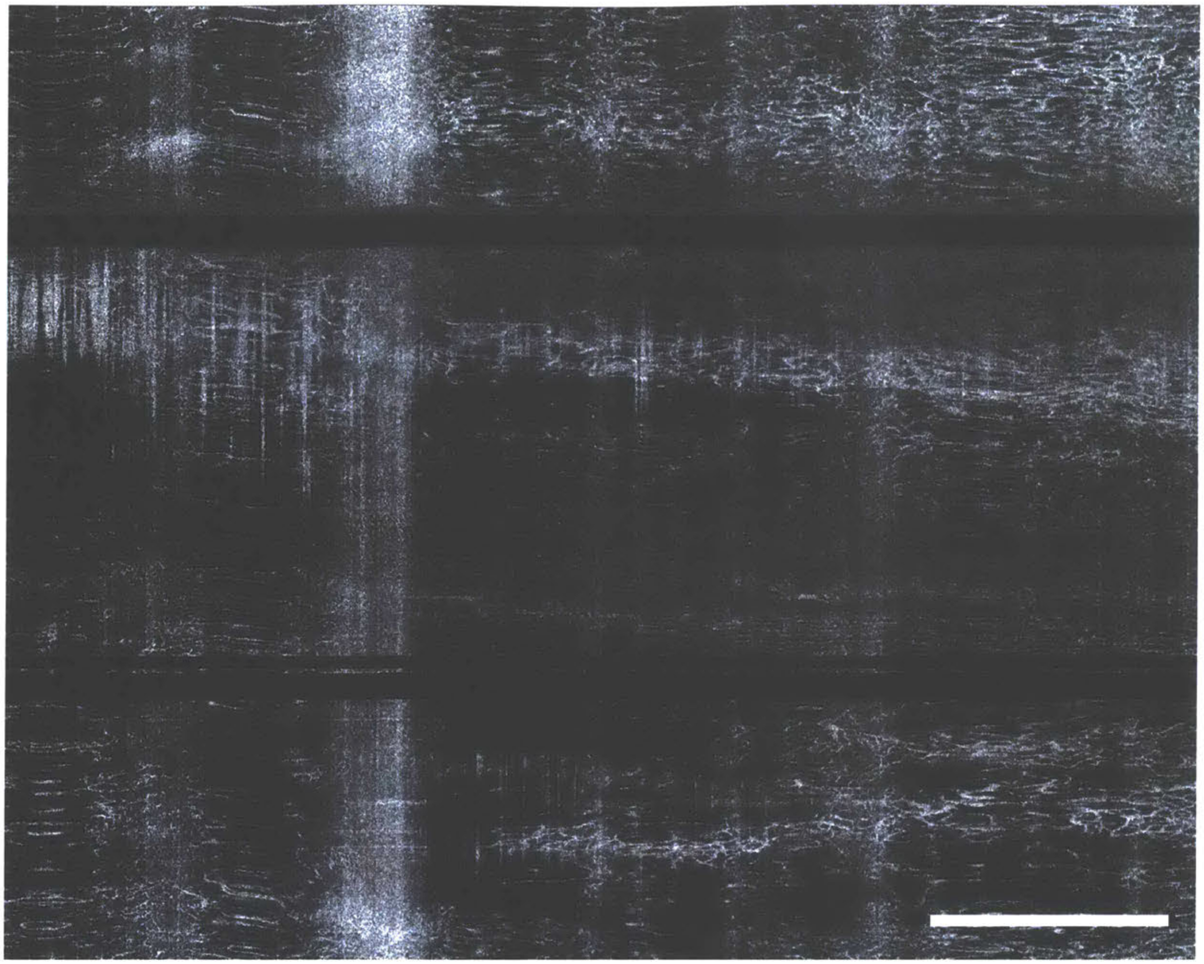

Fig. 7. OCTA of normal squamous mucosa at 400 um below surface. High density of complex vascular networks can be observed.

Fig. 8 shows an example of imaging in BE. At the superficial 200 um depth, the normal squamous region showed only minimal vascular contrast, but the BE region showed distinctive honeycomb network associated with the columnar epithelium. The high frequency vertical noise bands (1.3 Hz) are likely from cardiac motion. There is substantial longitudinal stretching from nonuniform translation, likely due to friction occurring at slow pullback speed. In Chapter 6, an optimized material for the capsule that appears to reduce frictional effects is discussed.

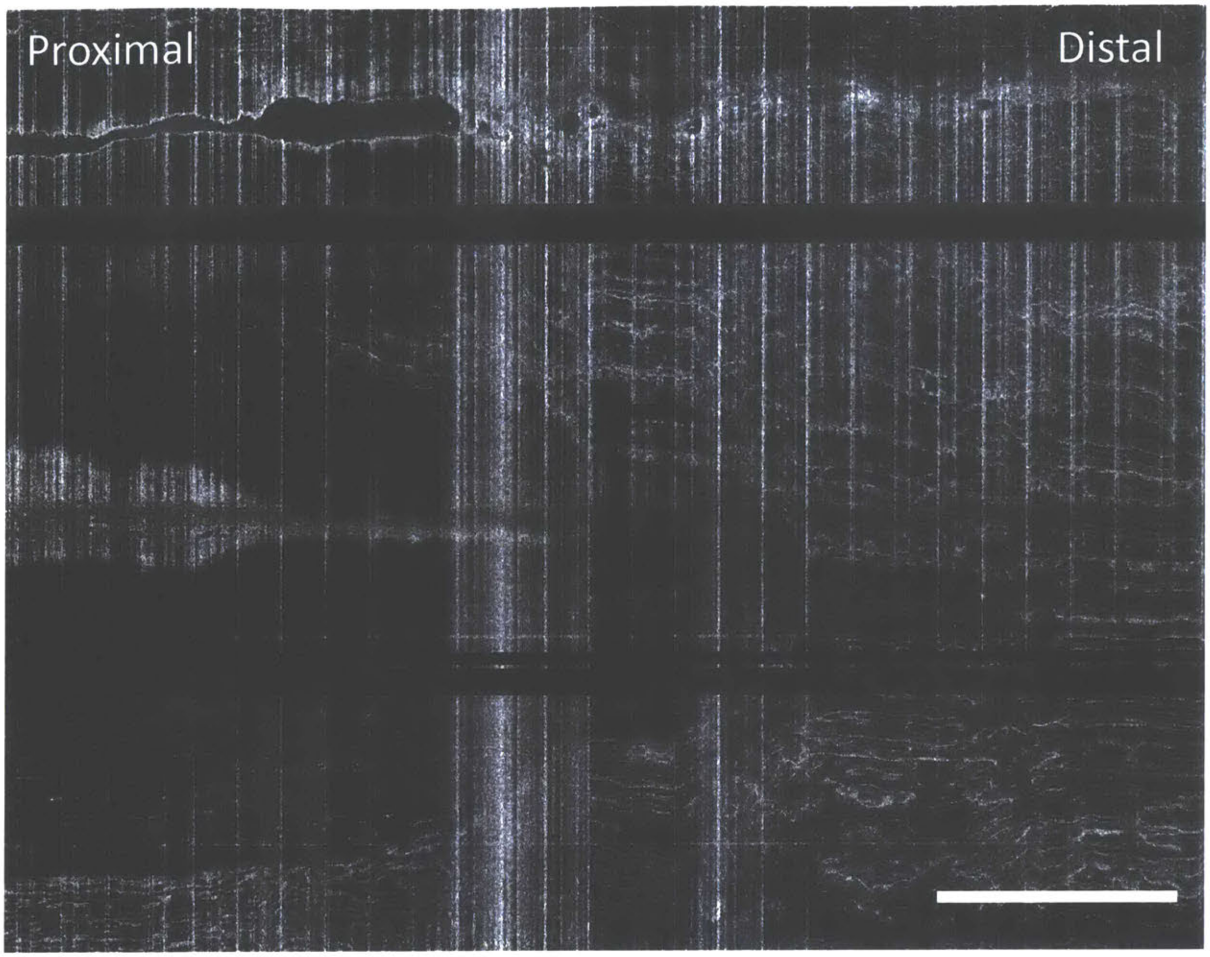

Fig. 8. OCTA from patient with BE. Despite high noise, the SCJ can be discerned based on superficial vasculature from BE vs squamous epithelium.

It will be of great interest to continue these efforts to improve the quality of capsule OCTA in the esophagus. The transverse resolution of 40 um appears to generate sufficiently oversampling but the OCT image quality may be unacceptably poor. Also, a slow manual scan of 0.25cm/sec is infeasible and likely to generate longitudinal distortions from frictional effects, therefore higher axial scan rates and frame rates are needed to correspondingly scale up manual scan speed. If accepting poor OCT image quality as a tradeoff for OCTA, using 2x faster OCT imaging speed at 2 MHz and 2x faster frame rate at 500-600 Hz would preserve sampling and enable 2x faster manual scanning at 0.5cm/sec. If using 30 um resolution (standard capsule specification) to preserve OCT image quality, and assuming a 4 cm capsule circumference, there are 5400 A-scans required per frame for 2x Nyquist transverse sampling. Assuming 600 Hz frame rate is technically feasible, this requires ~3 MHz axial scan rate and ~0.5cm/sec manual scan for 2x Nyquist longitudinal sampling. These proposed 2-3x increases in axial scan rates will need to be matched by corresponding gains in A/D sampling rates and/or linearized laser sweeps to preserve imaging range. Substantial system upgrades will be needed, but the rewards are likely worth it.

Chapter 5

Cycloid scanning for wide field side viewing endomicroscopy

Introduction

Optical imaging catheter devices have had a longstanding clinical impact in the endoscopic imaging of luminal organs such as the gastrointestinal (GI) tract, particularly with optical coherence tomography (OCT)[39, 40, 50] and confocal microscopy[29, 30]. Side-viewing optical probes, such as for 3-dimensional (3-D) OCT imaging, were traditionally scanned with rotary and pull-back mechanisms at the proximal end[36, 37]. Proximal scan actuation was known to result in non-uniform rotational distortion (NURD) and longitudinal distortion[41, 115, 116]. Early studies proposed the use of a micromotor to perform rotary scanning at the distal end[74, 75], which was recently revisited by multiple groups[52, 76-78, 117]. However, these studies still relied on a proximal motorized actuation for the slow pullback scan, and the micromotor still exhibited NURD[51]. 2-D scanning with purely distal mechanisms has been largely limited to forward viewing probes, using microelectromechanical systems (MEMS)[118] or piezoelectric actuators[60, 64, 82, 83]. The piezoelectric tubular actuator producing a 2-D spiral forward scan has been demonstrated with multi-spectral imaging[119], OCT[59, 62], and nonlinear fluorescence[120-122]. However, the spiral scan inefficiently samples towards the center, results in non-uniform optical exposure, and is known to require frequent trajectory calibration due to amplitude-dependent phase variation of the fiber scanner[60, 120]. Lissajous scanning has been proposed[123-125], which also has non-uniform sampling and requires careful control of frequency and cross-coupling between scan axes. Forward viewing piezoelectric probes for OCT and other scanning microscopies have been typically limited to small fields[59] of <3 mm^2.

Tethered capsules as optical probes have been studied for interrogation of the GI wall[88] where more precise spatial control is possible compared to the well-known wireless version[86], and the potential for capsule imaging without sedation has applications in disease screening. A tethered capsule using a piezoelectric fiber scanner delivering white-light forward imaging was reported previously[90]. This was followed by an OCT variant[92] and another variant with spectrally encoded confocal microscopy (SECM)[93] for side viewing of the esophageal circumference. Our group developed a micromotor tethered capsule using proximal manual pullback for volumetric and *en face* esophageal OCT imaging of up to 100 cm^2 field-of-view (FOV) in patients, but the manual pullback could not generate rapid volumetric rates[54]. Recently, we demonstrated one of the first distal 2-D scanning, circumferential side viewing scanners incorporated into a tethered capsule, using a micromotor for the rotary (circumferential) scan and a pneumatic scanner for the longitudinal scan[55]. This study suggested the potential for catheter-based 2-D scanning side-viewing microscopy *in vivo*, but the pneumatic scanner was bulky and difficult to drive rapidly, limiting volumetric rates.

In addition to OCT imaging of microstructure, OCT angiography (OCTA) has also been previously reported for imaging of vasculature without contrast agents[56, 66, 126-128]. Early endoscopic studies used Doppler OCT to visualize relatively large vessels[38, 129]. Recently, our group demonstrated ultrahigh speed endoscopic OCTA for visualizing 3-D microvasculature in the GI tract, using a small diameter micromotor probe[52], a balloon for larger FOV[57], and a piezoelectric scanning probe for forward imaging[130]. The use of distal scanners with high scan stability is critical for endoscopic OCTA.

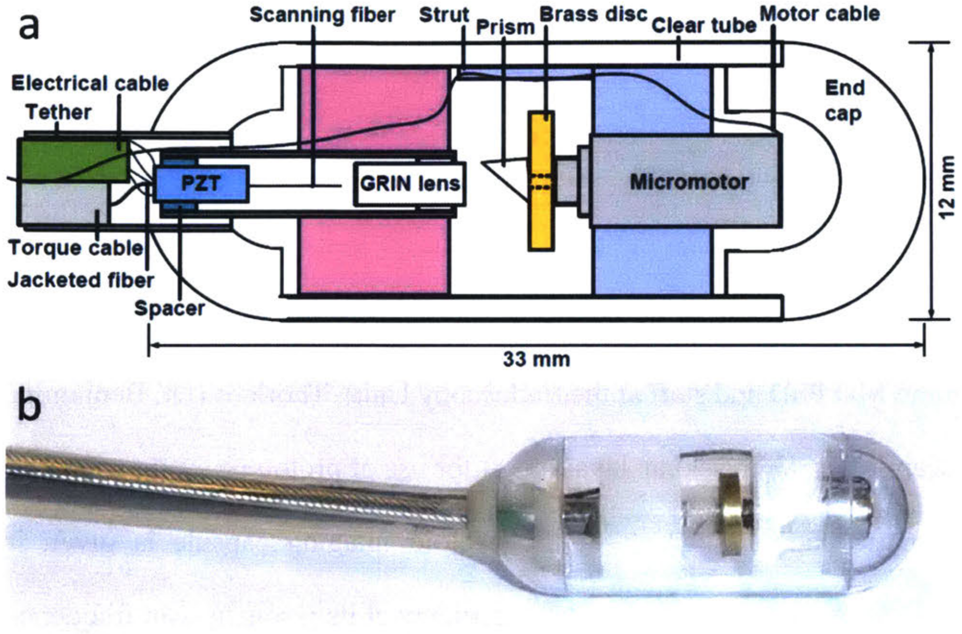

Fig. 1. (a) Schematic and (b) photograph of cycloid scanning capsule for distal 2-D scanning in luminal organs such as the GI tract.

In this study, we report a new distal 2-D precision scanning technology that can achieve rapid volumetric side view imaging with a large FOV using a capsule device. A piezoelectric tube is used to perform a precision fast scan of an optical fiber, and the scanned beam is reflected to the radial direction and rotary scanned around the circumference, generating a cycloid scan trajectory which covers a large circumferential strip. Sequential strip volumes can be acquired using proximal pullback (or push forward) to image centimeter-long regions. We demonstrate 1.17 MHz A-scan rate ultrahigh speed swept source OCT with an imaging area of 1 mm x 38 mm and volume rate of 3 volumes/sec, and OCTA at 0.5 volumes/sec in the human rectum. The combination of the resonant fiber scanner and micromotor, which are some of the fastest-in-class microscanners available, promises to not only increase frame or volume rates for higher data acquisition rates in OCT, but also enable precision 2-D scanning for other scanning modalities including fluorescence confocal and nonlinear microscopy.

Materials and Methods

This work was performed in collaboration with the VA Boston Healthcare System (Dr. Hiroshi Mashimo MD PhD and staff at the Endoscopy Unit), Thorlabs (Dr. Benjamin Potsaid) and Praevium Research (Dr. Vijaysekhar Jayaraman) for use of prototype swept source technology.

A schematic and photograph of the cycloid imaging capsule is given in Fig. 1. A piezoelectric tubular actuator scanned a fiber cantilever at its resonant scan frequency 7030 Hz to produce a 1 mm diameter circle in the focal plane. The circle was then scanned circumferentially by a micromotor at 3 Hz to produce a 1 mm x 38 mm 2-D strip FOV in a cycloid scan pattern[131] (Fig. 2a-b), which could be continuously acquired without scanner flyback.

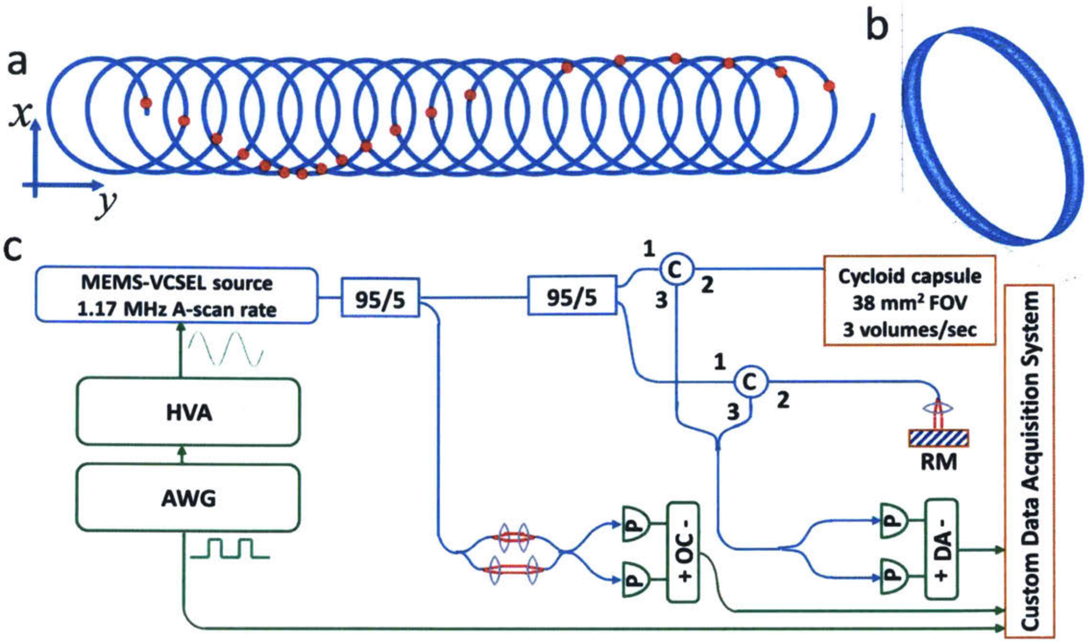

Fig. 2. (a) Schematic of cycloid scanning geometry when unwrapped on to a flat plane. The red dots indicate spots of each circle scanned at equal temporal frame intervals, showing the slow local rotation of the circle about its center during the scan due to the mirror inversion effect. (b) 3-D plot of the cycloid scan in the device geometry. (c) Ultrahigh speed OCT system. HVA: high-voltage amplifier. AWG: arbitrary waveform generator. C: circulator. RM: reference mirror. P: photodetector. OC: optical clock. DA: differential amplifier.

A. Cycloid scan

The scan geometry is known as a 'prolate cycloid', which is part of the larger family of trochoid curves[132]. The scan pattern consists of a circle translated by a length many times the circle diameter to produce a densely sampled strip. As the circular scan is reflected radially by the prism and rotated around the central axis of the motor, the circle is also incrementally rotated about its center (Fig. 2a), due to the mirror property of inverting (or 'reversing') an image in the axis perpendicular to its surface. Therefore, a fast 1-D line scan in this configuration would not generate a raster-like scan or sweep out a strip, but instead generate a translating and rotating line scan. This motivates the need for a 2-D circular scan. The mathematical equations defining the cycloid trajectory are derived as follows:

$$\begin{aligned}
\begin{bmatrix} x \\ y \end{bmatrix} &= Rot(\theta) \times \begin{bmatrix} \mathrm{r}\sin(2\pi f_{fast}t) \\ \mathrm{r}\cos(2\pi f_{fast}t) \end{bmatrix} + \begin{bmatrix} 0 \\ 2\pi R f_{slow} t \end{bmatrix} \\
&= \begin{bmatrix} \cos(2\pi f_{slow}t + \phi) & -\sin(2\pi f_{slow}t + \phi) \\ \sin(2\pi f_{slow}t + \phi) & \cos(2\pi f_{slow}t + \phi) \end{bmatrix} \times \\
&\quad \begin{bmatrix} \mathrm{r}\sin(2\pi f_{fast}t) \\ \mathrm{r}\cos(2\pi f_{fast}t) \end{bmatrix} + \begin{bmatrix} 0 \\ 2\pi R f_{slow} t \end{bmatrix} \\
&= \begin{bmatrix} \mathrm{r}\sin(2\pi(f_{fast} - f_{slow})t - \phi) \\ \mathrm{r}\cos(2\pi(f_{fast} - f_{slow})t - \phi) \end{bmatrix} + \begin{bmatrix} 0 \\ 2\pi R f_{slow} t \end{bmatrix}
\end{aligned}$$

$Rot(\theta)$ is a rotation matrix, where θ is the instantaneous angle of local rotation that is applied to the circular (fast) scan trajectory, and is a function of the instantaneous angular position of the prism on the micromotor circumferential rotation (slow) axis. The linear term in the slow axis is due to the micromotor scan producing a translation along the circumferential axis. The local rotation has the effect of slowing down (or speeding up) the effective speed of the circular scan, depending on the micromotor direction of rotation. f_{fast} and f_{slow} refer to the resonant frequency of the fast circular scan and the rotational speed of the slow micromotor scan, respectively. r and R are the radii of the circular scan in the focal plane, and capsule respectively. The angular offset ϕ refers to the initial rotational orientation of the circular scan due to the initial angular position of the circle on the capsule circumference at the start of the scan volume. ϕ is a critical parameter in achieving accurate reconstruction since all other parameters in the equations are pre-determined design constants.

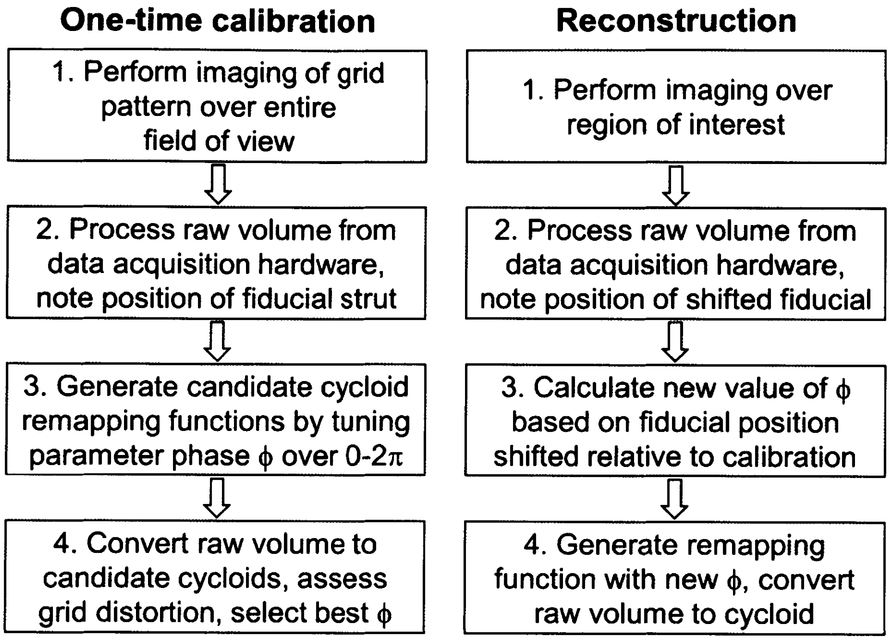

Fig. 3. Flowchart of one-time calibration and reconstruction procedures for cycloid scan trajectory.

B. OCT system

The OCT system (Fig. 2c) was a dual-circulator interferometer and used a 1.3 μm tunable MEMS-VCSEL swept light source [63] running at 583,490 Hz bi-directional sweep rate, which produced 1,166,980 Hz A-scan rate. The A-scan rate was tunable and chosen based on the piezoelectric resonant scan frequency 7030 Hz to have an integer (166) number of A-scans per circular scan frame, to facilitate synchronization and reconstruction. The A/D card (ATS 9370, AlazarTech) was optically clocked by a Mach-Zehnder interferometer up to a fringe frequency of 1.1 GHz to achieve an imaging range of 2.0 mm in air. The power incident on the sample from the capsule was 20 mW. The VCSEL sweep bandwidth was 115 nm, and the axial resolution was 12 μm in air (8.5 μm in tissue). The measured system sensitivity was 102 dB using a single reflection from a flat-cleaved fiber in the sample arm, and 98 dB overall after subtracting 4 dB to account for a round trip through the imaging capsule, which had ~60% one-way (~36% round trip) optical transmission.

C. Capsule construction

The cycloid scanning capsule was assembled as follows. A quadrupole piezoelectric tube fiber scanning device was first constructed; this has been reported previously by other groups[60, 64]. An angle-cleaved optical fiber was mounted to the tip of a 1.5 mm diameter piezoelectric tubular actuator (Boston Piezo-Optics, MA), which was enclosed in a 12G (2.8 mm diameter) hypodermic tube. The piezoelectric tube was 4 mm length, cut using a diamond saw from a standard half-inch length provided by the supplier. The actuator was centered within and electrically separated from the hypodermic tube housing by a sapphire spacer. The resonant frequency was determined by fiber length and could be mathematically predicted (see Chapter 2) [64] and experimentally verified. The resonance was selected to be about 7 kHz (corresponding to a scanning fiber length of ~3.8 mm), and measured to be 7030 Hz. The resonant fiber construction technique was similar to the previous description in Chapter 2, thus Q-factors were similarly >100. This was generally necessary to achieve large deflections at moderate voltages, although the scanning fibers were not driven to full amplitude in this study, due to prior failures where the scanning fiber broke at large amplitudes possibly due to the short fiber length. A 0.25 pitch gradient index (GRIN) lens (Edmund Optics) was inserted into the tube housing in front of the fiber at a separation that determined the working distance of the optical system. The transverse resolution was designed to be 30 μm FWHM based on simulations (Zemax) with diffraction-limited performance on- and off-axis. Best efforts were made to adhere to the simulated design, including use of GRIN lenses with factory cut pitch, and optical alignment performed under a magnification stereoscope. The resolution was verified by a knife edge (90-10) power measurement. The focal plane had slight variation in position around the circumference due to imperfect centration of the micromotor and scanning fiber, and the non-telecentric scan. Aberrations due to the off-axis scan rotated with the circular scan after reflection by the prism, and the plastic outer tube contributed additional aberration, although these were minimal. These effects will be exacerbated in future higher numerical aperture systems which will likely require custom lens designs. The piezoelectric actuator was soldered to a multi-conductor cable (Cooner Wire, CA). The shaft of the 4 mm diameter micromotor (Namiki, Japan) was mounted with a 6 mm diameter brass disc, which increased moment of inertia for smooth rotation at low speeds. The disc was then mounted with a 2 mm Al-coated prism. The fiber scanner and micromotor were then mounted in 3D-printed holders, which fit snugly and were self-centering within a medical grade polycarbonate plastic machined tube with hemispherical ends.

D. Scanner control and data acquisition

Custom software written in C++ controlled the resonant fiber scanner, and OCT image acquisition/display. A National Instruments D/A board generated 2-channel sinusoidal output with equal and constant amplitude and a phase difference to actuate the fiber scanner and produce a circular scan. The sinusoidal outputs were amplified by a custom voltage amplifier circuit with current limiting capability, to 30 V amplitude a.c., which generated a rapid ~1 mm diameter circular scan in the focal plane. This is below the International Electrotechnical Commission 60601-1 stipulated limit of 42 V amplitude a.c. for medical devices [65]. The micromotor was driven by a driver board (Namiki), generating a slow 38 mm scan around the capsule circumference. The acquisition was synchronized to the resonant fiber trajectory, while the micromotor was externally driven by the driver board, and thus a one-time calibration procedure was required for image reconstruction (section E, Fig. 3, and Supplementary Information). In this study, the resonant frequency was 7030 Hz (166 A-scans per circular scan for ~½ Nyquist sampling in the fast axis) and the micromotor rotation was 3 Hz (2322 circular scans per volume for ~Nyquist sampling in the slow axis) for structural OCT imaging, and 0.5 Hz (13932 circular scans per volume) for OCTA. The volume was then remapped to a 100 x 3800 pixel Cartesian grid based on the theoretical scan trajectory equations from section A above.

E. Image calibration and reconstruction

A circular scan of the resonant fiber was generated by applying two phase-separated sinusoidal drive signals to the piezoelectric tube. The phase difference is theoretically 90°, but required a one-time adjustment due to slight asymmetry of the fiber scanner mount and quadrupole electrodes on the piezoelectric tube. With the micromotor stationary, the phase difference between the sinusoids was empirically tuned until the scan was assessed visually to be sufficiently circular. The only parameter to be determined in the scan trajectory was the phase term ϕ (see section A above), which described the initial rotational orientation of the circle at the start of each acquisition, and is determined by the starting angular position of the micromotor.

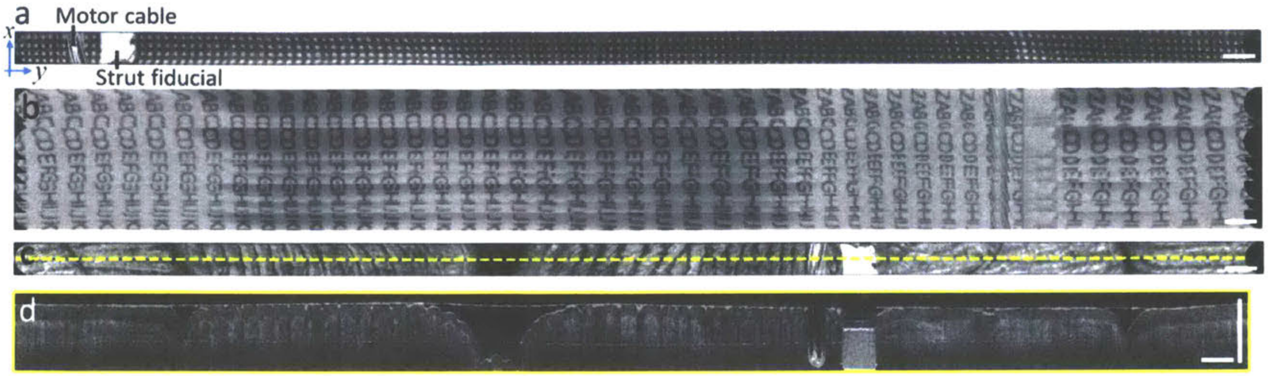

Fig. 4. Benchtop imaging. (a) *En face* OCT strip image of printed paper grid. (b) Large field mosaic of 10 sequential strip volumes acquired continuously while manually translating over alphabetically ordered letter grid. (c) *En face* OCT of human fingers/palm, showing fingerprints and skin creases. (d) Cross-sectional image from center line of volume. *En face* images are mean projections of 800 μm depth. Scale bars are 1 mm.

The acquisition was always triggered at the same phase within the period of the sinusoidal drive waveforms (in phase), therefore the acquisition always started at the same angular position within the circular scan relative to the fiber scanner mount, before reflection by the prism. However, the initial angular position of the micromotor was unsynchronized to the acquisition, which at the start of every acquisition imparted an arbitrary rotational orientation to the circular scan after reflection by the prism. In order to achieve accurate remapping and reconstruction, a one-time calibration procedure (Fig. 3) was carried out. First, a one-time imaging of a grid pattern was performed, in which a 'calibration phase' ϕ_0 was empirically tuned in post-processing until the grid was correctly reconstructed. Thereafter, images acquired at different micromotor angular start positions could be reconstructed by calculating the shift ϕ_1 of the micromotor angular position relative to the calibration image, which could be determined by locating a fiducial (Fig. 4) in the image produced by an internal strut. The fiducial was well-resolved, albeit distorted in the raw unreconstructed image, enabling its use as a marker of micromotor relative angular position even before reconstruction. The absolute shift $\phi = \phi_0 + \phi_1$ could then be applied to the scan trajectory for reconstruction (Supplementary Information).

Raw data volumes were converted to Cartesian coordinates by remapping data points to their theoretical location in time based on the mathematical trajectory. For rapid reconstruction and preview in the acquisition software, trading off image quality, lookup tables were created in MATLAB (MathWorks, MA) based on nearest neighbor interpolation of a Cartesian grid, such that each grid coordinate was mapped directly to a single A-scan in the acquisition. 12 lookup tables were pre-generated using 12 equally spaced values of ϕ from 0 to 2π and used as remapping functions. One of the 12 lookup tables could then be user-selected upon viewing the real-time previews, for an approximate reconstruction using CPU processing in C++. For the purposes of previewing, it was not necessary to use a more precise ϕ since this could be further tuned in post-processing. When the volume rate was 3 Hz, the acquisition time per volume was ~0.3 sec, and the nearest neighbor reconstruction took ~1.5 sec, for a volumetric display rate of ~0.5 volumes/sec. Future graphics processing unit (GPU) implementation should improve these speeds. When post-processing for optimal image quality, a more precise ϕ was calculated based on the exact fiducial location, and remapping was performed with cubic spline interpolation for higher quality reconstruction, which took several minutes for each volume in MATLAB. This can also be sped up in the future using GPU-accelerated processing. Larger FOVs were imaged by translating the capsule via the tether, and sequential strip volumes were mosaicked by manual alignment with visual inspection. OCTA was generated by computing OCT signal decorrelation between sequential circular scans (Supplementary Information). *En face* images were displayed in square root scale and depth-projected down to 800 μm depth for optimal contrast, although depth-resolved imaging at specific depths was also possible. Cross-sections analogous to traditional B-scans were extracted from reconstructed volumes and displayed in logarithmic scale. Parasitic reflection artifacts were cropped from cross-sections in regions of low/no signal deep in tissue. Images of living tissue were displayed in sepia for improved contrast. Co-registered OCT/OCTA images were depth projected over 400 μm depth, because deeper image depths had low-signal OCT and generated OCTA that had decorrelation arising from noise rather than blood flow.

F. Clinical imaging protocol

The imaging protocol was approved by Institutional Review Board committees at the Massachusetts Institute of Technology (MIT), Veterans Affairs Boston Healthcare System (VABHS), and Harvard Medical School. Written informed consent was obtained prior to imaging. Imaging was performed at the VABHS endoscopy unit. The patient underwent bowel preparation, and was sedated as per colonoscopy protocol. The capsule was introduced by the endoscopist into the patient's anal canal and rectum, before performing colonoscopy. Capsule positioning was guided by real-time *en face* and cross-sectional OCT imaging. For mosaicking, sequential image volumes were continuously acquired while the operator pulled back or advanced the capsule manually at about 1-2 mm/s, which enabled at least partial overlap of the sequential strip volumes. For structural OCT imaging, the micromotor was set to rotate at 3 Hz. For decorrelation-based OCTA imaging, the micromotor was set to rotate at 0.5 Hz. After OCT imaging was complete, the capsule was withdrawn and the endoscope was introduced for standard colonoscopy.

Results and Discussion

A. Benchtop validation

A printed paper grid pattern of 250 µm pitch was imaged to validate the scanning mechanisms and reconstruction algorithm. *En face* OCT imaging of the grid wrapped around the capsule circumference showed good scan accuracy with minimal distortion (Fig. 4a). To demonstrate image mosaicking for a larger FOV, imaging was performed on an alphabetically ordered letter grid rolled into a paper tube, with the capsule pulled back by hand at ~1-2 mm/s through the tube during continuous volumetric acquisition (Fig. 4b). 10 sequential image volumes were acquired over 3.3 seconds and could be approximately mosaicked to achieve a ~4.5 mm × 38 mm field. The 10 volumes were part of a longer 30-volume acquisition that was used to generate a 10-second video at 3 volumes/sec (Supplementary Video 1). The video enables an assessment of volume-to-volume repeatability, as well as overall performance of high volume rate cycloid scanning OCT.

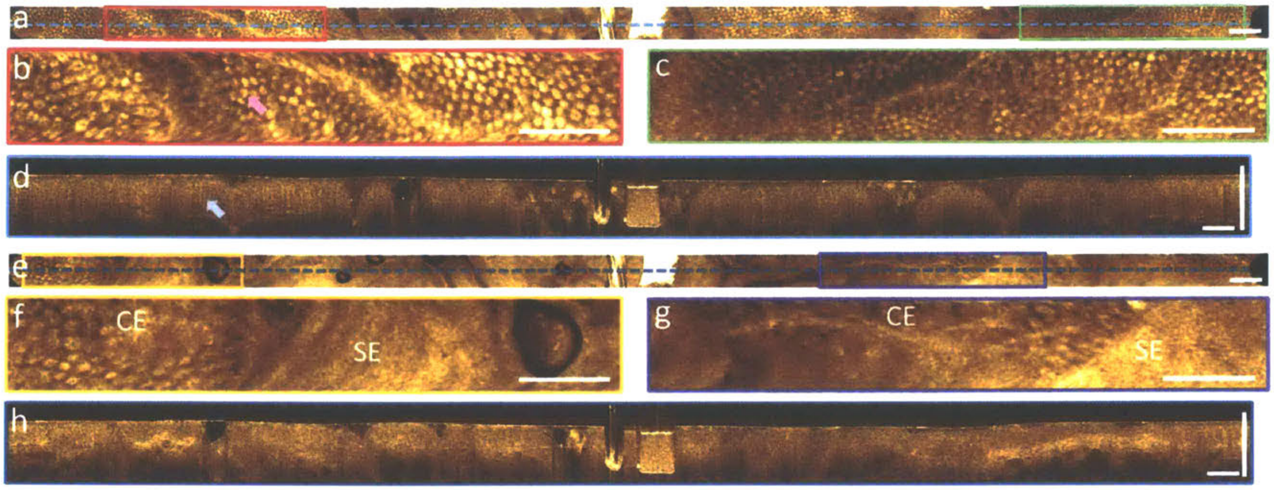

Fig. 5. Imaging in human subject. (a) *En face* OCT image of human rectum. (b, c) Enlargements visualizing crypt structures (pink arrow) of columnar epithelium. (d) Cross section showing vertical crypt architecture (blue arrow). (e) *En face* OCT image of the dentate line (squamo-columnar junction). (f, g) Enlargements showing the tissue boundary between columnar epithelium (CE) and squamous epithelium (SE). (h) Cross section showing crypt architecture, and squamous epithelium from anal canal. *En face* images are mean projections of 800 μm depth. Scale bars are 1 mm.

The slow manual longitudinal pullback of the capsule produced a tilt in the letter rows, because the capsule was translated longitudinally during the concurrent rotary scan in the orthogonal direction. The non-uniform speed of the pullback caused the tilts to appear misaligned. Certain letters appeared repeated when the manual pullback was momentarily slower. Loose contact of the paper tube on the capsule allowed the latter to slide, but led to varying contrast along the length of the strips, and contributed in part to apparent misalignment of the lettering. The micromotor exhibited non-uniform rotational distortion (Supplementary Information) that also contributed to misalignment. Imaging was performed with the capsule gripped in the hand, such that the *en face* plane showed well-resolved fingerprint contours and palm skin creases (Fig. 4c). Cross-sectional images were also extracted from the reconstructed volume along the slow circumferential axis, which showed depth-resolved imaging into the dermis, similar to traditional OCT B-scans (Fig. 4d).

B. Clinical imaging

Imaging was performed with a patient scheduled for routine surveillance colonoscopy, during which there were no notable endoscopic findings. OCT structural imaging in the rectum showed regular patterns indicative of rectal crypt structures in the *en face* plane (Fig. 5a-c), while cross-sectional images showed vertical features from crypt architecture and good tissue penetration to about 800 μm depth (Fig. 5d). Imaging at the dentate line showed tissue transition from intestinal crypts of the rectum to relatively smooth squamous epithelium in the anal canal (Fig. 5e-g), and the cross-sections showed strong OCT signal from regions of squamous epithelium (Fig. 5h). Large FOV mosaics were generated by manually advancing the capsule into the rectum and continuously acquiring sequential image volumes.

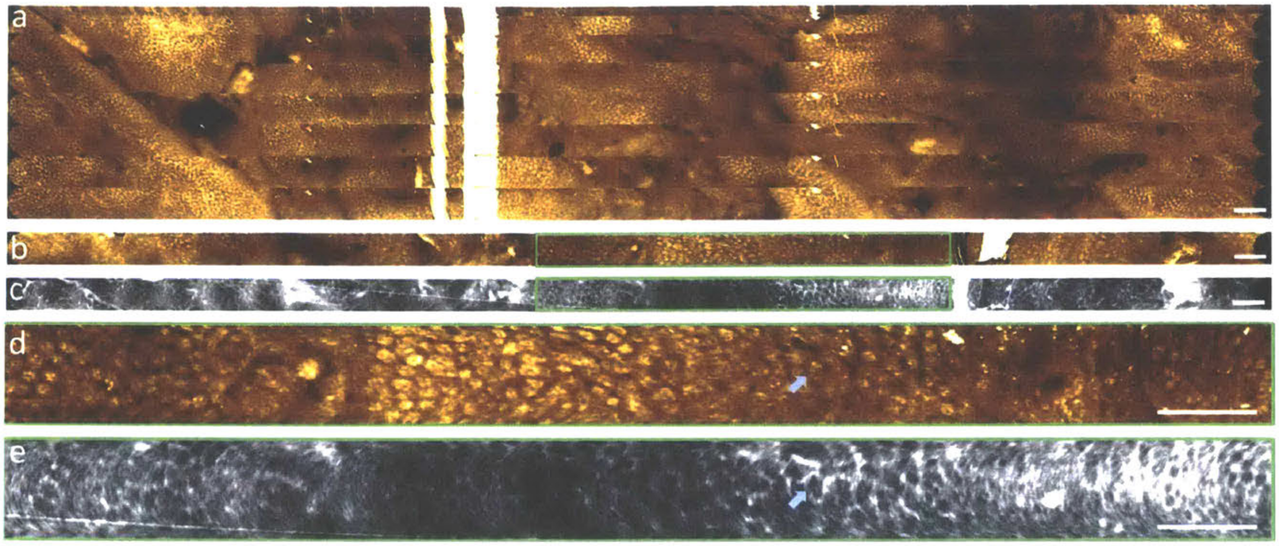

Fig. 6. (a) Large field mosaic of 10 sequential strip volumes covering a ~7 mm x 38 mm FOV acquired continuously while pushing capsule into rectum at 1-2 mm/s. *En face* images are mean projections of 800 μm depth. (b, c) Co-registered OCT and OCTA in rectum. *En face* images are mean projections of 400 μm depth. (d, e) Enlargements showing regular crypt patterns and a honeycomb vascular network encircling the crypts. Arrows point to a crypt encircled by vasculature. Scale bars are 1 mm.

The volumes generated a large FOV with *en face* features approximately mosaicked by manual alignment (Fig. 6a). Each strip of the mosaic showed accurate scanning and undistorted features. Despite non-uniform speed of the manual longitudinal scan, the partial overlap of each image volume enabled approximate registration and mosaicking based on *en face* features. Co-registered structural and angiographic OCT in the rectum showed regular crypt patterns and a honeycomb vascular network encircling the crypts [133] (Fig. 6b-e), corresponding to lamina propria regions between crypts. In the center of the enlargement (Fig. 6d-e), the crypts appear compressed, which could have resulted in slower flow and reduced vascular contrast in that region of the OCT angiogram. The arc-like noise artifacts mimicking the cycloid trajectory were likely due to 1. synchronization errors between the D/A output and the resonant fiber scanner resulting in small fluctuations in output frequency, 2. the incremental local rotation of the circular scan about its center during the slow micromotor scan, and 3. parasitic tissue motion. These factors produced small frame-to-frame misalignment, which were indiscernible in the structural OCT images but produced OCTA decorrelation noise.

To our knowledge, this study is the first demonstration of cycloid scanning for rapid, wide field endoscopic OCT imaging. The combination of piezoelectric resonant scanning and micromotor scanning enables high precision while also covering a large FOV. The cycloid promises to enable minimally invasive catheter / endoscope imaging not only for high speed OCT systems, but also for fluorescence confocal and nonlinear microscopy. The study also shows the potential of tethered capsules to image the rectum without endoscopy, extending previous capsule esophageal imaging applications. ~50% of colorectal cancers occur in the rectum and distal colon[134], which suggests that tethered capsules could be a screening tool for a large subset of colorectal cancers.

The cycloid scanner is an important technology for enabling distal 2-D scanning side view endomicroscopy. SECM was previously reported for rapid 2-D reflectance confocal microscopy, but has a limited strip width (~200 µm), visualizes a 2-D *en face* plane, and is incompatible with scanning microscopies such as fluorescence confocal or nonlinear microscopy[93]. Furthermore, SECM generates a rapid line scan with a swept wavelength source, and therefore cannot be used for volumetric swept source OCT. The cycloid scanner enables strip imaging at volumetric rates similar to reported capsule SECM frame rates, but with 3-D depth-resolved imaging and nearly 9x larger strip FOV[93]. The cycloid scanner can be extended to finer transverse resolution using a high NA design as suggested in previously reported capsule designs using a focusing objective rotated by the micromotor[54, 55].

The cycloid is simpler to calibrate than the spiral scan, and images can be reconstructed using theoretical equations describing the trajectory. The spiral scan requires amplitude modulation for the slow scan axis and is known to require frequent calibration, as well as complex drive waveforms to rapidly reset the spiral[60]. Moreover, amplitude modulation presents challenges including transient behavior, phase variation in resonance decay, and mode coupling (cross-coupling) between orthogonal fiber axes. These difficulties can also hinder attempts to perform other 2-D scans such as a linear scan with a rotating axis. By contrast the cycloid scan requires only a resonant circle at fixed amplitude, which remained repeatable with the same drive parameters over extended periods of several months without recalibration. The micromotor can scan continuously to acquire sequential strip volumes without interruption from flybacks or resets which are needed in other scanning methods.

Commercial catheter/endoscope OCT systems perform real-time, cross-sectional imaging in the rotary side-viewing direction, and volumetric data is acquired by a slow longitudinal pullback at the proximal end of the device. Side view distal 2-D scanning suggests a new paradigm for real-time *en face* OCT imaging that provides rapid volumetric, orthoplane visualization by precision scanning a local region of interest, while also covering a wide circumferential strip. As discussed previously, larger FOVs can be achieved by proximal pullback of the device, mosaicking the circumferential strips to map large regions of luminal organs. The ability to rapidly acquire and view strips of data while also comprehensively imaging a large FOV promises to improve the diagnostic utility of OCT.

The tethered capsule cycloid scanner device has applications in both sedated and unsedated imaging of the gastrointestinal tract. More compact microscanners such as smaller or flat micromotors and smaller piezoelectric actuators can be used to reduce the rigid length or diameter of the device, improving compactness and broadening potential clinical applications. Moreover, the cycloid scanner can also be used for small diameter imaging catheters, laparoscopes, or other minimally invasive devices. Smaller diameter cycloid scanners will enable higher NA focusing and faster volume acquisition rates than the large diameter capsules demonstrated in this study. The cycloid scanner is π times less efficient than a raster scan (Supplementary Information), while resonant and micromotor scanners require high data sampling rates. Recent progress in multi-MHz OCT systems[135] using high speed swept laser technology, fast data acquisition cards, GPUs and parallel processing is synergistic with rapid scanning. Fluorescence confocal and nonlinear microscopy can achieve 10s of MHz data rates. Cycloid scanners promise to enable a wide range of *in vivo* microscopy applications.

Conclusion

We demonstrate a new cycloid scanning technology that can be integrated into endoscopic devices for side view, distal 2-D precision scanning and wide FOV imaging. Tethered capsule imaging was demonstrated using swept source OCT at 1.17 MHz axial scan rate with 1 mm x 38 mm fields acquired at 3 volumes/sec and larger FOVs achieved by proximal pullback and mosaicking. The current study demonstrates cycloid scanning with a tethered capsule, but this method is also applicable to small diameter catheters, laparoscopes and other imaging devices. The ability to perform high speed, precision distal scanning promises to be enabling not only for OCT, but also for fluorescence confocal and nonlinear microscopy.

Supplementary Information

A. Scanner control and software acquisition/display

During imaging, it is important to ensure continuous circular scanning of the piezoelectrically actuated resonant fiber, to avoid transients that would limit volumetric acquisition speeds. Therefore, the sinusoidal outputs were continuously generated from a D/A card (National Instruments (NI) DAQ) to actuate the resonant fiber. The D/A was externally clocked by the swept laser trigger (583490 Hz) to optimize timing synchronizations and accuracy of the generated sinusoidal frequency 7030 Hz. The forward and backward sweep of each laser sweep period were used to generate 2 A-scans. Each circular fiber scan was stored as one frame consisting of a fixed integer number of 166 A-scans.

The micromotor was driven by a vendor-provided board with its own output sampling clock. To optimize synchronization between the micromotor rotation rate and the volumetric acquisition rate, the number of circular frames per volume was one-time empirically tuned such that the volumetric period was approximately equal to the micromotor rotation period. The image acquisition software had a preview mode in which a volume was continuously acquired, processed, and displayed in real time. Tuning of the volumetric period was aided by the software preview, in which the strut fiducial in the *en face* image plane could be observed to be drifting lengthwise if the micromotor and the volumetric rate were not adequately synchronized.

A 'volume trigger' waveform and the two sinusoidal waveforms for driving the piezoelectrically actuated resonant fiber were simultaneously generated from the D/A card using acquisition software (Fig. S1). The volume trigger was a pulse with period equal to the volume period in phase with the sinusoidal waveforms, and triggered the start of a volumetric acquisition. Once the software completed processing and displaying a volume, the A/D card (AlazarTech) read in the next volume trigger for the subsequent acquisition. This ensured that all acquired volumes were synchronized to the same reconstruction parameter ϕ .

The acquisition software used the CPU to process the OCT raw data, therefore the speed was modest and volumetric image preview was limited to ~0.5 volumes/sec. Future work utilizing GPU processing would achieve preview rates limited only by scanner speeds[70]. For data acquisition of single or multiple volumes, the raw data was continuously streamed to memory without processing, such that the volumetric data acquisition rate was the same as the micromotor scanner speed (3 volumes/sec).

B. Image reconstruction

For imaging a large FOV, multiple sequential volumes were continuously acquired starting from a single 'volume trigger' (explained in section A), which resulted in a small accumulated timing drift due to a small error in either the actual resonant frequency of the fiber scanner or the empirical synchronization of the micromotor rotation speed. This manifested as a 2 A-scan lag per volume (or 2/2322 A-scan lag per frame) for the second and subsequent volumes. The lag could be measured by a 1-D correlation or visual inspection of the first acquired frame of each volume. An alternative way to understand this error is that it results in the subsequent volumes being acquired starting at a slightly later point on the first circular scan of a subsequent volume compared to the first scan of the first volume. This produced a shift in the reconstruction phase ϕ, which is $\phi_{drift} = [2\ \text{Ascans/(166 Ascans/frame)}] \times 2\pi \approx \pi / 36$. Therefore, for the nth volume reconstruction of a multi-volume sequence, ϕ was offset by $+(n-1)\pi / 36$. This error was consistent and could be compensated by a one-time correction. Failure to account for this small error in ϕ resulted in accumulated distortion in subsequent image volumes.

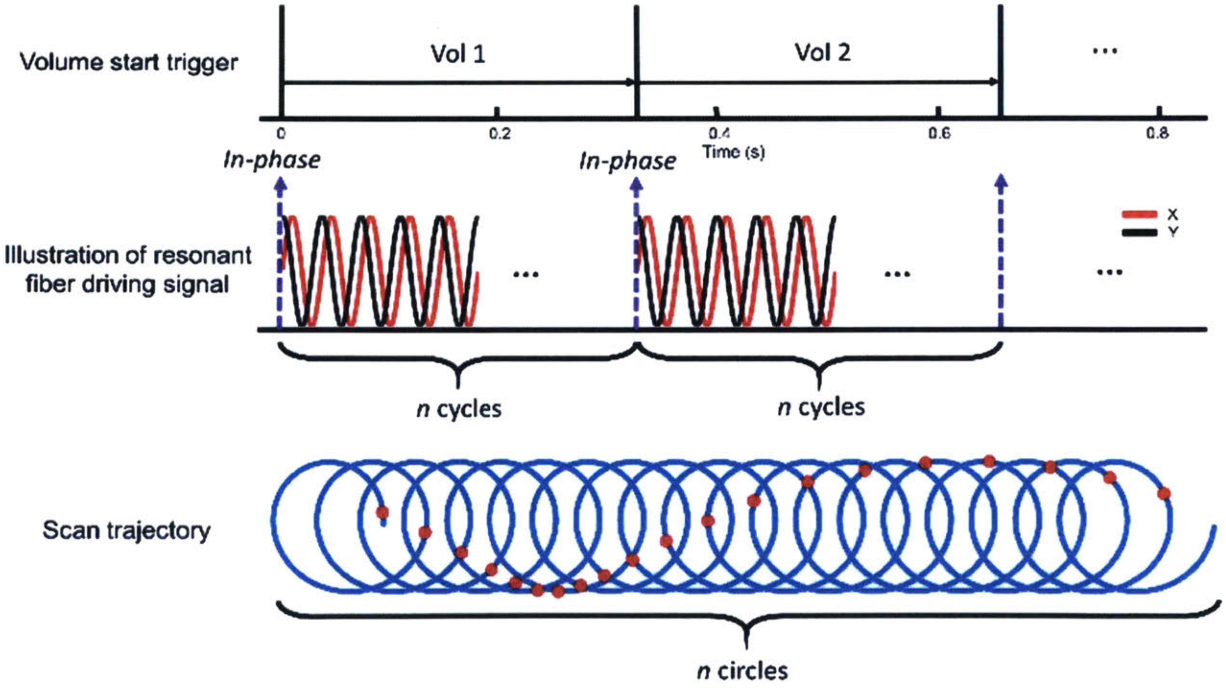

Fig. S1. Timing and driving waveforms of the cycloid scanning protocol. *n* is the number of circular scans per volume and was empirically selected to be 2322 and 13932 to synchronize with the micromotor rotation speed for structural (3 volumes/sec) and angiography imaging (0.5 volumes/sec), respectively.

The entire set of points on the scan trajectory was not required for image reconstruction. The circular scan has the property that it rescans areas already covered by earlier circles in the cycloid trajectory. The leading (left) or trailing (right) half of each circular scan could be used individually for reconstruction. If the entire circular scan was used such that rescanned points were included in the remapping function, distortions would be introduced into the image (Fig. S2(a, d)). This was attributed to the circular scan not being perfectly circular and uniform, resulting in rescanned points producing slightly differing images because the circular scan rotates. The non-telecentricity of the scan also resulted in variation of the optical resolution within the circular scan, producing asymmetry in the scan. In theory, the circularity could be improved by carefully tuning the parameter space of scan amplitudes and phase while monitoring the circularity on a position sensitive detector. However small drifts in the resonant frequency caused by temperature or other fluctuations could potentially lead to non-circularity. Therefore, achieving perfect circularity was considered less important than operational simplicity. When processing images using either the trailing (Fig. S2(b, e)) or leading (Fig. S2(c, f)) halves of the circular scan, the scan accuracy observed by scanning a grid appeared acceptable when the two images were assessed separately, but were slightly asymmetric when compared. Combining data from each half, i.e. including data that was rescanned by a later circular scan in the trajectory resulted in distortions. Therefore, each volumetric acquisition resulted in two nearly identical volumes, which are separated temporally by the time taken to longitudinally scan through half a circle width, i.e. the time taken for the leading half of the circular scan to rescan the same area that was earlier scanned by the trailing half. For consistency, all data was processed using the leading half-circle. Future work may investigate the potential for dewarping the images to generate a single combined image volume with potentially improved sampling and image quality.

Figure S3 shows a set of 5 sequential volumes acquired as part of a series of 30 volumes. Figure S3 enables an assessment of volume-to-volume repeatability. The 5 volumes as static images do not show apparent differences when assessed by eye. This was due to non-uniform rotational distortion (NURD) of the motor, producing non-constant angular velocity on the slow rotary (circumferential) scan. Increasing the rotary speed can substantially improve NURD while increasing volume rates, and would be especially relevant to smaller diameter devices that have smaller fields of view.

C. OCT angiography processing

The resonantly scanned circular scan frames did not require any rigid or non-rigid registration before computing speckle decorrelation, which is typically required for micromotor-based rotary scanning OCTA. Also, the lag/lead in the fast axis scan speed due to the slow local rotation of the circular scan was very small and thus did not require re-sampling. Rotation of the micromotor at 0.5 Hz was required in order to obtain usable OCTA, which amounted to ~6x Nyquist sampling in the slow scan direction. Significant oversampling was required, to compensate for the undersampling (½ Nyquist) in the fast scan direction and obtain sufficient scan overlap between adjacent frames. The frames were filtered by a 3 x 3 Gaussian kernel before computing decorrelation. Speckle decorrelation was calculated before Cartesian remapping, by element-wise computation using adjacent pairs of raw circular frames with the formula[57]:

$$D_n = 1 - A_n A_{n+1} / \tfrac{1}{2}(A_n^2 + A_{n+1}^2)$$

n is the non-remapped frame number and A_n the OCT amplitude of frame n. A 3-frame moving average of the decorrelation was calculated to reduce noise. The frames were then remapped to a Cartesian grid, similar to the structural data.

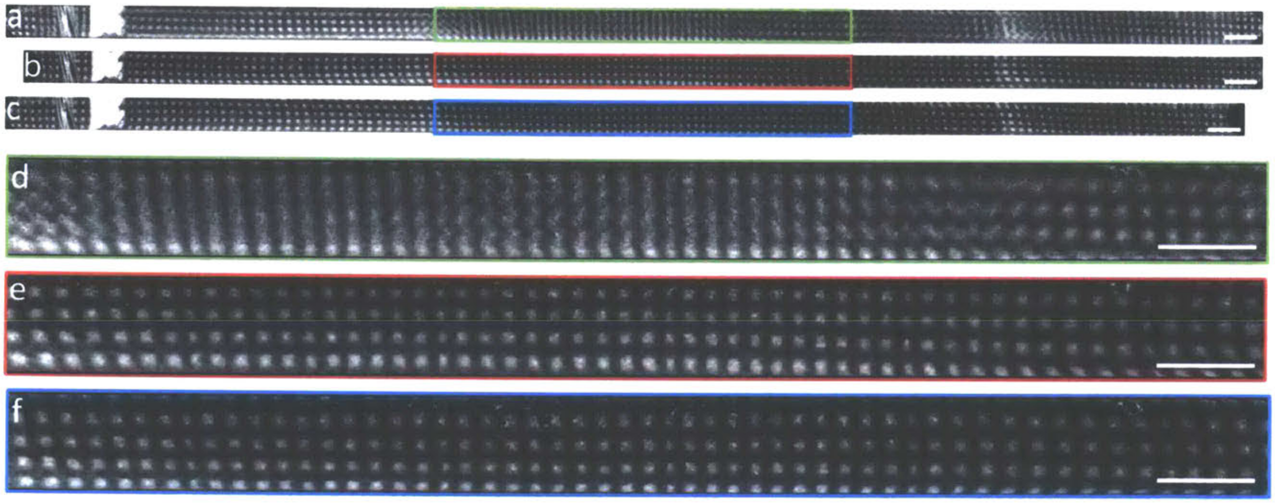

Fig. S2. An image of a printed paper grid with 250 μm pitch, reconstructed using (a) all scanned points, (b) the trailing (right) half of the circular scans, (c) the leading (left) half of the circular scans. (d, e, f) Enlargements showing scan distortions occurring when entire circular scan is used, and slight asymmetry between the use of either half of the scan. Scale bars 1 mm.

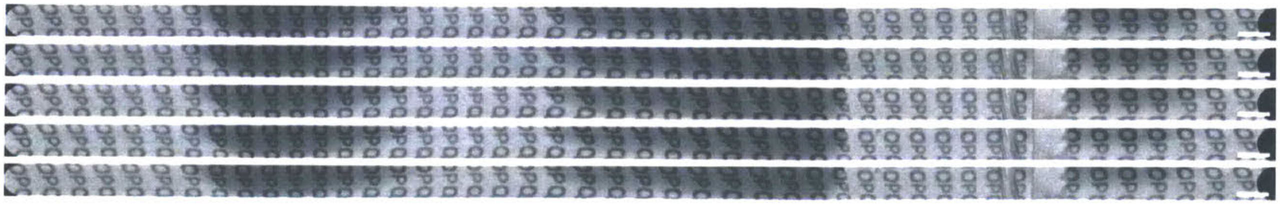

Fig. S3. Sequential volumes of an alphabetically ordered letter grid continuously acquired over the same location, to illustrate repeatability.

D. Cycloid scan efficiency comparison

Efficiency is defined here as being inversely proportional to the time taken for a scan pattern to Nyquist-sample a given area and normalized to the scan area. The efficiency of the cycloid scan is compared to the linear raster scan (ideal efficiency), as well as the sinusoidal raster scan and the spiral scan, which are commonly used resonant scans.

A **linear raster** covering an area of $D \times L$ requires $D/(\omega/2) \times L/(\omega/2)$ A-scans for Nyquist sampling, where D, L, and ω are the width, longitudinal length, and spot size. Therefore the scan time is $T_{\text{linear raster}} \propto D/(\omega/2) \times L/(\omega/2) = 4DL/\omega^2$.

Normalizing, $\mathit{Efficiency}_{\text{linear raster}} \propto \omega^2/4$.

A **sinusoidal raster** scan has a displacement of $(\mathrm{D}/2)\sin(2\pi t/\tau)$ along the width D, which has period τ and a maximum velocity of $\pi D/\tau$. Let this maximum velocity give Nyquist sampling. Comparing the sinusoidal raster scan to a linear raster scan at this maximum velocity, the former would take $\tau/2$ to cover one width D, while the latter would take τ/π. Therefore the sinusoidal scan is $\pi/2$ slower than the linear raster. The scan time is $T_{\text{sin raster}} \propto 2\pi DL/\omega^2$.

Normalizing, $\mathit{Efficiency}_{\text{sin raster}} \propto \omega^2/2\pi$.

A resonant **spiral scan** requires $\pi D/(\omega/2)$ A-scans in the outermost circle for Nyquist sampling, where D is the diameter. A resonant scanner has a fixed angular velocity producing non-uniform sampling, such that inner circles with smaller circumferences are more densely sampled than outer circles. It also requires $D/2/(\omega/2)$ circles for Nyquist sampling in the radial axis. The scan time is $T_{\text{spiral}} \propto \pi D/(\omega/2) \times D/2/(\omega/2) = 2\pi D^2/\omega^2$.

Normalizing, $\mathit{Efficiency}_{\text{spiral}} \propto \omega^2/8$. The scan time is the same as the sinusoidal raster (if L = D) but with lower efficiency, and the spiral area is potentially smaller and of order D^2.

A **cycloid scan** requires $\pi D/(\omega/2)$ A-scans in each circle for Nyquist sampling. It also requires $L/(\omega/2)$ circles for Nyquist sampling over the longitudinal strip, when using one half of each circular scan (not using rescanned points). The scan time is $T_{\text{cycloid}} \propto \pi D/(\omega/2) \times L/(\omega/2) = 4\pi DL/\omega^2$.

An alternate derivation is that the cycloid also has a sinusoidal velocity along the width similar to the sinusoidal scan, but takes τ (twice longer) to cover one width D because the rescan is not used.

Normalizing, $\mathit{Efficiency}_{\text{cycloid}} \propto \omega^2/4\pi$. The cycloid is $\pi/2$ less efficient than the spiral, but has free choice of L for a larger field. The cycloid is twice less efficient than the sinusoidal raster if the rescanned points are not used.

Chapter 6

Tethered capsule *en face* and cross-sectional OCT imaging in unsedated patients

Introduction

Esophageal adenocarcinoma (EAC) precursors are Barrett's esophagus (BE) and dysplasia. However, >90% of EAC patients have never had an endoscopic BE diagnosis[136] and 40% do not report symptoms of chronic gastroesophageal reflux disease[4], which is a primary indication for endoscopic screening. Therefore, current endoscopic screening recommendations have had limited efficacy in preventing EAC.

Simple and low-cost screening/surveillance modalities are needed to detect BE and dysplasia in a broader population than existing paradigms. The Cytosponge has been validated in large trials with 80% sensitivity and 92% specificity for BE detection[137]. Unsedated transnasal endoscopy has been evaluated in comparison to endoscopy, showing no difference in BE yield, although transnasal intubation requires specialist expertise and tolerability results have been mixed[138, 139]. Breath testing has demonstrated ~80% sensitivity/specificity to BE[140]. Recent work using DNA methylation markers and a swallowable device for tissue sampling achieved >90% sensitivity/specificity to BE[141]. These techniques generally do not identify dysplasia.

Endoscopic optical coherence tomography (OCT) can image tissue microstructure and has shown potential for *in vivo* detection of BE and dysplasia[45]. Commercial balloon-based OCT imaging known as volumetric laser endomicroscopy (VLE) has been used to study *ex vivo* resection specimens[42, 43] and experienced users reported diagnostic performance[46]; larger trials of *in vivo* sensitivity/specificity for dysplasia with laser-guided biopsies are ongoing and have shown promising results[142]. Tethered capsules can be swallowed without sedation, and were initially string-tethered video capsules that showed feasibility for BE screening[88], and later adapted for cross-sectional OCT[94]. These studies demonstrated cross-sectional OCT images, and reported excellent patient toleration[143], but lacked correlation with patients' pathology and endoscopic findings, and used OCT systems with slower imaging speeds that could not generate *en face* images.

Our group has developed ultrahigh-speed OCT technology that uses micromotor scanning devices for endoscopic imaging, which can generate high quality *en face* and cross-sectional views[79, 144]. Previously we evaluated the feasibility of ultrahigh-speed micromotor tethered capsule OCT with *en face* visualization of >20 cm of esophageal length in sedated patients, demonstrating large field-of-view and dysplasia-associated features including irregular mucosal patterns and atypical glands[54]. We now report a case series of unsedated BE patients with and without neoplasia, imaged with ultrahigh-speed OCT tethered capsules. We describe device improvements that improve procedural ease and image acquisition, and analyses of patient toleration and image quality. We report preliminary results of *en face* and cross-sectional OCT features potentially associated with neoplasia.

Materials and Methods

Imaging system and tethered capsule

This work was performed in collaboration with the VA Boston Healthcare System (Dr. Hiroshi Mashimo MD PhD and staff at the Endoscopy Unit), Thorlabs (Dr. Benjamin Potsaid) and Praevium Research (Dr. Vijaysekhar Jayaraman) for use of prototype swept source technology.

OCT was performed using a prototype ultrahigh-speed instrument imaging at 1,000,000 axial scans per second, 20x faster than commercial VLE. The tethered capsules (Figure 1A-B) used micromotors for circumferential imaging at 300 frames/sec[54], and had 30μm transverse resolution. Several improvements were made over previously reported capsule designs for unsedated imaging[143]. The capsule enclosure was largely composed of lubricious medical grade ultrahigh-molecular-weight polyethylene material with a small transparent imaging window, reducing friction and allowing the 12mm diameter capsule to be swallowed or pulled back smoothly within the esophagus. The proximal end of the capsule was designed with a 30° taper, improving pullback smoothness and ease of retrieval. The tether was 2.2mm diameter, providing flexibility for patient comfort while retaining some rigidity for operator control, and marked at 5cm intervals to assess approximate capsule distance from incisors.

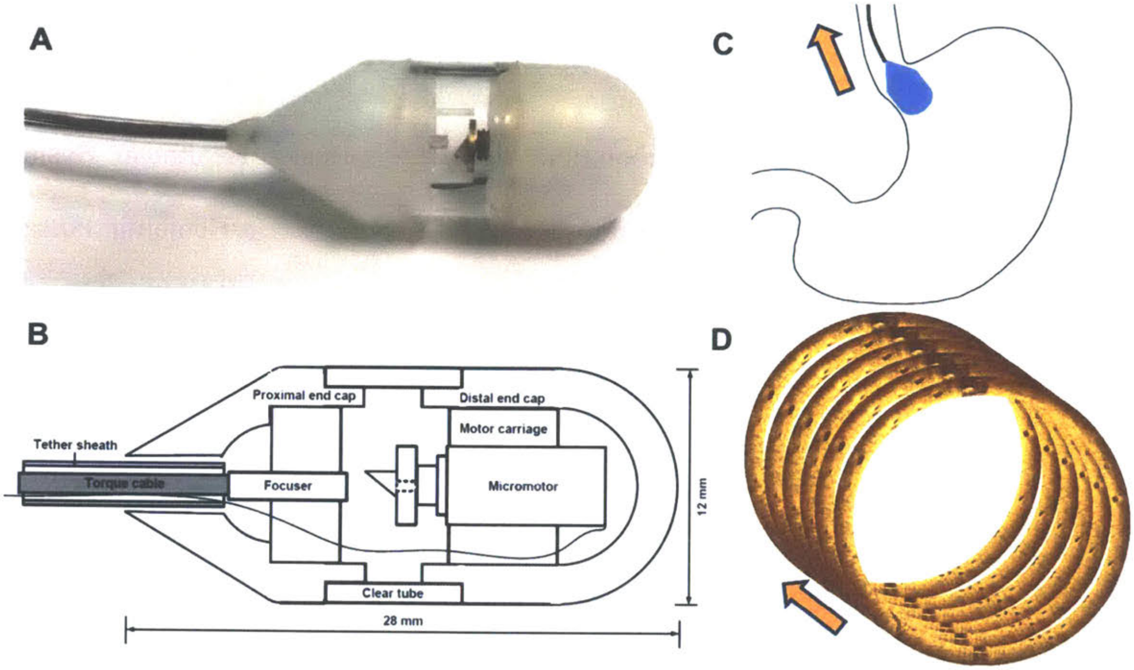

Figure 1. A: Photograph of tethered capsule constructed out of lubricious material and a 30° taper for ease of retrieval. B: Schematic showing micromotor optical scanner and other components. C: Cartoon showing capsule travelling from gastric cardia into distal esophagus during a pullback scan. D: Illustration showing multiple cross-sectional images rapidly acquired in sequence to obtain volumetric and *en face* visualization.

Patient recruitment and imaging procedure

The study was approved by IRBs at the Veterans Affairs Boston Healthcare System, Harvard Medical School, and Massachusetts Institute of Technology. Written informed consent was obtained before enrollment. Patients undergoing BE surveillance or endoscopic treatment for prior diagnosed neoplasia were recruited. Neoplasia was defined to include low-grade dysplasia (LGD), high-grade dysplasia (HGD), and intramucosal carcinoma (IMC). Patients were scheduled for same-day sedated endoscopy, and underwent standard endoscopy preparation.

Unsedated patients swallowed the tethered capsule with sips of water, sitting upright and supervised by the endoscopist manually controlling the tether. The capsule travelled through the gastroesophageal junction (GEJ) to the proximal gastric cardia, guided by real-time cross-sectional OCT visualization, with additional dry/wet swallows to help the capsule's downward travel and open the lower esophageal sphincter (LES). Before the pullback scan, patients were asked to take dry swallows to improve capsule contact with the esophageal wall, and ~10sec was allowed to elapse without swallows to avoid swallow-induced relaxation (deglutitive inhibition) of the LES that normally forms a dilated vestibule[145]. The endoscopist then pulled back the capsule from the GEJ (Figure 1C) at a steady speed of ~1cm/sec for volumetric imaging over ~10sec. Cross-sectional images were acquired at 300 frames/sec to build up a densely sampled volumetric dataset (Figure 1D). After each dataset acquisition, the *en face* OCT images could be previewed for adequate coverage of the GEJ and squamo-columnar junction (SCJ). If esophageal contact on the capsule was suboptimal, additional dry/wet swallows were taken to improve contact before subsequent repeat pullback scans. If initial pullback images showed longitudinal nonuniformity, pullback data acquisitions were repeated immediately after the swallow or after greater period of rest post-swallow to avoid rebound LES contractions.

After completion of imaging, the capsule was retrieved orally by pulling up on the tether. To ease retrieval through the upper esophageal sphincter (UES), patients were asked to perform slow nasal inhalation, which relaxed the UES and minimized gag reflex resulting from stimulating the posterior tongue. Swallowing motions are not effective for capsule retrieval since the relaxation of the UES is transient, and this places the posterior tongue closer to the tether in a position for greater gagging.

Patients then underwent sedated endoscopy ~2-4 hours later, based on the American Society for Gastrointestinal Endoscopy (ASGE) guidelines which require a 2-hour fast after ingestion of clear liquids for safe administration of intravenous sedation[146]. During endoscopy, measurements were obtained of Prague C&M and the diaphragmatic hiatus, and 4-quadrant biopsy for NDBE surveillance or endoscopic treatment for patients with prior diagnosed dysplasia was performed per clinical standard of care.

After each of the imaging procedures (tethered capsule and endoscopy), a research nurse carried out a brief interview with the patient on their anxiety before ("How anxious did you feel before the procedure? 1 not, 5 very") and discomfort during ("How much discomfort did you have during the procedure? 1 none, 5 a lot") each of the procedures, as well as a recommendation score ("Would you recommend the procedure to others?" 1 definitely yes, 5 definitely no). These questions were identical to a previous report[143], to facilitate comparison.

Data analysis

The toleration (anxiety and discomfort) and recommendation scores for each procedure were analyzed. In addition to mean and standard deviation of scores, the toleration score distributions for all patients were plotted by pathology and treatment status subgroups, to show any possible associations of toleration with prior endoscopy and/or treatment experience. Datasets acquired were assessed for image quality, and one optimal dataset from each patient was selected for further analysis. Two quality metrics were analyzed: tissue contact of the capsule on the esophagus, and longitudinal (pullback) image uniformity. The *en face* OCT image at ~100um distance/depth from the capsule surface was assessed for non-contact areas. The fraction of tissue contact area over the BE segment was estimated. Squamous mucosa regions proximal to the squamo-columnar junction (SCJ) maximal extent were excluded from the tissue contact analysis, because these areas usually showed good contact but were less relevant to BE. Longitudinally stretched areas due to slowing of the capsule relative to the esophageal wall during pullback were manually marked as image non-uniformity, which generated a percentage of longitudinal uniformity per dataset. Tissue contact and longitudinal image uniformity were plotted by short/long-segment BE (<=3cm and >3cm), and absence/presence of sliding hiatal hernia (distance of diaphragmatic hiatus from gastric folds <=2cm and >2cm) subgroups.

The datasets were assessed by an expert OCT reader (KCL) for features found within the BE segment that were potentially associated with dysplasia. The reader was unblinded to patient history and endoscopic findings, so as to be attentive to any distinctive data features/traits associated with clinical characteristics. Two features were studied– atypical gland clusters and irregular mucosal patterns. Atypical gland clusters were defined as regions of clustered atypical glands, including non-elliptical shape, branching or internal debris, with a density of >5 atypical glands over a 5mm square (25mm^2) *en face* area. Adjacent areas each with >5 atypical glands were grouped as a single clustered region. The *en face* area/density criteria were added to previously reported cross-sectional criteria for atypical glands[42], to define clustering in the cross-sectional and/or *en face* plane, and to impose higher severity than atypical glands distributed over larger areas. Atypical gland clusters were assessed using simultaneous viewing of *en face* and cross-sectional image series. Irregular mucosal patterns were defined as regions of *en face* mucosal irregularity using narrowband imaging (NBI) criteria[26] including distortion/absence of mucosal patterns. To optimize mucosal pattern visibility, the *en face* image series was averaged over ~1 mm depth to generate a single *en face* image with improved image contrast, which was then used to assess mucosal patterns. The two features were assessed separately and outlined in the *en face* plane. The features were then independently counted for their absolute occurrence rate (occurrences/patient), the per-area occurrence rate (occurrences/approximate area of tissue in contact) and occurrence rate of the two features overlapping, i.e. a region of irregular mucosal pattern with an underlying atypical gland cluster. Features occurring near (within 1cm of) the GEJ on the BE side were noted.

Results

Patient demographics and clinical characteristics

16 patients were enrolled. Demographics and characteristics including baseline pathology (neoplasia status) at time of imaging, treatment history, and BE length are summarized in Table 1. In all but one patient, the tethered capsule procedure was followed by an esophagogastroduodenoscopy (EGD). This one patient was scheduled to receive an unrelated colonoscopy, but was recruited to the study due to his known ongoing surveillance for long-segment BE, including a recent EGD in the previous year. This patient was not asked to provide toleration scores for his colonoscopy.

Age, mean (± SD)	68 (7)
Sex, male, no. (%)	16 (100)
Race, white, no. (%)	16 (100)
Baseline pathology and treatment status	
NDBE subjects, no. (%)	9 (56)
Short-segment (<=3cm) Barrett's Esophagus (BE), no. (%)	2 (13)
LGD subjects, no. (%)	4 (25)
Ablative treatment-naïve subjects, no. (%)	1 (6)
Short-segment BE, no. (%)	1 (6)
Treated subjects, no. (%)	3 (19)
Residual short-segment BE, no. (%)	3* (19)
HGD/IMC subjects, no. (%)	3 (19)
Ablative treatment-naïve subjects, no. (%)	2[†] (13)
Short-segment BE, no. (%)	1 (6)
Treated subjects, no. (%)	1 (6)
Residual short-segment BE, no. (%)	1 (6)
Length of BE at study endoscopy, cm	
Circumferential extent, mean (± SD)	3.6 (4.3)
Maximal extent, mean (± SD)	5.1 (4.5)
Short-segment (<=3cm) subjects, no. (%)	8 (50)
Long-segment (>3cm) subjects, no. (%)	8 (50)
Distance from diaphragmatic hiatus (D) to gastric folds (G), mean (± SD)	2.3 (2.5)
Subjects with sliding hiatal hernia (D-G >2cm), no. (%)	5 (31)
Length of hiatal hernia, mean (± SD)	5.6 (2.1)

*One treated LGD patient had no visible BE on endoscopy and was classified as short-segment BE.

[†] One HGD/IMC patient had prior EMR and no ablation, thus classified as ablative treatment-naive.

Table 1. Patient demographics and clinical characteristics (n=16)

Patient toleration and recommendation scores

The procedure time was 9.7±3.0 minutes. For the unsedated capsule procedure (n=16), pre-procedure anxiety was 1.9±1.0, procedural discomfort was 2.5±1.1, and recommendation score was 1.3±0.7. For the sedated endoscopy procedure (n=15), pre-procedure anxiety was 1.3±0.7, procedural discomfort was 1.6±0.9, and recommendation score was 1.1±0.3. The toleration score distributions, grouped by patients' pathology and treatment history are presented in Figure 2.

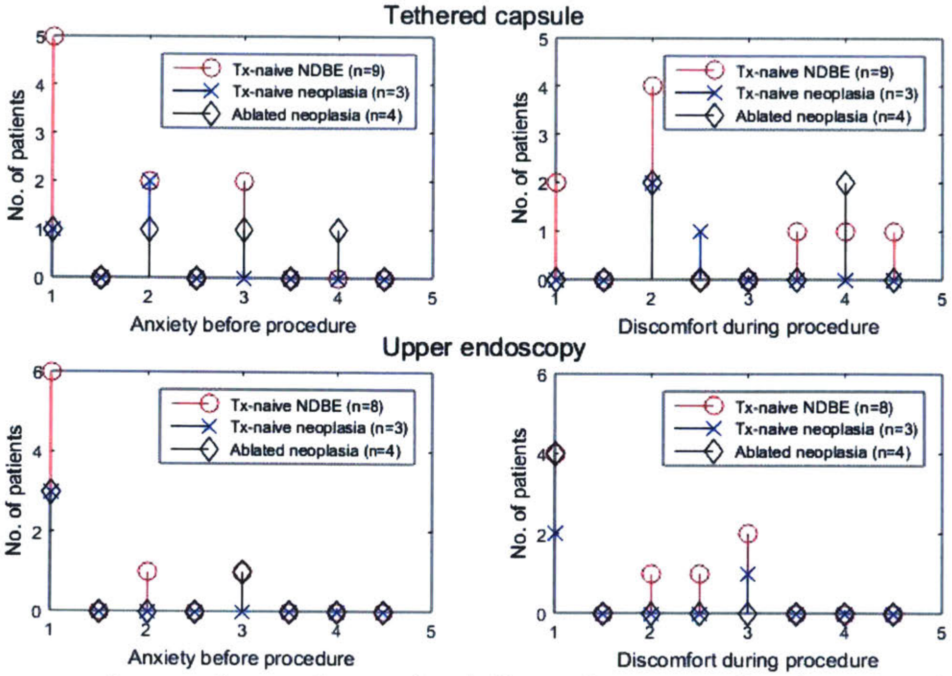

Figure 2. Pre-procedure anxiety and procedural discomfort scores for the tethered capsule and endoscopy procedures. 1- no anxiety/discomfort, 5- high anxiety/discomfort. Scores between patient subgroups of baseline pathology and treatment history were similar.

Tissue contact and longitudinal uniformity

The number of pullback datasets per patient was 5.5 ± 1.3, from which an optimal dataset was selected. Out of 16 patients, the fraction of tissue contact area over the BE segment was 75±27%. Tissue contact was observed to be associated with BE length and sliding hiatal hernia. Tissue contact was 89±11% for short segment BE with/without prior ablative treatment (n=8) patients, and 61±31% for long segment BE (n=8) (p=0.03). Tissue contact was 84±15% in patients without a sliding hiatal hernia (n=11), and 55±37% with hernia (n=5) (p=0.04).

Longitudinal image uniformity was observed in 59±34% of the BE segment. Longitudinal uniformity was 45±43% for short segment BE, and 72±14% for long segment BE (p=0.11).

Longitudinal uniformity without sliding hiatal hernia was 61±36%, and with hernia 54±31% (p=0.7). The spread of these measurements are presented in Figure 3.

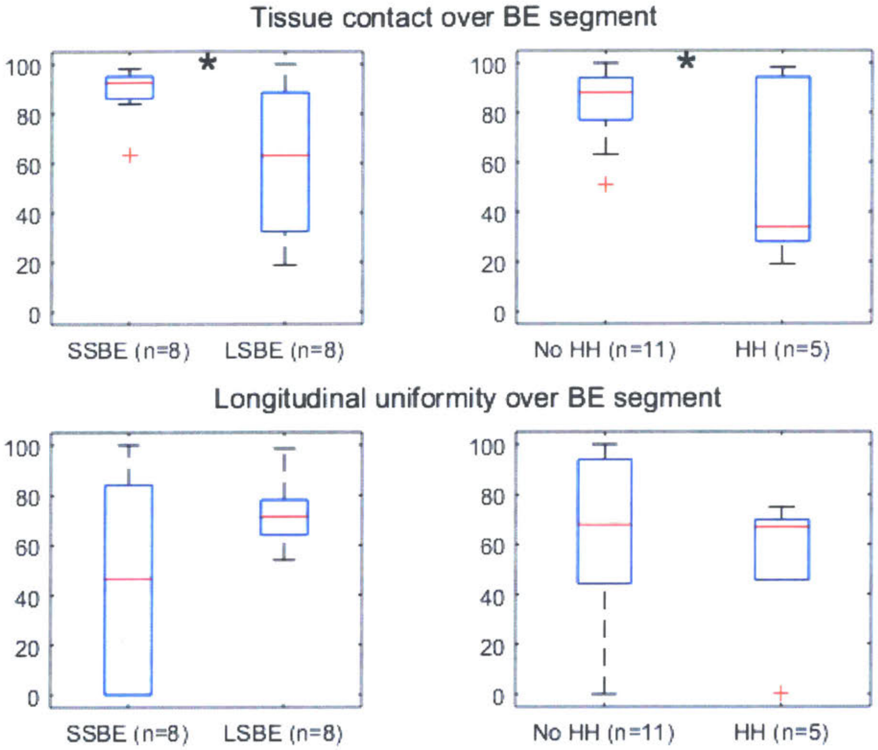

Figure 3. Boxplots of tissue contact and longitudinal uniformity for the tethered capsule OCT datasets. Tissue contact and longitudinal uniformity showed opposite associations with BE segment length. Tissue contact was significantly different between short/long segment BE (p=0.03) and absence/presence of sliding hiatal hernia (p=0.04).

Non-contact areas were generally consistent between repeated pullback datasets (Fig. 4), suggesting that contact was largely dependent on anatomy and physiology, rather than transient phenomena.

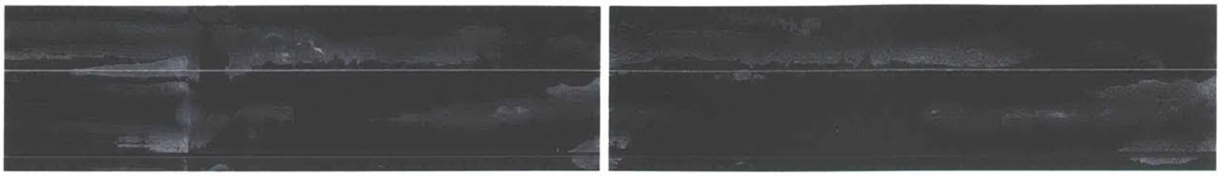

Fig. 4. Two consecutive pullbacks from a long-segment BE patient showing that non-contact areas were relatively comparable in location.

OCT features associated with patient history

Example OCT images are presented. Figure 5 shows results from a treatment-naïve patient with prior histological diagnosis for low-grade dysplasia referred for treatment. Imaging was performed prior to endoscopy. The imaging area (Figure 5A) was 4cm (circumference of capsule) x ~9cm (approximate pullback length). Atypical gland clusters (Figure 5B-C) were observed. In the contrast-enhanced *en face* OCT image (Figure 5D), regions of regular mucosal patterns (Figure 5G), irregular mucosal patterns (Figure 5E-F), and absence of pattern (also irregular) (Figure 5H) were observed. Some regions of irregular mucosal patterns had underlying atypical gland clusters. Cross-sectional images also showed atypical glands (Figure 5I-J), and surface signal higher than subsurface (Figure 5K), and normal columnar epithelium (Figure 5L).

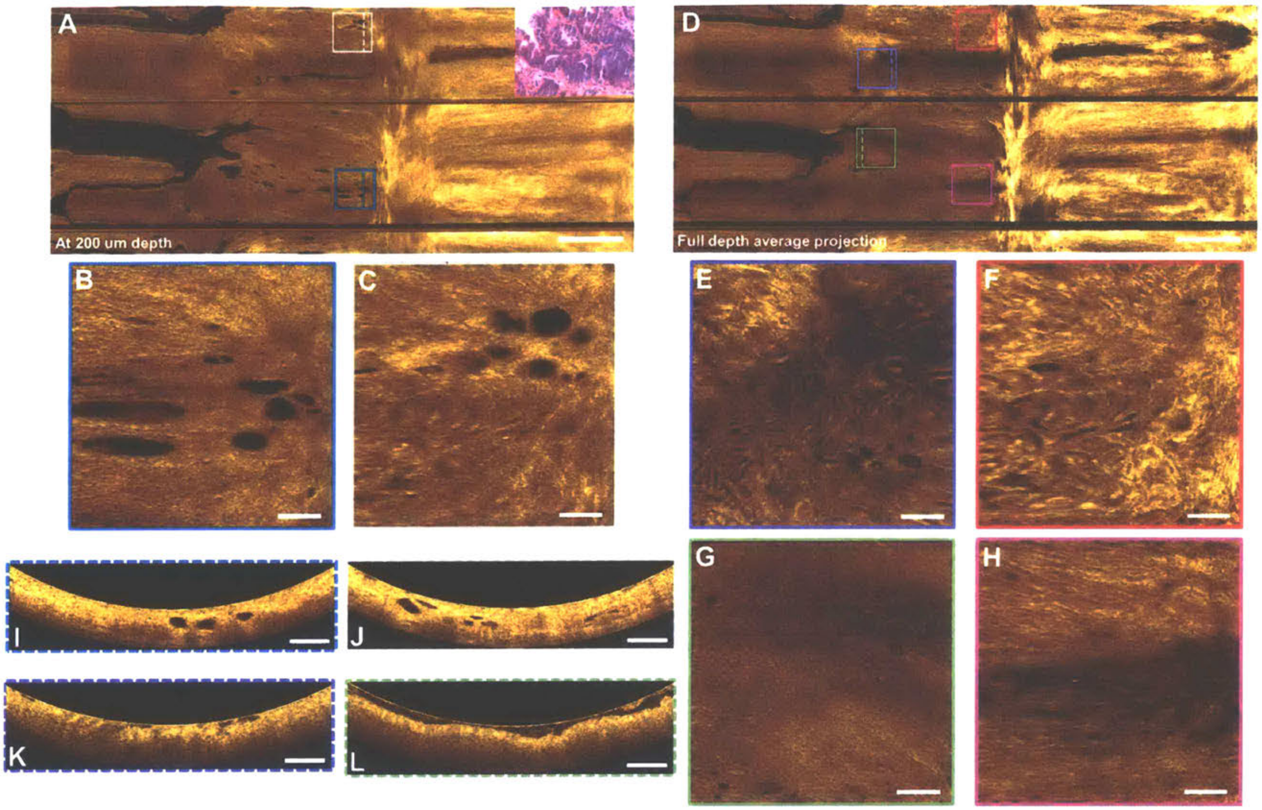

Figure 5. Tethered capsule image volume from patient with C0.5M2 and treatment-naïve low-grade (basal crypt) dysplasia with biopsy (inset) from previous EGD. *En face* OCT image (A) at 200 um depth from surface, averaged over 80 um depth, showing dilated glands and (D) averaged over ~1 mm depth (full projection) for contrast enhancement to show mucosal pattern. Scale bar 1 cm. (B, C) Atypical gland clusters. (E, F) Irregular mucosal pattern. (G) Regular mucosal pattern. (H) Absence of mucosal pattern, noted to be irregular. (I-L) Cross-sectional images co-registered to *en face* regions of interest. (I) shows 3 dilated glands of atypical shape, but does not convey the substantial clustering of >5 glands that is observed in *en face*. (K) shows surface signal higher than subsurface but does not convey the *en face* irregularity. (L) shows loose contact at the gastroesophageal junction, which may confound differentiation between gastric and BE tissue. All other scale bars 1 mm.

Another patient (Figure 6) did not receive same-day EGD, but had known long-segment NDBE from two EGDs 9 months prior and 4 years prior. A high density of glands was observed over the entire segment, and an exceptionally high number of atypical gland clusters was observed at the GEJ on the gastric side. This example showed well-defined boundaries of the gastroesophageal junction (GEJ) and squamocolumnar junction (SCJ). The GEJ boundary is typically less well-defined. This example is instructive in illustrating that notable OCT features may occur frequently at the GEJ, even in low-risk NDBE patients.

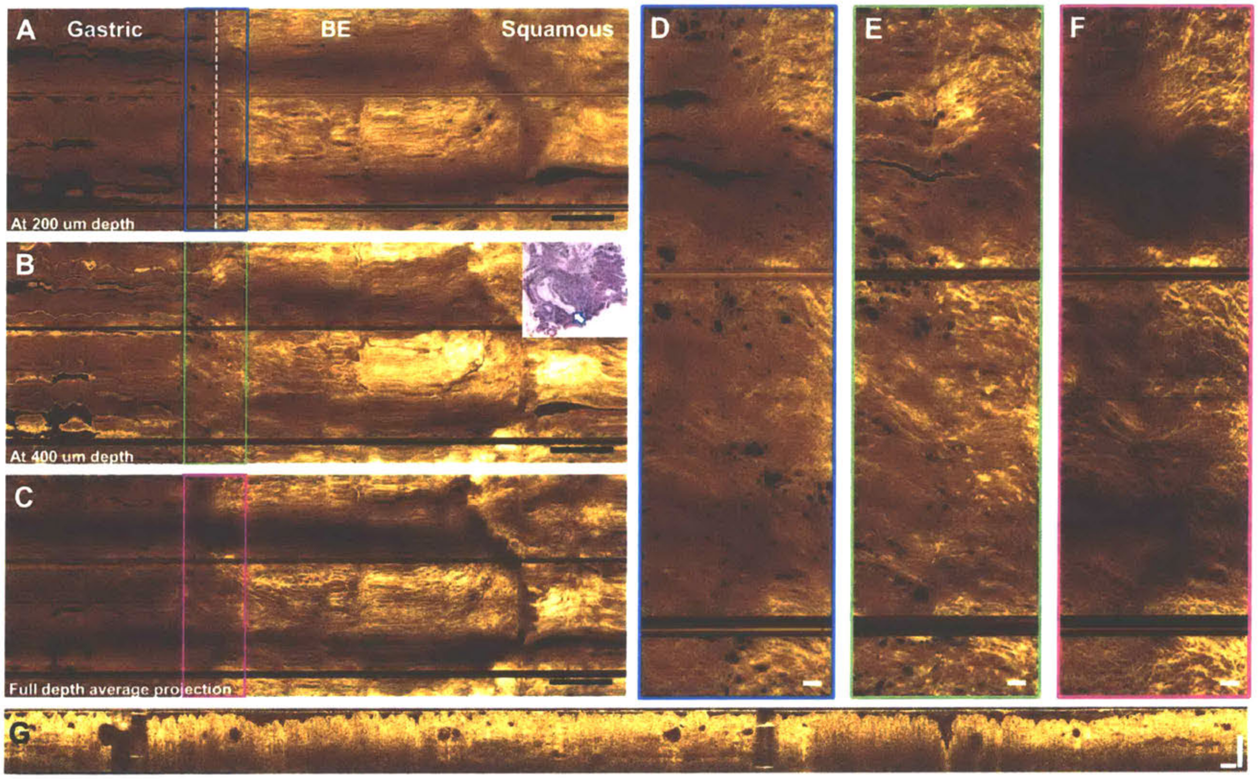

Figure 6. Tethered capsule image volume from patient with C2M4 non-dysplastic BE at (A) 200 μm depth, (B) 400 μm depth, and (C) full depth projection. Scale bars 1 cm. (D-F) Enlargements showing glands and mucosal pattern at the GEJ. Scale bars 1 mm. (G) Cross-sectional OCT from the GEJ showing atypical glands. Scale bar 500 um. Two recent surveillance EGDs with 4-

quadrant biopsies found no dysplasia. Numerous atypical gland clusters at various tissue depths were observed near the GEJ on the gastric side, and were not accompanied by any notable mucosal irregularity. These features at the GEJ can confound attempts to identify neoplasia, particularly if the GEJ boundary is poorly defined and wide field *en face* views are unavailable. Biopsy from last EGD 9 months prior at the GEJ (inset) shows large dilated cardiac gland (arrow) with smaller peripheral glands.

Table 2 and Figure 7 show a summary of features observed in patient subgroups (NDBE vs history of dysplasia and treatment). The occurrence rates of irregular mucosal patterns, atypical gland clusters, and overlapping features, on a per-patient and per-area basis are reported. In the neoplasia group, irregular mucosal patterns with underlying atypical gland clusters had 1.7 occurrences/patient and 0.36 occurrences/area, while in the NDBE group had 0.22 occurrences/patient and 0.01 occurrences/area, suggesting strong association with patient neoplasia status. Two patients in the NDBE group each had a single occurrence of irregular mucosal pattern with underlying atypical gland cluster; standard 4-quadrant biopsies obtained during the subsequent EGD from the longitudinal position closest to the observed features showed low-grade dysplasia and indefinite for dysplasia respectively.

OCT features in patient subgroups	All neoplasia (n=7)	Treatment-naïve neoplasia (n=3)	Ablated neoplasia (n=4)†	NDBE (n=9)
Irregular mucosal patterns (all)				
No. of patients	6/7	3/3	3/4	6/9
Occurrences	17 (2.4/patient)	11 (3.7/patient)	6 (1.5/patient)	10 (1.1/patient)
Occurrences <1cm from GEJ	14 (2.0/patient)	9 (3.0/patient)	5 (1.3/patient)	3 (0.33/patient)
Occurrences per cm^2 area*	0.56	0.40	0.72	0.06
Irregular mucosal patterns w/ atypical gland clusters				
No. of patients	5/7	3/3	2/4	2/9
Occurrences	12 (1.7/patient)	9 (3.0/patient)	3 (0.75/patient)	2 (0.22/patient)
Occurrences <1cm from GEJ	9 (1.3/patient)	7 (2.3/patient)	2 (0.5/patient)	0 (0/patient)
Occurrences per cm^2 area	0.36	0.31	0.40	0.008
Atypical gland clusters (all)				
No. of patients	7/7	3/3	4/4	7/9
Occurrences	21 (3.0/patient)	11 (3.7/patient)	10 (2.5/patient)	12 (1.3/patient)
Occurrences <1cm from GEJ	15 (2.1/patient)	7 (2.3/patient)	8 (2.0/patient)	6 (0.67/patient)
Occurrences per cm^2 area	0.60	0.40	0.81	0.30

*Mean of occurrences/area for each patient, where total area per patient is approximated by BE maximal extent × capsule circumference × fraction of BE area in contact.

†One patient out of 4 had no visible BE on endoscopy, and was thus excluded from the mean occurrences/area computation. Features observed at the GEJ were counted as occurrences.

Table 2. Occurrence rates of OCT features in BE, namely irregular mucosal patterns and atypical gland clusters, in patient subgroups of baseline pathology and treatment history.

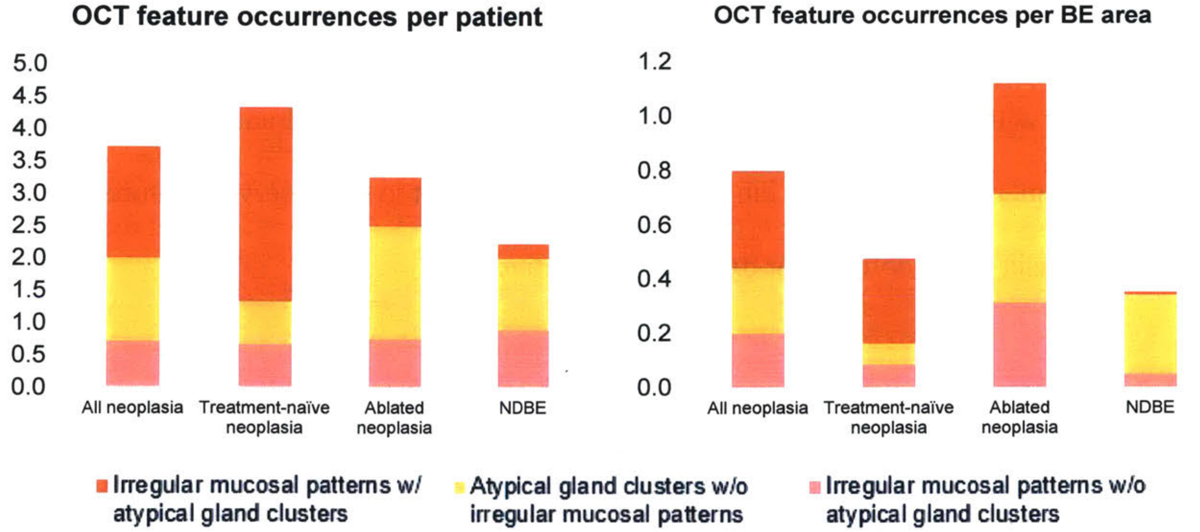

Figure 7. Stacked bar charts of OCT feature occurrences per patient and per cm^2 of BE area. The features are plotted to avoid repeat counting, such that the stacked height indicates the total feature

count. Neoplasia patients showed a high occurrence rate of irregular mucosal patterns with underlying atypical gland clusters, while NDBE patients showed a much lower occurrence rate. Atypical gland clusters were numerous in all subgroups, and associated with a proximity to the GEJ (Table 2).

Discussion

We report our initial experience with tethered capsules using ultrahigh speed OCT imaging technology for wide field, *en face* and cross-sectional visualization. We used OCT imaging speeds of 1,000,000 A-scans/sec and micromotor rotary scanning at 300 frames/sec to generate high quality *en face* views, enhanced by capsule design improvements for smooth pullback. Previous reports demonstrated screening applications by recruiting largely from a primary care population, who likely had little or no BE. We aimed to investigate feasibility of surveillance, thus recruited from a heterogeneous BE surveillance population, in which patients had various BE lengths, baseline pathology and treatment history.

Toleration (anxiety and discomfort) scores stratified by pathology and treatment history were generally consistent between subgroups, suggesting that toleration may be independent of experience with prior endoscopies and treatment. The endoscopic procedure was better tolerated than the tethered capsule, due to sedation use. Our toleration scores show marginally lower pre-procedure anxiety (1.9±1.1 vs 2.1±0.8) and higher procedural discomfort (2.5±1.0 vs 1.9±0.9) than a previous report[143], possibly due to our larger capsule diameter (12mm vs 11mm) chosen for better tissue contact. These results suggest that tethered capsule OCT is a moderately well-tolerated procedure, although both were single-center studies, and our study was at the VA with all enrolled subjects veterans and male, so results may not be generalizable to the broader population.

Close contact of the capsule with the esophageal wall is critical for optimal visualization with OCT, because it assures that most of the esophagus circumference is visualized and within the focal range of the imaging optics. Loose contact on the esophagus may affect the appearance of mucosal microstructure on OCT, and implies the presence of esophageal folds, which obscure portions of the esophagus. Primary peristalsis is initiated by swallow, which soon triggers a relaxation (deglutitive inhibition) at the LES. In the ensuing ~10 sec, the peristaltic wave travels rapidly down the esophagus, and upon reaching the LES causes it to close shut. Therefore, waiting ~10 sec after the last swallow avoids any vestibular dilation of the distal esophagus due to LES relaxation. Previous studies suggested that peristaltic contractions initiated by swallowing would ensure close contact between the capsule and the esophagus. In our experience, patient swallows were helpful, but a substantial minority of patients persistently showed poor contact on the capsule despite repeated dry/wet swallows and avoiding deglutitive inhibition. The short-segment cases (n=8) showed superior tissue contact compared to the long-segment cases (n=8) (89±11% vs 61±31%, p=0.03) (Figure 3). Patients without sliding hiatal hernia (n=11) showed superior contact compared to those with hernia (n=5) (84±15% vs 55±37%, p=0.04). Previous studies did not report difficulties with obtaining close contact of the esophagus on the capsule, but had likely recruited patients with little or no BE. Early studies of esophageal motility in BE found an association between long BE lengths and reduction of LES tone and peristaltic amplitude[147]. The reduced LES tone associated with sliding hiatal hernia[145] may also contribute to poor tissue contact.

Longitudinal pullback uniformity is necessary for high quality *en face* visualization. Our previously reported micromotor imaging probe[79] relied on 2mm/sec motorized pullback for *en face* OCT. For simplicity, our tethered capsule was longitudinally translated by manual pullback at 1cm/sec. Our previous tethered capsule study in sedated patients[54] found that the capsule could not be translated smoothly at slow speeds, which produced longitudinal image artifacts. Friction between the capsule surface and esophageal wall contribute to non-uniform motion. In our design, the lubricious housing improved pullback uniformity. The operator pulled back on the tether at a fast ~1cm/sec, minimizing frictional effects. During pullback, the operator occasionally reported sensing resistance on the tether possibly exerted by a combination of anatomic variations, peristaltic contractions, LES tone and/or rebound contractions, leading to nonuniform pullback. We did not forcefully pull through these resistances, which are meaningful anatomical signals for safe and effective use. Short-segment BE had inferior longitudinal uniformity to long-segment BE. The good tissue contact produced by strong LES tone might have resulted in nonuniform capsule pullback. Conversely, long-segment BE has looser contact, which may be enabling smoother pullback. Information on BE length and hiatal hernia from prior endoscopy, or pressure measurements from manometry, if available, may help determine suitability for tethered capsule imaging.

The occurrence rates of irregular mucosal patterns and atypical gland clusters identified in this case series showed associations of these features with patients' neoplasia status and treatment history. The neoplasia subgroup showed a much higher occurrence rate of irregular mucosal patterns with underlying atypical gland clusters than NDBE (1.7/patient and 0.36/area versus

0.22/patient and 0.01/area). The two patients in the NDBE subgroup that showed this combined feature were found in subsequent EGD biopsies to have low-grade and indefinite for dysplasia diagnoses from the approximate longitudinal position of the OCT features. Atypical gland clustering may occur in either plane, but transverse clustering cannot be easily discerned in the cross-sectional plane alone. Earlier cross-sectional OCT criteria were developed in part using VLE, which had slow imaging speeds that generated sparsely-spaced cross-sectional image volumes without *en face* views. The present study shows effective gland visualization in either cross-sectional or subsurface *en face* planes, the latter enabling more comprehensive evaluation. Atypical glands are known to be associated with neoplasia, but also occur in NDBE cases, leading to suboptimal specificity in some studies[43]. The present study showed atypical gland cluster occurrence rates of 3.0/patient and 0.60/area in neoplasia versus lower but still substantial rates of 1.3/patient and 0.30/area in NDBE. A multi-center study of NBI criteria for dysplasia based partly on irregular mucosal pattern showed 80% sensitivity and 88% specificity[26]. The augmentation of OCT atypical gland criteria with *en face* irregular mucosal pattern may improve the differentiation of neoplasia and NDBE subgroups using OCT.

A substantial fraction of features in all subgroups occurred near the GEJ, which has been reported in the past as an area where OCT features may have low specificity[148]. The region of cardiac mucosa at the GEJ is the subject of ongoing debate, and it has been proposed that GEJ glands may progress to BE and have pre-malignant potential[7]. The large field-of-view and *en face* visualization with the tethered capsule may improve assessment of the GEJ boundary (Figure 5) compared to slower cross-sectional OCT systems, and facilitate the study of the pathogenesis of BE and dysplasia originating from GEJ features. Treated patients appeared to show higher rates of features, but these patients had short residual BE lengths after prior treatment; therefore the majority of features were near the GEJ leading to high density of feature occurrences over a small area.

An important limitation of the study was the lack of histological correlation with the observed OCT features. Our device did not have the capability to obtain biopsy or mark regions for biopsy during endoscopy. In the present study, the feature analysis was based on descriptions from prior NBI and volumetric *en face* and cross-sectional OCT studies that reported histologically correlated features. Early success of laser marking using tethered capsules based on cross-sectional image guidance have been reported[110]. Future work may adapt the laser marking paradigm for tethered capsules to guide biopsy based on both *en face* and cross-sectional features. Alternatively, the follow-up EGD could use NBI to identify regions of irregular mucosal pattern that agree with the *en face* OCT findings for biopsy correlation. With further improvements to data quality and yield, tethered capsule image volumes with optimal tissue contact and longitudinal uniformity would map the BE segment and enable feature localization by clock and longitudinal position, with sufficient accuracy for endoscopic sampling. Another limitation was the use of a single unblinded reader for feature analysis. This was a pilot study with small enrollment, which necessitated the use of an OCT expert to interpret this data while cognizant of patient history. This unblinded study has generated hypotheses that will be tested in a future prospective study using tethered capsule OCT for dysplasia identification.

Ultrahigh-speed tethered capsule OCT can achieve comprehensive visualization of esophageal microstructure in unsedated patients, and may be an effective modality for risk stratification in BE screening, and surveillance for neoplasia. Irregular mucosal patterns with underlying atypical gland clusters were strongly associated in patients with neoplasia, and may be a potential marker of neoplasia. Additional studies with histological correlation are warranted.

Bonus supplement: Prague C&M reading of capsule OCT

The Prague C&M criteria is an endoscopic standard of determining the length and extent of BE. C is the circumferential extent and M is the maximal extent. Determining the Prague measurements in an unsedated procedure may have impact in risk stratification, since it is well established that long-segment BE patients are at higher risk of EAC than short-segment patients.

Datasets were assessed in a blinded reading by 2 readers, an experienced gastroenterologist who performed the capsule imaging and endoscopies at least 2 months before the reading, and an OCT student trainee with only minimal previous exposure to endoscopic OCT images. Each dataset was presented by the reading facilitator (KCL) as a 3-dimensional image stack, with simultaneous ('orthoplane') scrollable views of en face and cross-sectional planes, as well as a single en face image generated by an average 'projection' of an en face image stack of 800 um depth from the capsule surface. The former provided depth-resolved visualization, while the latter provided a contrast-enhanced image of surface mucosal pattern. Readers were first given a brief training session introducing image examples from a range of tissue types including squamous epithelium, BE, and gastric mucosa, as well as the reading protocol. The maximal location of BE was defined as the most distal location at which 100% of the cross section showed squamous epithelium. The circumferential location of BE was defined as the most proximal location at which 0% of the cross section showed squamous epithelium. The gastroesophageal junction (GEJ) location was defined as the location at which about 50% of the cross section showed OCT features of gastric mucosa. The training included practice assessment of one dataset. Training was followed by a pretest assessment of another dataset, and a discussion with the facilitator. The remaining 12 datasets were then read in blinded fashion. The location of the maximal extent, circumferential extent, and GEJ identified by the reader were noted by the facilitator.

Out of 14 datasets assessed, 1 dataset was used for training and 1 for pretest, and 12 datasets were read. A minority of cases had <60% tissue contact (n=4) but were also included in the reading for completeness, but were not expected to yield viable measurements. All measurements were rounded to the nearest 0.5 cm similar to endoscopic measurements. Reader 1 (HM) had M mean absolute error 1.7±1.3 cm, and C 1.3±1.1 cm. Reader 2 (EM) had M mean absolute error 2.4±1.4 cm, C 2.0±1.1 cm. An early study validating the endoscopic Prague criteria[149] found good agreement within 2 cm between readers, therefore the OCT readings appear consistent. However, it is important to plot the actual readings versus true measurements on a scatter plot to observe trends and distributions.

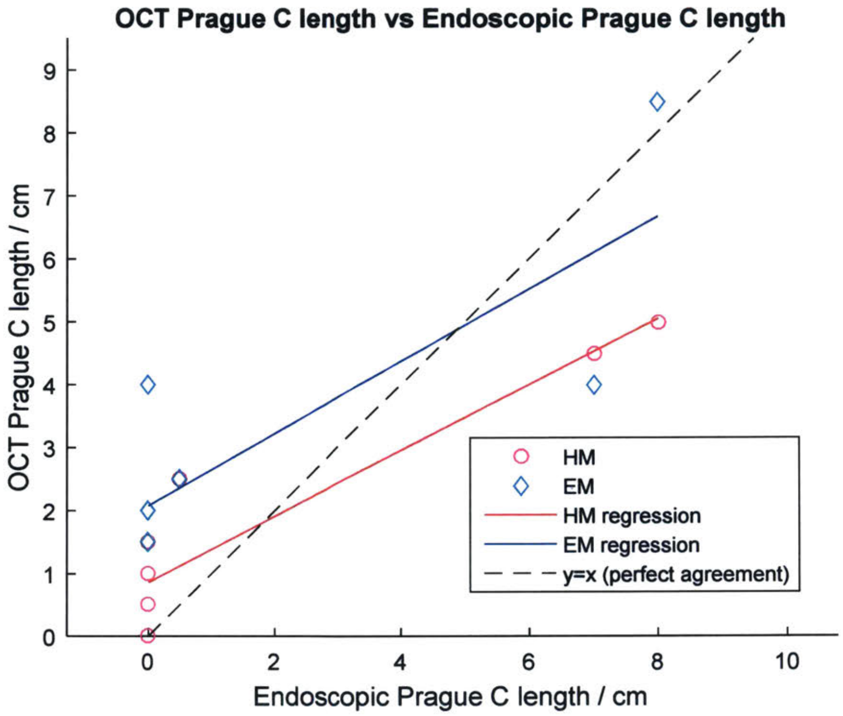

Fig. 7. Scatter plot of OCT Prague reading of circumferential (C) extent versus endoscopic length.

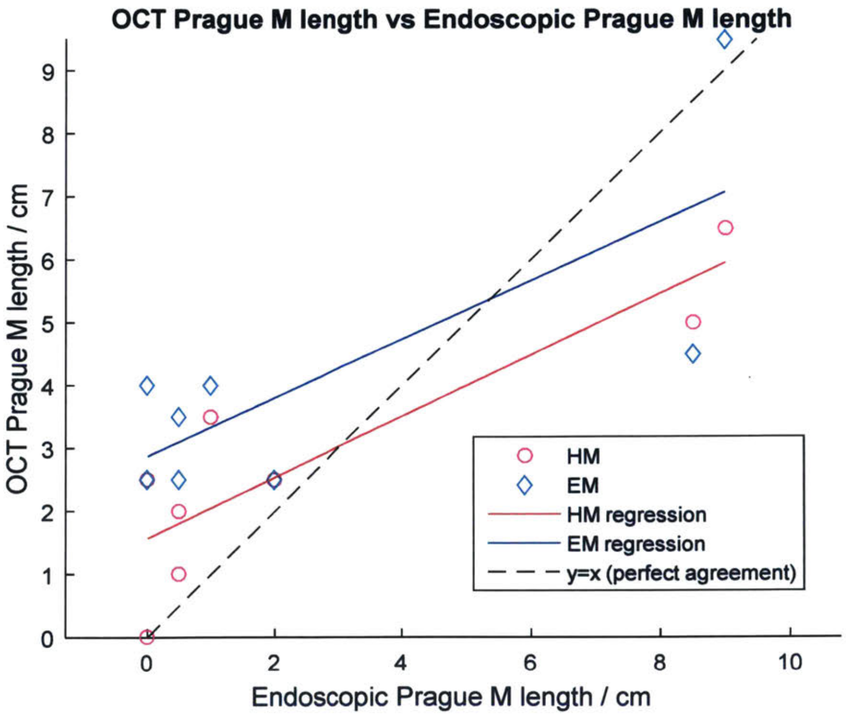

Fig. 8. Scatter plot of OCT Prague reading of maximal (M) extent versus endoscopic length.

It can be observed that the short-segment BE lengths are consistently overestimated, by as much as 2 -3 cm, while the long-segment BE lengths are underestimated. Short-segment BE is known to be low risk, so an overestimate of length may lead to an overestimate of risk, and vice versa. This points to an area of potential improvement in the reading criteria. It will be possible to modify the criteria for the GEJ to start at the longitudinal location that contains 0% gastric tissue (excluding the tissue transition zone), which will shorten the lengths overall by 1-2 cm. This will however lead to a further underestimation of long-segment BE. It is possible that a number of the long-segment BE cases did not show comprehensive coverage of the GEJ, due to difficulty in assessing the transition zone (longer in long-segment BE) in real-time, and suboptimal tissue contact leading to erroneously determining the start of the pullback during data acquisition. Also, longer lengths, being acquired over a longer time and length, are more likely to be subject to longitudinal non-uniform artifacts. However, from Fig. 3 it is apparent that short segment BE may be more prone to longitudinal stretching, which will lead to length overestimation. It is also evident from the scatter plots that cases with BE lengths of ~4-6 cm are missing from the data. It is likely necessary to demonstrate reading of a comprehensive spread of BE lengths for study completeness.

The ability to assess Prague criteria without endoscopy is attractive, but may not be realistically achievable if difficulties with tissue contact and longitudinal uniformity persist, because those factors limit coverage and the accuracy of the visualization particularly over long-segment BE. A possible compromise would be simply the reading of absence/presence of BE, however this can be performed with a wide range of technologies that may be lower cost and simpler than OCT. Using OCT features to identify potential dysplasia may be a more important application.

Chapter 7

Conclusion and Future Work

This thesis work presents the development of a broad suite of endoscopic optical imaging technologies, and their *in vivo* demonstration and validation in living swine models and human patients. The modality of choice was optical coherence tomography (OCT), which has known longstanding advantages for *in vivo* gastrointestinal imaging, and recent dramatic advances in imaging speeds have necessitated parallel developments in scanning speed and precision of catheter-based imaging devices. The author has benefited tremendously from early work by colleagues in developing ultrahigh-speed OCT, especially Benjamin Potsaid PhD, Tsung-Han Tsai PhD, Hsiang-Chieh Lee PhD, Osman Ahsen PhD, and other illustrious alumni too numerous to name. The scan speeds enabled by resonant scanning techniques are particularly scalable, reaching into the 10-20 kHz range, finding their match only in the latest advances in multi-MHz OCT speeds. Indeed, these technologies are generalizable to any optical beam scanning technique, and may find even stronger applications with other microscopic modalities. On the clinical front, the emerging practice of unsedated gastrointestinal imaging shows great promise, validated in part by this thesis work and other groups, and could have far reaching applications beyond Barrett's esophagus for the screening of various esophageal and anorectal disorders, bringing low-cost early detection modalities to at-risk groups.

The first portion of the thesis continues efforts from the author's master thesis work on resonant fiber spiral scanning for forward viewing endomicroscopy. Resonant fiber scanning is a classic, even dated technique from the early 2000s, and has been investigated by countless groups since then. However, the complexity of the technique meant that few groups found sustained success, and OCT lagged behind other white-light and nonlinear microscopy techniques due to limited imaging speeds a decade ago. Recent advances in OCT speeds motivated a triumphant return to the resonant fiber scanner, which performed poorly at slow speeds but really flourished in the kHz range. The thesis work has developed compact device packaging, scan calibration, reconstruction and display methods, and clinical use protocols for forward viewing inspection during endoscopy. The main challenge was in producing large resonant scan amplitudes while keeping voltages to a safe minimum and the rigid length of the device as short as possible. This challenge was solved in part by building extremely high quality factor resonant scanners for large amplitude responses, but difficulties with controlling the scan linearity and reset (decay) phase suggest that Q-factors will require more careful control. More compact (<1 mm diameter) piezoelectric tubes capable of high amplitude deflection, relaxing requirements on Q-factor, will be critically important for the continued evolution of this device for ease of clinical translation.

The thesis also reports a new scanning technique that the author and colleagues have named cycloid scanning. This work was developed in close collaboration with postdoc Zhao Wang PhD, who shares co-first authorship with the thesis author on the publication. This technique was intended in part to address difficulties with amplitude modulation of the resonant fiber scanner, particularly on the reset phase. Using a micromotor for the slow axis scan, the resonant fiber can scan continuously at full amplitude and does not require complex control. Rapid multi-volume/sec imaging is enabled by the micromotor rotation. The cycloid is the side-viewing analog to the forward viewing spiral; both techniques use distal actuation mechanisms to cover 2-D areas and do not require external (proximal) actuations. This was a highly novel effort encompassing the theoretical development of the scan trajectory, device design and assembly, image calibration and reconstruction, and translation to human imaging. While results were compelling and likely of great interest to the research community, the most appropriate applications of this technique remain unclear. The cycloid scan has an inefficient non-raster trajectory. For high speed, wide field coverage, standard raster-like scan mechanisms using distal micromotor rotary scanning and rapid pullback are likely to remain ideal. Other imaging modalities such as nonlinear microscopy or confocal microscopy might lend themselves better to cycloid scanning, using data rates of tens of MHz, but the lack of depth information and the extreme alignment precision needed of high numerical aperture imaging may prove challenging for optical assembly and real-world use. Specific applications that require high volumetric rate imaging, say in scenarios that suffer from bulk motion artifacts such as surgical/handheld applications or in regions near the heart such as the gastroesophageal junction, may be most suited to the cycloid technique, which may be used for rapid imaging that freezes motion.

A substantial portion of the thesis has been dedicated to engineering development and clinical investigations of tethered capsules, which have recently enabled a new paradigm of unsedated esophageal imaging. Previous work with tethered capsules involved relatively low technology, including tying strings to capsules, and slow OCT imaging speeds only capable of cross-sectional imaging, but were lauded as an effective technique for rapid yet thorough inspection of the distal esophagus without use of expensive and labor-intensive sedation anesthesia. The author has endeavored to extend the imaging capabilities of tethered capsules to potentially improve diagnostic capabilities. The implementation of micromotors for rapid and precise rotary scanning, and the evaluation of pneumatic actuation, then piezoelectric actuation to provide a second axis scan is motivated by the necessity for high speed and high precision scanning compatible with high speed image acquisition. Also, important has been the development and validation of large animal models and clinical use protocols. The swine is an important model for evaluating large endoscopic devices. Early capsules developed in this thesis were tested in swine esophagus and rectum, which helped to inform clinical protocols later. Initially the capsules were used in sedated patients during endoscopy, but tissue contact on the esophagus was suboptimal and it was unclear if this was superior to existing commercial OCT balloons already capable of imaging large areas in sedated patients. Later, clinical imaging protocols and procedures were devised and iterated for effective tethered capsule imaging of patients without sedation. While results in this thesis suggest that imaging of Barrett's Esophagus using tethered capsules may have diagnostic potential in early detection and screening/surveillance applications, there are substantial opportunities for use in other esophageal pathologies, and numerous other areas of the GI tract that can be accessed by tethered capsules. Screening for squamous cell carcinoma in the esophagus, anal neoplasia and cancer, or rectal polyps as a surrogate for colorectal screening are all worthy of investigation for possible use of tethered capsule imaging. The promise of low cost and simple, non-endoscopic GI imaging using tethered capsules could have enormous impact on population wide screening and early cancer detection.

As OCT technologies continue to make prodigious gains in speed and imaging sensitivity, endoscopic imaging tools must keep up in scanning speed and precision while maintaining compactness and ergonomic ease. It is the author's hope that this thesis work has made a notable contribution in enabling the translation of advanced optical modalities towards not only GI and endoscopy but a wide scope of minimally invasive clinical applications.

Bibliography

1. C. L. Booth and K. S. Thompson, "Barrett's esophagus: A review of diagnostic criteria, clinical surveillance practices and new developments," Journal of Gastrointestinal Oncology **3**, 232-242 (2012).
2. N. J. Shaheen, "Advances in Barrett's esophagus and esophageal adenocarcinoma," Gastroenterology **128**, 1554-1566 (2005).
3. J. Chai and M. M. Jamal, "Esophageal malignancy: A growing concern," World Journal of Gastroenterology : WJG **18**, 6521-6526 (2012).
4. A. Chak, A. Faulx, C. Eng, W. Grady, M. Kinnard, H. Ochs-Balcom, and G. Falk, "Gastroesophageal reflux symptoms in patients with adenocarcinoma of the esophagus or cardia," Cancer **107**, 2160-2166 (2006).
5. S. Öberg, T. R. DeMeester, J. H. Peters, J. A. Hagen, J. J. Nigro, S. R. DeMeester, J. Theisen, G. M. R. Campos, and P. F. Crookes, "The extent of barrett's esophagus depends on the status of the lower esophageal sphincter and the degree of esophageal acid exposure," The Journal of Thoracic and Cardiovascular Surgery **117**, 572-580 (1999).
6. N. Manabe, K. Haruma, H. Imamura, T. Kamada, H. Kusunoki, K. Inoue, A. Shiotani, and J. Hata, "DOES SHORT-SEGMENT COLUMNAR-LINED ESOPHAGUS ELONGATE DURING A MEAN FOLLOW-UP PERIOD OF 5.7 YEARS?," Digestive Endoscopy **23**, 166-172 (2011).
7. S. A. C. McDonald, D. Lavery, N. A. Wright, and M. Jansen, "Barrett oesophagus: lessons on its origins from the lesion itself," Nature Reviews Gastroenterology & Hepatology **12**, 50 (2014).
8. Q. Huang, "Controversies of cardiac glands in the proximal stomach: A critical review," Journal of Gastroenterology and Hepatology **26**, 450-455 (2011).
9. J. M. O'Riordan, O. N. Tucker, P. J. Byrne, G. S. A. McDonald, N. Ravi, P. W. N. Keeling, and J. V. Reynolds, "Factors Influencing The Development of Barrett's Epithelium in The Esophageal Remnant Postesophagectomy," American Journal Of Gastroenterology **99**, 205 (2004).
10. N. J. Shaheen, P. Sharma, B. F. Overholt, H. C. Wolfsen, R. E. Sampliner, K. K. Wang, J. A. Galanko, M. P. Bronner, J. R. Goldblum, A. E. Bennett, B. A. Jobe, G. M. Eisen, M. B. Fennerty, J. G. Hunter, D. E. Fleischer, V. K. Sharma, R. H. Hawes, B. J. Hoffman, R. I. Rothstein, S. R. Gordon, H. Mashimo, K. J. Chang, V. R. Muthusamy, S. A. Edmundowicz, S. J. Spechler, A. A. Siddiqui, R. F. Souza, A. Infantolino, G. W. Falk, M. B. Kimmey, R. D. Madanick, A. Chak, and C. J. Lightdale, "Radiofrequency Ablation in Barrett's Esophagus with Dysplasia," New England journal of medicine **360**, 2277-2288 (2009).
11. C. Ell, A. May, L. Gossner, O. Pech, E. Gunter, G. Mayer, R. Henrich, M. Vieth, H. Muller, G. Seitz, and M. Stolte, "Endoscopic mucosal resection of early cancer and high-grade dysplasia in Barrett's esophagus," Gastroenterology **118**, 670-677 (2000).
12. M. H. Johnston, J. A. Eastone, J. D. Horwhat, J. Cartledge, J. S. Mathews, and J. R. Foggy, "Cryoablation of Barrett's esophagus: a pilot study," Gastrointestinal Endoscopy **62**, 842-848 (2005).
13. A. J. Cameron and H. A. Carpenter, "Barrett's esophagus, high-grade dysplasia, and early adenocarcinoma: A pathological study," American Journal Of Gastroenterology **92**, 586-591 (1997).
14. A. Guthikonda, C. C. Cotton, R. D. Madanick, M. B. Spacek, S. E. Moist, K. Ferrell, E. S. Dellon, and N. J. Shaheen, "Clinical Outcomes Following Recurrence of Intestinal Metaplasia

After Successful Treatment of Barrett's Esophagus With Radiofrequency Ablation," The American journal of gastroenterology **112**, 87 (2016).

15. M. Gupta, P. G. Iyer, L. Lutzke, E. C. Gorospe, J. A. Abrams, G. W. Falk, G. G. Ginsberg, A. K. Rustgi, C. J. Lightdale, T. C. Wang, D. I. Fudman, J. M. Poneros, and K. K. Wang, "Recurrence of Esophageal Intestinal Metaplasia After Endoscopic Mucosal Resection and Radiofrequency Ablation of Barrett's Esophagus: Results From a US Multicenter Consortium," Gastroenterology (2013).
16. C. C. Cotton, W. A. Wolf, S. Pasricha, N. Li, R. D. Madanick, M. B. Spacek, K. Ferrell, E. S. Dellon, and N. J. Shaheen, "Recurrent intestinal metaplasia after radiofrequency ablation for Barrett's esophagus: endoscopic findings and anatomic location," Gastrointestinal Endoscopy **81**, 1362-1369 (2015).
17. R. Kiesslich, J. Fritsch, M. Holtmann, H. H. Koehler, M. Stolte, S. Kanzler, B. Nafe, M. Jung, P. R. Galle, and M. F. Neurath, "Methylene blue-aided chromoendoscopy for the detection of intraepithelial neoplasia and colon cancer in ulcerative colitis," Gastroenterology **124**, 880-888 (2003).
18. P. Sharma, A. P. Weston, M. Topalovski, R. Cherian, A. Bhattacharyya, and R. E. Sampliner, "Magnification chromoendoscopy for the detection of intestinal metaplasia and dysplasia in Barrett's oesophagus," Gut **52**, 24-27 (2003).
19. R. Kiesslich, M. F. Neurath, and P. R. Galle, "Chromoendoscopy and magnifying endoscopy in patients with gastroesophageal reflux disease. Useful or negligible?," Dig Dis **22**, 142-147 (2004).
20. K. Gono, T. Obi, M. Yamaguchi, N. Oyama, H. Machida, Y. Sano, S. Yoshida, Y. Hamamoto, and T. Endo, "Appearance of enhanced tissue features in narrow-band endoscopic imaging," J. Biomed. Opt. **9**, 10 (2004).
21. P. Sharma, A. Bansal, S. Mathur, S. Wani, R. Cherian, D. McGregor, A. Higbee, S. Hall, and A. Weston, "The utility of a novel narrow band imaging endoscopy system in patients with Barrett's esophagus," Gastrointestinal Endoscopy **64**, 167-175 (2006).
22. M. A. Kara, M. Ennahachi, P. Fockens, F. J. W. ten Kate, and J. J. G. H. M. Bergman, "Detection and classification of the mucosal and vascular patterns (mucosal morphology) in Barrett's esophagus by using narrow band imaging," Gastrointestinal Endoscopy **64**, 155-166 (2006).
23. T. Endo, T. Awakawa, H. Takahashi, Y. Arimura, F. Itoh, K. Yamashita, S. Sasaki, H. Yamamoto, X. F. Tang, and K. Imai, "Classification of Barrett's epithelium by magnifying endoscopy," Gastrointestinal Endoscopy **55**, 641-647 (2002).
24. S.-e. Kudo, S. Tamura, T. Nakajima, H.-o. Yamano, H. Kusaka, and H. Watanabe, "Diagnosis of colorectal tumorous lesions by magnifying endoscopy," Gastrointestinal Endoscopy **44**, 8-14 (1996).
25. R. Singh, G. K. Anagnostopoulos, K. Yao, H. Karageorgiou, P. J. Fortun, A. Shonde, K. Garsed, P. V. Kaye, C. J. Hawkey, and K. Ragunath, "Narrow-band imaging with magnification in Barrett's esophagus: validation of a simplified grading system of mucosal morphology patterns against histology," Endoscopy **40**, 457-463 (2008).
26. P. Sharma, J. J. G. H. M. Bergman, K. Goda, M. Kato, H. Messmann, B. R. Alsop, N. Gupta, P. Vennalaganti, M. Hall, V. Konda, A. Koons, O. Penner, J. R. Goldblum, and I. Waxman, "Development and Validation of a Classification System to Identify High-Grade Dysplasia and Esophageal Adenocarcinoma in Barrett's Esophagus Using Narrow-Band Imaging," Gastroenterology **150**, 591-598 (2016).

27. L. Alvarez Herrero, W. L. Curvers, R. Bisschops, M. A. Kara, E. J. Schoon, F. J. W. t. Kate, M. Visser, B. L. A. M. Weusten, and J. J. G. H. M. Bergman, "Narrow band imaging does not reliably predict residual intestinal metaplasia after radiofrequency ablation at the neo-squamo columnar junction," Endoscopy **46**, 98-104 (2014).
28. J. M. Jabbour, M. A. Saldua, J. N. Bixler, and K. C. Maitland, "Confocal Endomicroscopy: Instrumentation and Medical Applications," Annals of biomedical engineering **40**, 378-397 (2012).
29. M. I. Canto, "Endomicroscopy of Barrett's Esophagus," Gastroenterology Clinics of North America **39**, 759-769 (2010).
30. R. Kiesslich, L. Gossner, M. Goetz, A. Dahlmann, M. Vieth, M. Stolte, A. Hoffman, M. Jung, B. Nafe, P. R. Galle, and M. F. Neurath, "In vivo histology of Barrett's esophagus and associated neoplasia by confocal laser endomicroscopy," Clin Gastroenterol Hepatol **4**, 979-987 (2006).
31. T. Kuiper, F. J. C. van den Broek, S. van Eeden, P. Fockens, and E. Dekker, "Feasibility and Accuracy of Confocal Endomicroscopy in Comparison With Narrow-Band Imaging and Chromoendoscopy for the Differentiation of Colorectal Lesions," Am J Gastroenterol **107**, 543-550 (2012).
32. P. Sharma, A. R. Meining, E. Coron, C. J. Lightdale, H. C. Wolfsen, A. Bansal, M. Bajbouj, J.-P. Galmiche, J. A. Abrams, A. Rastogi, N. Gupta, J. E. Michalek, G. Y. Lauwers, and M. B. Wallace, "Real-time increased detection of neoplastic tissue in Barrett's esophagus with probe-based confocal laser endomicroscopy: final results of an international multicenter, prospective, randomized, controlled trial," Gastrointestinal Endoscopy **74**, 465-472 (2011).
33. P. M. Vila, M. J. Kingsley, A. D. Polydorides, M. A. Protano, M. C. Pierce, J. Sauk, M. K. Kim, K. Patel, J. H. Godbold, J. D. Waye, R. Richards-Kortum, and S. Anandasabapathy, "Accuracy and interrater reliability for the diagnosis of Barrett's neoplasia among users of a novel, portable high-resolution microendoscope," Diseases of the esophagus : official journal of the International Society for Diseases of the Esophagus / I.S.D.E **27**, 55-62 (2014).
34. M.-A. Protano, H. Xu, G. Wang, A. D. Polydorides, S. M. Dawsey, J. Cui, L. Xue, F. Zhang, T. Quang, M. C. Pierce, D. Shin, R. A. Schwarz, M. S. Bhutani, M. Lee, N. Parikh, C. Hur, W. Xu, E. Moshier, J. Godbold, J. Mitcham, C. Hudson, R. R. Richards-Kortum, and S. Anandasabapathy, "Low-Cost High-Resolution Microendoscopy for the Detection of Esophageal Squamous Cell Neoplasia: An International Trial," Gastroenterology **149**, 321-329 (2015).
35. M. V. Sivak, Jr., K. Kobayashi, J. A. Izatt, A. M. Rollins, R. Ung-Runyawee, A. Chak, R. C. Wong, G. A. Isenberg, and J. Willis, "High-resolution endoscopic imaging of the GI tract using optical coherence tomography," Gastrointestinal Endoscopy **51(4) Pt 1**, 474-479 (2000).
36. S. H. Yun, G. J. Tearney, B. J. Vakoc, M. Shishkov, W. Y. Oh, A. E. Desjardins, M. J. Suter, R. C. Chan, J. A. Evans, I. K. Jang, N. S. Nishioka, J. F. de Boer, and B. E. Bouma, "Comprehensive volumetric optical microscopy in vivo," Nature Medicine **12**, 1429-1433 (2006).
37. D. C. Adler, Y. Chen, R. Huber, J. Schmitt, J. Connolly, and J. G. Fujimoto, "Three-dimensional endomicroscopy using optical coherence tomography," Nature Photonics **1**, 709-716 (2007).
38. B. J. Vakoc, M. Shishko, S. H. Yun, W. Y. Oh, M. J. Suter, A. E. Desjardins, J. A. Evans, N. S. Nishioka, G. J. Tearney, and B. E. Bouma, "Comprehensive esophageal microscopy by using optical frequency-domain imaging (with video)," Gastrointestinal Endoscopy **65**, 898-905 (2007).
39. M. J. Suter, B. J. Vakoc, P. S. Yachimski, M. Shishkov, G. Y. Lauwers, M. Mino-Kenudson, B. E. Bouma, N. S. Nishioka, and G. J. Tearney, "Comprehensive microscopy of the esophagus in human patients with optical frequency domain imaging," Gastrointestinal Endoscopy **68**, 745-753 (2008).

40. H. C. Wolfsen, P. Sharma, M. B. Wallace, C. Leggett, G. Tearney, and K. K. Wang, "Safety and feasibility of volumetric laser endomicroscopy in patients with Barrett's esophagus (with videos)," Gastrointestinal Endoscopy (2015).
41. N. Uribe-Patarroyo and B. E. Bouma, "Rotational distortion correction in endoscopic optical coherence tomography based on speckle decorrelation," Optics Letters **40**, 5518-5521 (2015).
42. C. L. Leggett, E. C. Gorospe, D. K. Chan, P. Muppa, V. Owens, T. C. Smyrk, M. Anderson, L. S. Lutzke, G. Tearney, and K. K. Wang, "Comparative diagnostic performance of volumetric laser endomicroscopy and confocal laser endomicroscopy in the detection of dysplasia associated with Barrett's esophagus," Gastrointestinal Endoscopy **83**, 880-888.e882 (2016).
43. A.-F. Swager, G. J. Tearney, C. L. Leggett, M. G. H. van Oijen, S. L. Meijer, B. L. Weusten, W. L. Curvers, and J. J. G. H. M. Bergman, "Identification of volumetric laser endomicroscopy features predictive for early neoplasia in Barrett's esophagus using high-quality histological correlation," Gastrointestinal Endoscopy **85**, 918-926.e917 (2017).
44. J. A. Evans, J. M. Poneros, B. E. Bouma, J. Bressner, E. F. Halpern, M. Shishkov, G. Y. Lauwers, M. Mino-Kenudson, N. S. Nishioka, and G. J. Tearney, "Optical coherence tomography to identify intramucosal carcinoma and high-grade dysplasia in Barrett's esophagus," Clinical Gastroenterology and Hepatology **4**, 38-43 (2006).
45. G. Isenberg, M. V. Sivak, A. Chak, R. C. K. Wong, J. E. Willis, B. Wolf, D. Y. Rowland, A. Das, and A. Rollins, "Accuracy of endoscopic optical coherence tomography in the detection of dysplasia in Barrett's esophagus: a prospective, double-blinded study," Gastrointestinal Endoscopy **62**, 825-831 (2005).
46. A. J. Trindade, S. Inamdar, M. S. Smith, K. J. Chang, C. L. Leggett, C. J. Lightdale, D. K. Pleskow, D. V. Sejpal, G. J. Tearney, R. M. Thomas, and M. B. Wallace, "Volumetric laser endomicroscopy in Barrett's esophagus: interobserver agreement for interpretation of Barrett's esophagus and associated neoplasia among high-frequency users," Gastrointestinal Endoscopy **86**, 133-139 (2017).
47. M. J. Suter, P. A. Jillella, B. J. Vakoc, E. F. Halpern, M. Mino-Kenudson, G. Y. Lauwers, B. E. Bouma, N. S. Nishioka, and G. J. Tearney, "Image-guided biopsy in the esophagus through comprehensive optical frequency domain imaging and laser marking: a study in living swine," Gastrointestinal Endoscopy **71**, 346-353 (2010).
48. M. J. Suter, M. J. Gora, G. Y. Lauwers, T. Arnason, J. Sauk, K. A. Gallagher, L. Kava, K. M. Tan, A. R. Soomro, T. P. Gallagher, J. A. Gardecki, B. E. Bouma, M. Rosenberg, N. S. Nishioka, and G. J. Tearney, "Esophageal-guided biopsy with volumetric laser endomicroscopy and laser cautery marking: a pilot clinical study," Gastrointestinal Endoscopy **79**, 886-896 (2014).
49. A. D. Aguirre, "Advances in Optical Coherence Tomography and Microscopy for endoscopic applications and functional neuroimaging," (Massachusetts Institute of Technology, 2008).
50. G. J. Tearney, M. E. Brezinski, B. E. Bouma, S. A. Boppart, C. Pitris, J. F. Southern, and J. G. Fujimoto, "In vivo endoscopic optical biopsy with optical coherence tomography," Science **276**, 2037-2039 (1997).
51. O. O. Ahsen, H.-C. Lee, M. G. Giacomelli, Z. Wang, K. Liang, T.-H. Tsai, B. Potsaid, H. Mashimo, and J. G. Fujimoto, "Correction of rotational distortion for catheter-based en face OCT and OCT angiography," Optics Letters **39**, 5973-5976 (2014).
52. T.-H. Tsai, O. O. Ahsen, H.-C. Lee, K. Liang, M. Figueiredo, Y. K. Tao, M. G. Giacomelli, B. M. Potsaid, V. Jayaraman, Q. Huang, A. E. Cable, J. G. Fujimoto, and H. Mashimo, "Endoscopic Optical Coherence Angiography Enables 3-Dimensional Visualization of Subsurface Microvasculature," Gastroenterology **147**, 1219-1221 (2014).

53. J. C. Jing, L. Chou, E. Su, B. J. F. Wong, and Z. Chen, "Anatomically correct visualization of the human upper airway using a high-speed long range optical coherence tomography system with an integrated positioning sensor," Scientific Reports **6**, 39443 (2016).
54. K. Liang, O. O. Ahsen, H.-C. Lee, Z. Wang, B. M. Potsaid, M. Figueiredo, V. Jayaraman, A. E. Cable, Q. Huang, H. Mashimo, and J. G. Fujimoto, "Volumetric Mapping of Barrett's Esophagus and Dysplasia With en face Optical Coherence Tomography Tethered Capsule," Am J Gastroenterol **111**, 1664-1666 (2016).
55. K. Liang, G. Traverso, H.-C. Lee, O. O. Ahsen, Z. Wang, B. Potsaid, M. Giacomelli, V. Jayaraman, R. Barman, A. Cable, H. Mashimo, R. Langer, and J. G. Fujimoto, "Ultrahigh speed en face OCT capsule for endoscopic imaging," Biomedical Optics Express **6**, 1146-1163 (2015).
56. S. Makita, Y. Hong, M. Yamanari, T. Yatagai, and Y. Yasuno, "Optical coherence angiography," Optics Express **14**, 7821-7840 (2006).
57. H.-C. Lee, O. O. Ahsen, K. Liang, Z. Wang, C. Cleveland, L. Booth, B. Potsaid, V. Jayaraman, A. E. Cable, H. Mashimo, R. Langer, G. Traverso, and J. G. Fujimoto, "Circumferential optical coherence tomography angiography imaging of the swine esophagus using a micromotor balloon catheter," Biomedical Optics Express **7**, 2927-2942 (2016).
58. Y.-H. Seo, K. Hwang, H.-C. Park, and K.-H. Jeong, "Electrothermal MEMS fiber scanner for optical endomicroscopy," Optics Express **24**, 3903-3909 (2016).
59. L. Huo, J. F. Xi, Y. C. Wu, and X. D. Li, "Forward-viewing resonant fiber-optic scanning endoscope of appropriate scanning speed for 3D OCT imaging," Optics Express **18**, 14375-14384 (2010).
60. C. M. Lee, C. J. Engelbrecht, T. D. Soper, F. Helmchen, and E. J. Seibel, "Scanning fiber endoscopy with highly flexible, 1 mm catheterscopes for wide-field, full-color imaging," Journal of Biophotonics **3**, 385-407 (2010).
61. N. Zhang, T.-H. Tsai, O. O. Ahsen, K. Liang, H.-C. Lee, P. Xue, X. Li, and J. G. Fujimoto, "Compact piezoelectric transducer fiber scanning probe for optical coherence tomography," Optics Letters **39**, 186-188 (2014).
62. K. L. Lurie, A. A. Gurjarpadhye, E. J. Seibel, and A. K. Ellerbee, "Rapid scanning catheterscope for expanded forward-view volumetric imaging with optical coherence tomography," Optics Letters **40**, 3165-3168 (2015).
63. V. Jayaraman, J. Jiang, H. Li, P. J. S. Heim, G. D. Cole, B. Potsaid, J. G. Fujimoto, and A. Cable, "OCT imaging up to 760 kHz axial scan rate using single-mode 1310nm MEMS-tunable VCSELs with >100nm tuning range," in *Lasers and Electro-Optics (CLEO)*, (IEEE, 2011), 1-2.
64. X. Liu, M. J. Cobb, Y. Chen, M. B. Kimmey, and X. Li, "Rapid-scanning forward-imaging miniature endoscope for real-time optical coherence tomography," Optics Letters **29**, 1763-1765 (2004).
65. "60601-1 Medical electrical equipment general requirements for basic safety and essential performance," International Electrotechnical Commission, 69-70 (2005).
66. E. Jonathan, J. Enfield, and M. J. Leahy, "Correlation mapping method for generating microcirculation morphology from optical coherence tomography (OCT) intensity images," Journal of Biophotonics **4**, 583-587 (2011).
67. C. J. Chen, "Electromechanical deflections of piezoelectric tubes with quartered electrodes," Applied Physics Letters **60**, 132-134 (1992).
68. K. Liang, "Forward viewing OCT endomicroscopy," (MIT, 2014).

69. C. Hassan, P. J. Pickhardt, and D. K. Rex, "A Resect and Discard Strategy Would Improve Cost-Effectiveness of Colorectal Cancer Screening," Clinical Gastroenterology and Hepatology **8**, 865-869.e863 (2010).
70. W. Wieser, W. Draxinger, T. Klein, S. Karpf, T. Pfeiffer, and R. Huber, "High definition live 3D-OCT in vivo: design and evaluation of a 4D OCT engine with 1 GVoxel/s," Biomedical Optics Express **5**, 2963-2977 (2014).
71. J. F. Xi, L. Huo, Y. C. Wu, M. J. Cobb, J. H. Hwang, and X. D. Li, "High-resolution OCT balloon imaging catheter with astigmatism correction," Optics Letters **34**, 1943-1945 (2009).
72. J. Su, J. Zhang, L. Yu, H. G Colt, M. Brenner, and Z. Chen, "Real-time swept source optical coherence tomography imaging of the human airway using a microelectromechanical system endoscope and digital signal processor," J Biomed Opt **13**, 030506 (2008).
73. T. H. Tsai, B. Potsaid, M. F. Kraus, C. Zhou, Y. K. Tao, J. Hornegger, and J. G. Fujimoto, "Piezoelectric-transducer-based miniature catheter for ultrahigh-speed endoscopic optical coherence tomography," Biomedical Optics Express **2**, 2438-2448 (2011).
74. P. R. Herz, Y. Chen, A. D. Aguirre, K. Schneider, P. Hsiung, J. G. Fujimoto, K. Madden, J. Schmitt, J. Goodnow, and C. Petersen, "Micromotor endoscope catheter for in vivo, ultrahigh-resolution optical coherence tomography," Optics Letters **29**, 2261-2263 (2004).
75. P. H. Tran, D. S. Mukai, M. Brenner, and Z. P. Chen, "In vivo endoscopic optical coherence tomography by use of a rotational microelectromechanical system probe," Optics Letters **29**, 1236-1238 (2004).
76. J. Li, M. de Groot, F. Helderman, J. Mo, J. M. A. Daniels, K. Grünberg, T. G. Sutedja, and J. F. de Boer, "High speed miniature motorized endoscopic probe for optical frequency domain imaging," Opt. Express **20**, 24132-24138 (2012).
77. T.-H. Tsai, B. Potsaid, Y. K. Tao, V. Jayaraman, J. Jiang, P. J. S. Heim, M. F. Kraus, C. Zhou, J. Hornegger, H. Mashimo, A. E. Cable, and J. G. Fujimoto, "Ultrahigh speed endoscopic optical coherence tomography using micromotor imaging catheter and VCSEL technology," Biomedical Optics Express **4**, 1119-1132 (2013).
78. T. Wang, W. Wieser, G. Springeling, R. Beurskens, C. T. Lancee, T. Pfeiffer, A. F. W. van der Steen, R. Huber, and G. v. Soest, "Intravascular optical coherence tomography imaging at 3200 frames per second," Optics Letters **38**, 1715-1717 (2013).
79. T.-H. Tsai, H.-C. Lee, O. O. Ahsen, K. Liang, M. G. Giacomelli, B. M. Potsaid, Y. K. Tao, V. Jayaraman, M. Figueiredo, Q. Huang, A. E. Cable, J. Fujimoto, and H. Mashimo, "Ultrahigh speed endoscopic optical coherence tomography for gastroenterology," Biomedical Optics Express **5**, 4387-4404 (2014).
80. X. Liu, M. J. Cobb, Y. Chen, M. B. Kimmey, and X. Li, "Rapid-scanning forward-imaging miniature endoscope for real-time optical coherence tomography," Opt Lett **29**, 1763-1765 (2004).
81. J. Sawinski and W. Denk, "Miniature random-access fiber scanner for in vivo multiphoton imaging," Journal of Applied Physics **102**, - (2007).
82. A. D. Aguirre, J. Sawinski, S. W. Huang, C. Zhou, W. Denk, and J. G. Fujimoto, "High speed optical coherence microscopy with autofocus adjustment and a miniaturized endoscopic imaging probe," Optics Express **18**, 4222-4239 (2010).
83. D. R. Rivera, C. M. Brown, D. G. Ouzounov, I. Pavlova, D. Kobat, W. W. Webb, and C. Xu, "Compact and flexible raster scanning multiphoton endoscope capable of imaging unstained tissue," Proceedings of the National Academy of Sciences (2011).
84. D. Do, H. Yoo, and D.-G. Gweon, "Fiber-optic raster scanning two-photon endomicroscope using a tubular piezoelectric actuator," Journal of Biomedical Optics **19**, 066010-066010 (2014).

85. S. Chang, E. Murdock, Y. Mao, C. Flueraru, and J. Disano, "Stationary-fiber rotary probe with unobstructed 360° view for optical coherence tomography," Optics Letters **36**, 4392-4394 (2011).
86. G. Iddan, G. Meron, A. Glukhovsky, and P. Swain, "Wireless capsule endoscopy," Nature **405**, 417-417 (2000).
87. F. C. Ramirez, M. S. Shaukat, M. A. Young, D. A. Johnson, and R. Akins, "Feasibility and safety of string, wireless capsule endoscopy in the diagnosis of Barrett's esophagus," Gastrointestinal Endoscopy **61**, 741-746 (2005).
88. F. C. Ramirez, R. Akins, and M. Shaukat, "Screening of Barrett's esophagus with string-capsule endoscopy: a prospective blinded study of 100 consecutive patients using histology as the criterion standard," Gastrointestinal Endoscopy **68**, 25-31 (2008).
89. Z. Liao, R. Gao, C. Xu, D.-F. Xu, and Z.-S. Li, "Sleeve string capsule endoscopy for real-time viewing of the esophagus: a pilot study (with video)," Gastrointestinal Endoscopy **70**, 201-209 (2009).
90. E. J. Seibel, R. E. Carroll, J. A. Dominitz, R. S. Johnston, C. D. Melville, C. M. Lee, S. M. Seitz, and M. B. Kimmey, "Tethered Capsule Endoscopy, A Low-Cost and High-Performance Alternative Technology for the Screening of Esophageal Cancer and Barrett's Esophagus," Biomedical Engineering, IEEE Transactions on **55**, 1032-1042 (2008).
91. E. J. Seibel, C. M. Brown, J. A. Dominitz, and M. B. Kimmey, "Scanning Single Fiber Endoscopy: A New Platform Technology for Integrated Laser Imaging, Diagnosis, and Future Therapies," Gastrointestinal Endoscopy Clinics of North America **18**, 467-478 (2008).
92. M. J. Gora, J. S. Sauk, R. W. Carruth, K. A. Gallagher, M. J. Suter, N. S. Nishioka, L. E. Kava, M. Rosenberg, B. E. Bouma, and G. J. Tearney, "Tethered capsule endomicroscopy enables less invasive imaging of gastrointestinal tract microstructure," Nature Medicine **19**, 238-240 (2013).
93. N. Tabatabaei, D. Kang, T. Wu, M. Kim, R. W. Carruth, J. Leung, J. S. Sauk, W. Shreffler, Q. Yuan, A. Katz, N. S. Nishioka, and G. J. Tearney, "Tethered confocal endomicroscopy capsule for diagnosis and monitoring of eosinophilic esophagitis," Biomedical Optics Express **5**, 197-207 (2014).
94. M. J. Gora, J. S. Sauk, R. W. Carruth, W. Lu, D. T. Carlton, A. Soomro, M. Rosenberg, N. S. Nishioka, and G. J. Tearney, "Imaging the Upper Gastrointestinal Tract in Unsedated Patients Using Tethered Capsule Endomicroscopy," Gastroenterology **145**, 723-725 (2013).
95. T. Endo, T. Awakawa, H. Takahashi, Y. Arimura, F. Itoh, K. Yamashita, S. Sasaki, H. Yamamoto, X. Tang, and K. Imai, "Classification of Barrett's epithelium by magnifying endoscopy," Gastrointestinal Endoscopy **55**, 641-647 (2002).
96. B. Potsaid, V. Jayaraman, J. G. Fujimoto, J. Jiang, P. J. S. Heim, and A. E. Cable, "MEMS tunable VCSEL light source for ultrahigh speed 60kHz - 1MHz axial scan rate and long range centimeter class OCT imaging," Proc. SPIE 8213, Optical Coherence Tomography and Coherence Domain Optical Methods in Biomedicine XVI **8213**, 82130M-82130M-82138 (2012).
97. Merck, "The Merck Veterinary Manual Reference Guides", retrieved 02/25/2015, http://www.merckmanuals.com/vet/appendixes/reference_guides/resting_heart_rates.html.
98. R. Singh, G. K. Anagnostopoulos, K. Yao, H. Karageorgiou, P. J. Fortun, A. Shonde, K. Garsed, P. V. Kaye, C. J. Hawkey, and K. Ragunath, "Narrow-band imaging with magnification in Barrett's esophagus: validation of a simplified grading system of mucosal morphology patterns against histology," Endoscopy **40**, 457,463 (2008).
99. O. O. Ahsen, Y. K. Tao, B. M. Potsaid, Y. Sheikine, J. Jiang, I. Grulkowski, T.-H. Tsai, V. Jayaraman, M. F. Kraus, J. L. Connolly, J. Hornegger, A. Cable, and J. G. Fujimoto, "Swept source

optical coherence microscopy using a 1310 nm VCSEL light source," Optics Express **21**, 18021-18033 (2013).
100. H.-C. Lee, J. J. Liu, Y. Sheikine, A. D. Aguirre, J. L. Connolly, and J. G. Fujimoto, "Ultrahigh speed spectral-domain optical coherence microscopy," Biomedical Optics Express **4**, 1236-1254 (2013).
101. I. Grulkowski, J. J. Liu, B. Potsaid, V. Jayaraman, J. Jiang, J. G. Fujimoto, and A. E. Cable, "High-precision, high-accuracy ultralong-range swept-source optical coherence tomography using vertical cavity surface emitting laser light source," Optics Letters **38**, 673-675 (2013).
102. B. Y. Yeo, R. A. McLaughlin, R. W. Kirk, and D. D. Sampson, "Enabling freehand lateral scanning of optical coherence tomography needle probes with a magnetic tracking system," Biomedical Optics Express **3**, 1565-1578 (2012).
103. N. D. Shemonski, S. S. Ahn, Y.-Z. Liu, F. A. South, P. S. Carney, and S. A. Boppart, "Three-dimensional motion correction using speckle and phase for in vivo computed optical interferometric tomography," Biomedical Optics Express **5**, 4131-4143 (2014).
104. S. A. Rodriguez, S. Banerjee, D. Desilets, D. L. Diehl, F. A. Farraye, V. Kaul, R. S. Kwon, P. Mamula, M. C. Pedrosa, S. Varadarajulu, L.-M. W. K. Song, and W. M. Tierney, "Ultrathin endoscopes," Gastrointestinal Endoscopy **71**, 893-898 (2010).
105. B. E. Lacy, T. O'Shana, M. Hynes, M. L. Kelley, J. E. Weiss, L. Paquette, and R. I. Rothstein, "Safety and Tolerability of Transoral Bravo Capsule Placement After Transnasal Manometry Using a Validated Conversion Factor," Am J Gastroenterol **102**, 24-32 (2007).
106. C. Zhou, D. C. Adler, L. Becker, Y. Chen, T.-H. Tsai, M. Figueiredo, J. M. Schmitt, J. G. Fujimoto, and H. Mashimo, "Effective treatment of chronic radiation proctitis using radiofrequency ablation " Therapeutic Advances in Gastroenterology **2**, 149-156 (2009).
107. M. Singh, A. Bansal, W. L. Curvers, M. A. Kara, S. B. Wani, L. A. Herrero, C. R. Lynch, M. C. A. van Kouwen, F. T. Peters, J. D. Keighley, A. Rastogi, K. Pondugula, R. Kim, V. Singh, S. Gaddam, J. J. Bergman, and P. Sharma, "Observer agreement in the assessment of narrow-band imaging system surface patterns in Barrett's esophagus: a multicenter study," Endoscopy **43**, 745-751 (2011).
108. R. A. Ganz, D. S. Utley, R. A. Stern, J. Jackson, K. P. Batts, and P. Termin, "Complete ablation of esophageal epithelium with a balloon-based bipolar electrode: a phased evaluation in the porcine and in the human esophagus," Gastrointestinal Endoscopy **60**, 1002-1010 (2004).
109. W. Crosby, U. S. Army, and H. Kugler, "Intraluminal biopsy of the small intestine," The American Journal of Digestive Diseases **2**, 236-241 (1957).
110. M. J. Gora, A. R. Soomro, W. P. Puricelli, W. Lu, E. Quijano, L. a. Moffitt, M. Rosenberg, J. Sauk, N. S. Nishioka, and G. J. Tearney, "359 Unsedated Screening for Barrett's Esophagus Using Tethered Capsule Endomicroscopy," Gastrointestinal Endoscopy **79**, AB136 (2014).
111. J. A. Evans, J. M. Poneros, B. E. Bouma, J. Bressner, E. F. Halpern, M. Shishkov, G. Y. Lauwers, M. Mino–Kenudson, N. S. Nishioka, and G. J. Tearney, "Optical Coherence Tomography to Identify Intramucosal Carcinoma and High-Grade Dysplasia in Barrett's Esophagus," Clinical Gastroenterology and Hepatology **4**, 38-43 (2006).
112. G. J. Ughi, M. J. Gora, A.-F. Swager, A. Soomro, C. Grant, A. Tiernan, M. Rosenberg, J. S. Sauk, N. S. Nishioka, and G. J. Tearney, "Automated segmentation and characterization of esophageal wall in vivo by tethered capsule optical coherence tomography endomicroscopy," Biomedical Optics Express **7**, 409-419 (2016).
113. P. Sharma, R. H. Hawes, A. Bansal, N. Gupta, W. Curvers, A. Rastogi, M. Singh, M. Hall, S. C. Mathur, S. B. Wani, B. Hoffman, S. Gaddam, P. Fockens, and J. J. Bergman, "Standard

endoscopy with random biopsies versus narrow band imaging targeted biopsies in Barrett's oesophagus: a prospective, international, randomised controlled trial," Gut **62**, 15-21 (2013).

114. R. Maselli, H. Inoue, H. Ikeda, M. Onimaru, A. Yoshida, E. G. Santi, H. Sato, B. H. Hayee, and S.-E. Kudo, "Microvasculature of the esophagus and gastroesophageal junction: Lesson learned from submucosal endoscopy," World journal of gastrointestinal endoscopy **8**, 690-696 (2016).

115. G. van Soest, J. G. Bosch, and A. F. W. van der Steen, "Azimuthal registration of image sequences affected by nonuniform rotation distortion," Ieee Transactions on Information Technology in Biomedicine **12**, 348-355 (2008).

116. W. Kang, H. Wang, Z. Wang, M. W. Jenkins, G. A. Isenberg, A. Chak, and A. M. Rollins, "Motion artifacts associated with in vivo endoscopic OCT images of the esophagus," Optics Express **19**, 20722-20735 (2011).

117. J. Mavadia, J. Xi, Y. Chen, and X. Li, "An all-fiber-optic endoscopy platform for simultaneous OCT and fluorescence imaging," Biomedical Optics Express **3**, 2851-2859 (2012).

118. H.-C. Park, C. Song, M. Kang, Y. Jeong, and K.-H. Jeong, "Forward imaging OCT endoscopic catheter based on MEMS lens scanning," Optics Letters **37**, 2673-2675 (2012).

119. S. J. Miller, C. M. Lee, B. P. Joshi, A. Gaustad, E. J. Seibel, and T. D. Wang, "Targeted detection of murine colonic dysplasia in vivo with flexible multispectral scanning fiber endoscopy," Journal of Biomedical Optics **17**, 0211031-02110311 (2012).

120. M. T. Myaing, D. J. MacDonald, and X. D. Li, "Fiber-optic scanning two-photon fluorescence endoscope," Optics Letters **31**, 1076-1078 (2006).

121. J. F. Xi, Y. P. Chen, Y. Y. Zhang, K. Murari, M. J. Li, and X. D. Li, "Integrated multimodal endomicroscopy platform for simultaneous en face optical coherence and two-photon fluorescence imaging," Optics Letters **37**, 362-364 (2012).

122. W. Liang, G. Hall, B. Messerschmidt, M. Li, and X. Li, "Nonlinear optical endomicroscopy for label-free functional histology in vivo," Light: Science and Applications **6**(2017).

123. S. Moon, S. W. Lee, M. Rubinstein, B. J. F. Wong, and Z. P. Chen, "Semi-resonant operation of a fiber-cantilever piezotube scanner for stable optical coherence tomography endoscope imaging," Optics Express **18**, 21183-21197 (2010).

124. W. Liang, K. Murari, Y. Y. Zhang, Y. Chen, X. D. Li, and M.-J. Li, "Increased illumination uniformity and reduced photodamage offered by the Lissajous scanning in fiber-optic two-photon endomicroscopy," Journal of Biomedical Optics **17**, 6 (2012).

125. H.-C. Park, Y.-H. Seo, and K.-H. Jeong, "Lissajous fiber scanning for forward viewing optical endomicroscopy using asymmetric stiffness modulation," Optics Express **22**, 5818-5825 (2014).

126. R. K. Wang, S. L. Jacques, Z. Ma, S. Hurst, S. R. Hanson, and A. Gruber, "Three dimensional optical angiography," Optics Express **15**, 4083-4097 (2007).

127. A. Mariampillai, B. A. Standish, E. H. Moriyama, M. Khurana, N. R. Munce, M. K. K. Leung, J. Jiang, A. Cable, B. C. Wilson, I. A. Vitkin, and V. X. D. Yang, "Speckle variance detection of microvasculature using swept-source optical coherence tomography," Optics Letters **33**, 1530-1532 (2008).

128. B. J. Vakoc, R. M. Lanning, J. A. Tyrrell, T. P. Padera, L. A. Bartlett, T. Stylianopoulos, L. L. Munn, G. J. Tearney, D. Fukumura, R. K. Jain, and B. E. Bouma, "Three-dimensional microscopy of the tumor microenvironment in vivo using optical frequency domain imaging," Nature Medicine **15**, 1219-U1151 (2009).

129. V. X. D. Yang, S.-j. Tang, M. L. Gordon, B. Qi, G. Gardiner, M. Cirocco, P. Kortan, G. B. Haber, G. Kandel, I. A. Vitkin, B. C. Wilson, and N. E. Marcon, "Endoscopic Doppler optical

coherence tomography in the human GI tract: initial experience," Gastrointestinal Endoscopy **61**, 879-890 (2005).

130. K. Liang, O. O. Ahsen, Z. Wang, H.-C. Lee, W. Liang, B. M. Potsaid, T.-H. Tsai, M. G. Giacomelli, V. Jayaraman, H. Mashimo, X. Li, and J. G. Fujimoto, "Endoscopic forward-viewing optical coherence tomography and angiography with MHz swept source," Optics Letters **42**, 3193-3196 (2017).

131. Y. K. Yong, S. O. R. Moheimani, and I. R. Petersen, "High-speed cycloid-scan atomic force microscopy," Nanotechnology **21**, 365503 (2010).

132. R. C. Yates, *A Handbook on Curves and their Properties* (J.W. Edwards, Ann Arbor, MI, 1947), pp. 233-236.

133. M. Wallace, G. Y. Lauwers, Y. Chen, E. Dekker, P. Fockens, P. Sharma, and A. Meining, "Miami classification for probe-based confocal laser endomicroscopy," Endoscopy **43**, 882,891 (2011).

134. R. L. Siegel, K. D. Miller, S. A. Fedewa, D. J. Ahnen, R. G. S. Meester, A. Barzi, and A. Jemal, "Colorectal cancer statistics, 2017," CA Cancer J Clin **67**, 177-193 (2017).

135. T. Klein and R. Huber, "High-speed OCT light sources and systems [Invited]," Biomedical Optics Express **8**, 828-859 (2017).

136. G. S. Dulai, S. Guha, K. L. Kahn, J. Gornbein, and W. M. Weinstein, "Preoperative prevalence of Barrett's esophagus in esophageal adenocarcinoma: A systematic review," Gastroenterology **122**, 26-33 (2002).

137. C. S. Ross-Innes, I. Debiram-Beecham, M. O'Donovan, E. Walker, S. Varghese, P. Lao-Sirieix, L. Lovat, M. Griffin, K. Ragunath, R. Haidry, S. S. Sami, P. Kaye, M. Novelli, B. Disep, R. Ostler, B. Aigret, B. V. North, P. Bhandari, A. Haycock, D. Morris, S. Attwood, A. Dhar, C. Rees, M. D. D. Rutter, P. D. Sasieni, R. C. Fitzgerald, and B. S. G. on behalf of the, "Evaluation of a Minimally Invasive Cell Sampling Device Coupled with Assessment of Trefoil Factor 3 Expression for Diagnosing Barrett's Esophagus: A Multi-Center Case–Control Study," PLOS Medicine **12**, e1001780 (2015).

138. S. S. Sami, K. T. Dunagan, M. L. Johnson, C. D. Schleck, N. D. Shah, A. R. Zinsmeister, L.-M. Wongkeesong, K. K. Wang, D. A. Katzka, K. Ragunath, and P. G. Iyer, "A Randomized Comparative Effectiveness Trial of Novel Endoscopic Techniques and Approaches for Barrett's Esophagus Screening in the Community," The American journal of gastroenterology **110**, 148 (2014).

139. M. K. Shariff, S. Varghese, M. O'Donovan, Z. Abdullahi, X. Liu, R. C. Fitzgerald, and M. di Pietro, "Pilot randomized crossover study comparing the efficacy of transnasal disposable endosheath with standard endoscopy to detect Barrett's esophagus," Endoscopy **48**, 110-116 (2016).

140. D. K. Chan, L. Zakko, K. H. Visrodia, C. L. Leggett, L. S. Lutzke, M. A. Clemens, J. D. Allen, M. A. Anderson, and K. K. Wang, "Breath Testing for Barrett's Esophagus Using Exhaled Volatile Organic Compound Profiling With an Electronic Nose Device," Gastroenterology **152**, 24-26 (2017).

141. H. R. Moinova, T. LaFramboise, J. D. Lutterbaugh, A. K. Chandar, J. Dumot, A. Faulx, W. Brock, O. De la Cruz Cabrera, K. Guda, J. S. Barnholtz-Sloan, P. G. Iyer, M. I. Canto, J. S. Wang, N. J. Shaheen, P. N. Thota, J. E. Willis, A. Chak, and S. D. Markowitz, "Identifying DNA methylation biomarkers for non-endoscopic detection of Barrett's esophagus," Science Translational Medicine **10**(2018).

142. M. Alshelleh, S. Inamdar, M. McKinley, M. Stewart, J. S. Novak, R. E. Greenberg, K. Sultan, B. Devito, M. Cheung, M. A. Cerulli, L. S. Miller, D. V. Sejpal, A. K. Vegesna, and A. J. Trindade, "Incremental yield of dysplasia detection in Barrett's esophagus using volumetric laser endomicroscopy with and without laser marking compared with a standardized random biopsy protocol," Gastrointestinal Endoscopy (2018).
143. M. J. Gora, L. H. Simmons, L. Quénéhervé, C. N. Grant, R. W. Carruth, W. Lu, A. Tiernan, J. Dong, B. W. Corkery, A. Soomro, M. Rosenberg, J. P. Metlay, and G. J. Tearney, "Tethered capsule endomicroscopy: from bench to bedside at a primary care practice," J. Biomed. Opt. **21**, 104001 (2016).
144. O. O. Ahsen, K. Liang, H.-C. Lee, M. G. Giacomelli, Z. Wang, B. M. Potsaid, M. Figueiredo, Q. Huang, V. Jayaraman, J. G. Fujimoto, and H. Mashimo, "Assessment of Barrett's Esophagus and Dysplasia with Ultrahigh-speed Volumetric En face and Cross-sectional Optical Coherence Tomography," Endoscopy **in review**(2018).
145. T. Hershcovici, H. Mashimo, and R. Fass, "The lower esophageal sphincter," Neurogastroenterology & Motility **23**, 819-830 (2011).
146. D. R. Lichtenstein, S. Jagannath, T. H. Baron, M. A. Anderson, S. Banerjee, J. A. Dominitz, R. D. Fanelli, S. I. Gan, M. E. Harrison, S. O. Ikenberry, B. Shen, L. Stewart, K. Khan, and J. J. Vargo, "Sedation and anesthesia in GI endoscopy," Gastrointestinal Endoscopy **68**, 815-826 (2008).
147. T. Loughney, C. L. Maydonovitch, and R. K. H. Wong, "Esophageal manometry and ambulatory 24-hour pH monitoring in patients with short and long segment Barrett's esophagus," American Journal Of Gastroenterology **93**, 916 (1998).
148. N. Gupta, U. Siddiqui, I. Waxman, C. Chapman, A. Koons, V. Valuckaite, S.-Y. Xiao, N. Setia, J. Hart, and V. Konda, "Use of volumetric laser endomicroscopy for dysplasia detection at the gastroesophageal junction and gastric cardia," World journal of gastrointestinal endoscopy **9**, 319-326 (2017).
149. P. Sharma, J. Dent, D. Armstrong, J. J. G. H. M. Bergman, L. Gossner, Y. Hoshihara, J. A. Jankowski, O. Junghard, L. Lundell, G. N. J. Tytgat, and M. Vieth, "The Development and Validation of an Endoscopic Grading System for Barrett's Esophagus: The Prague C & M Criteria," Gastroenterology **131**, 1392-1399 (2006).